MICROMECHANISMS FOR PLASTICITY AND FRACTURE OF Si-Al-O-N CERAMICS

BY

B. S. B. KARUNARATNE

A dissertation submitted to the University of Warwick
for admission to the degree of Doctor of Philosophy

Department of Physics

January 1980

ACKNOWLEDGEMENTS

I would like to thank Professor A. J. Forty for the provision of laboratory facilities in the Department of Physics. I am indebted to Dr. M. H. Lewis for his continued interest and advice concerning the research and during the preparation of this thesis.

I wish to thank the Commonwealth Scholarship Commission for the award of a grant which made this research possible.

I would also like to thank many others who assisted me during this work particularly Gerry Smith and Martin Thornton for their kind help during the past three years and also Roy McLeod for help in the production of some photographs.

Thanks are due to Dr. R. J. Lumby and Mr. B. North at the Lucas Group Research Centre, Monkspath, Solihull for preparation of the hot-pressed ceramics and JEOL U.K. Ltd. for allowing me to use their 100 CX electron microscope for some high-resolution work.

Thanks are also due to Sandra Callanan for her accurate typing of this thesis.

Finally, I would like to thank my parents for their continued encouragement and my wife, Kanthi, for her continued help and her understanding during the course of this work.

DECLARATION

This dissertation is submitted to the University of Warwick in support of my application for admission to the degree of Doctor of Philosophy. It contains an account of my own work performed at the Department of Physics at the University of Warwick during the period of October 1976 to September 1979 under the general supervision of Dr. M. H. Lewis. No part of this dissertation has been used previously in a degree thesis submitted to this or any other University. The work described in this thesis is the result of my own independent research except where specifically acknowledged in the text.

B. S. B. Karunaratne

January 1980

ABSTRACT

The broad aim of this research programme was to understand the structure, deformation and fracture processes associated with grain boundaries in nominally single phase β′ Si-Al-O-N ceramics, hot-pressed with different sintering aids (MgO and Mn_3O_4).

The major microstructural difference between the two types of ceramic is the occurence of microscopic regions of triple-junction silicate glass in the Mn-containing ceramic. Lattice imaging shows that there is no resolvable phase within two-grain interfaces in both ceramics down to an approximate limit set by the prism-plane spacing of Si-Al-O-N crystals (6.6 Å). However, Auger electron spectroscopy indicates the presence of Mg, Mn, O and impurity Ca at grain boundaries.

Creep tests have been performed in a newly designed and constructed apparatus which can easily be adapted to perform bend and uniaxial compressive creep. A double-torsion jig has been constructed to determine crack propagation data in vacuum.

The dominant deformation mechanism in the Mn-containing ceramic is that of grain boundary sliding accompanied by cavitation at triple junctions nucleated within the silicate phase. The measured non-integral stress exponent ($n \simeq 1.5$) and activation energy ($Q \simeq 490$ k $Jmol^{-1}$) in the creep rate equation $\dot{\varepsilon} = \text{const.}\ \sigma^n \exp\left(-\frac{Q}{RT}\right)$ are typical of commercial Si_3N_4 ceramics. A similar cavity-interlinkage is the principal mechanism for subcritical crack growth, characterised by a low value for the stress intensity (K_I) exponent (n) in the relation V(crack velocity) = const. K_I^n.

Triple junction silicate, and hence cavitation, is absent in the Mg-containing ceramic, which exhibits a grain boundary diffusional (Coble) creep mechanism ($n \simeq 1$). Subcritical crack growth is restricted to a narrow range of K_I and shows a higher K_I-exponent ($n \sim 13$) which favours a diffusive crack growth mechanism.

The influence of heat-treatment on high-temperature creep and subcritical crack growth has been analysed from microstructural evidence and determination of creep and crack growth parameters. Extraction of impurities (Mg, Mn, Ca etc.) from grain boundaries into a surface oxide film and consequent crystallisation of remaining glass components as β′ Si-Al-O-N, results in marked improvement in creep and resistance to subcritical crack growth. The most significant change is the elimination

of triple-junction glass and hence suppression of cavitation during creep and the cavity-interlinkage mechanism for slow crack growth in the Mn-containing ceramics. A creep mechanism of grain boundary diffusion is characterised by stress exponent $n \approx 1$ and high activation energy > 800 k $Jmol^{-1}$. The slow crack growth behaviour favours a diffusive crack growth mechanism or that of a thermally-activated bond breaking.

TABLE OF CONTENTS

LIST OF FIGURES

LIST OF TABLES

CHAPTER ONE

INTRODUCTION

With the development of advanced heat engines (e.g. Gas turbines for electricity generation, aircraft engines and for vehicle propulsion) mechanical engineering entered a new high temperature field which has increased the demand for high temperature structural materials. The improvements in metallic alloys and coated refractory metals have shown that they are unsuitable for temperatures at which the new engines are required to operate for a higher efficiency.

The most obvious approach to achieving good high temperature engineering properties is to select a material with a high melting point and good ancillary thermal properties such as high oxidation, corrosion and thermal shock resistance. Most of these properties are inherent in many ceramics, particularly many metallic oxides, nitrides and carbides. Operating at higher temperatures with uncooled ceramic components (present maximum about 1000^{o}C with air cooling) gas turbines will give improved efficiency and better power to weight ratio with less fuel consumption. The possibility of using lower grade fuels, less pollution and also the possible lower cost of ceramics compared to nickel and cobalt superalloys have accelerated this interest. The primary reasons for the limited application of ceramics are their brittleness, low thermal shock resistance and difficulty in fabrication. However the new ceramic materials developed in recent years, are overcoming the traditional aversion to ceramics in structural applications. Currently, substantial research programmes are in progress to investigate the feasibility of ceramic materials for high temperature structural applications. The choice of a material for high temperature applications is not entirely

governed by its load-bearing capacity. Apart from high oxidation and corrosion resistance they must have very low thermal expansion coefficients or high thermal conductivity to avoid thermal shock failures arising from temperature gradients and sudden temperature changes.

Ceramics with potential for high temperature applications are listed in Table 1.1 with their relevant properties and will be briefly discussed.

1.1 High Temperature Ceramics

Alumina was one of the pure oxide ceramics first developed and is now produced in a range of shapes and sizes. Although the high temperature strength (Table 1.1) and good corrosion resistance of dense polycrystalline alumina are attractive, the relatively high expansion coefficient and low thermal conductivity result in poor thermal shock resistance and makes it unsuitable for many high temperature structural applications.

Following the development of glass ceramics by Stookey (1954) a range of such materials has been developed for various applications such as domestic oven ware, infra-red gas burners and regenerative heat-exchangers in small gas turbine engines. Thermal expansion coefficient varies according to the composition and heat-treatment, but is low compared to the other ceramics, and therefore these materials have an excellent thermal shock resistance. However these materials have upper working temperatures of about 900^{o}C and some are susceptible to attack by sea-salt at high temperatures [1]. This makes these materials relatively unattractive for high temperature applications. The relatively low melting temperature of residual phases in this material is thought to be responsible for this high temperature strength degradation.

Property	Alumina	Glass Ceramics	Silicon Nitride		Silicon Carbide	
			Reaction-bonded	Hot-pressed	Self-bonded	Hot-pressed
Density (ρ) kg m^{-3} x 10^3	4.0	2.5 - 2.8	2.4 - 2.6	3.1 - 3.2	3.1	3.2 - 3.3
Melting or Decomposition (D) K	2320	> 1700	2170 (D)	2170 (D)	3000 (D)	3000 (D)
Young's Modulus (Y) GNm^{-2}(at 300K)	360	90 - 160	138 - 220	310	351 - 420	386 - 452
*Rupture Modulus MNm^{-2}(at 300K)	400 - 500	80 - 180	150 - 215	500 - 900	200 - 400	500 - 650
Poisson's Ratio ν			0.25 - 0.27	0.27 - 0.29	$\sim$ 0.24	0.16 - 0.17
Thermal expansion coefficient α 10^{-6} K^{-1}	6.9	0.7 - 6.6	2.8	3.1	4.3	
Thermal conductivity Wm^{-1} K^{-1} at 1000 K	7	2.0 - 3.6	4	16	59	

* Four-point bend strength

Table 1.1: Properties of Ceramics with potential for high temperature applications (data from [1] and [4]).

As mentioned earlier, materials with high melting temperatures must have high strength retension at elevated temperatures. Covalently bonded solids have high bond strength and therefore have very high melting or decomposition temperatures. Silicon nitride and silicon carbide possess many attractive high temperature properties dictated by their covalent bonding and are leading candidates as high temperature structural materials.

Silicon nitride exists in two modifications [2] α and β, both having hexagonal crystal structures. The unit cell dimensions are given in Table 1.2. The structural unit is the SiN_4 tetrahedron in which each silicon atom is covalently bonded to four nitrogen atoms (similar to the silicate tetrahedral unit SiO_4). The β form is composed of SiN_4 tetrahedra sharing corners, (see Fig. 1.1) each nitrogen corner being common to three tetrahedra . α-Si_3N_4 is built up in a similar way from SiN_4 tetrahedra, but has an elongated structure (Lattice parameter c is nearly twice that of β-Si_3N_4). In the α form it is believed [3] that approximately one in every thirty nitrogen atoms is replaced by oxygen and to maintain electrical neutrality the equivalent number of silicon sites remain vacant.

Lattice Parameters	α-Si_3N_4	β-Si_3N_4
a (nm)	0.7753	0.7608
c (nm)	0.5617	0.2911

Table 1.2. The unit cell dimensions of the two forms of Si_3N_4 [4]

The self-diffusivities of pure Si_3N_4 and SiC are likely to be very small because of the covalent nature of their bonding, hence they are not easily densified by high temperature solid-state sintering used for oxide ceramics. Therefore silicon nitride ceramics were initially

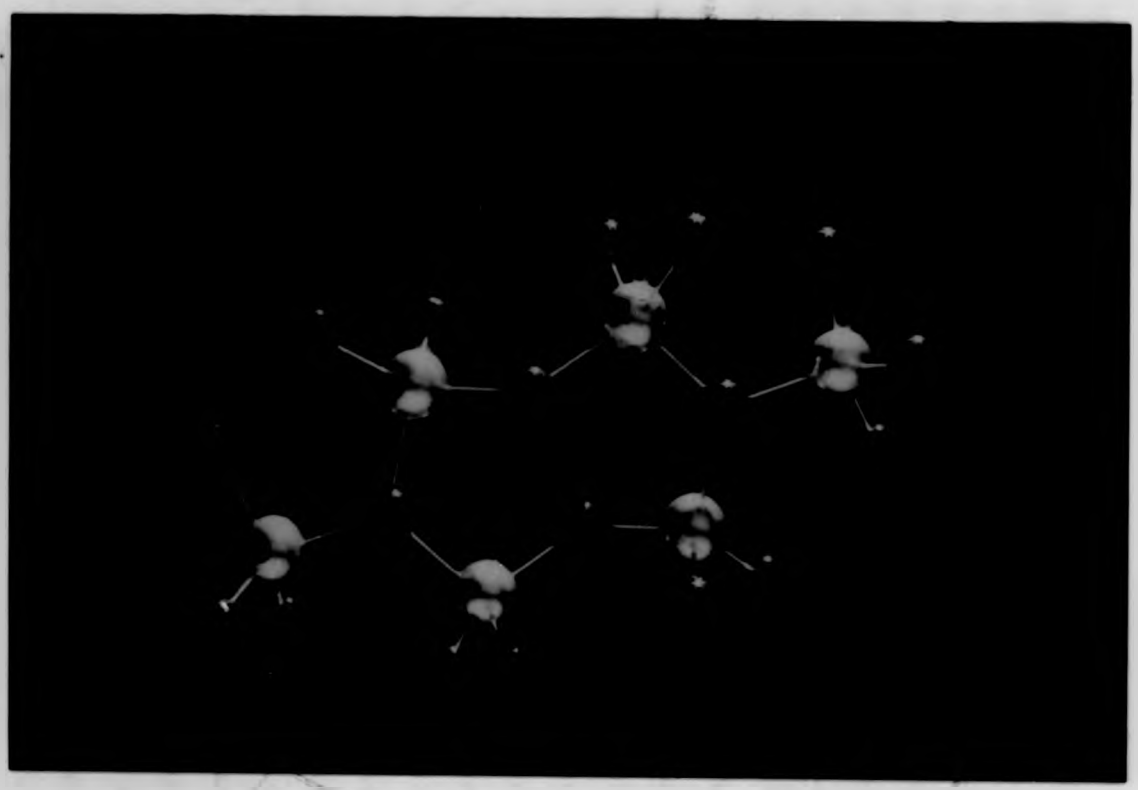

Fig. 1·1 $\beta - Si_3N_4$ Crystal Structure

prepared by nitriding silicon powder at elevated temperatures. This product is known as 'reaction-bonded' or 'reaction-sintered' Si_3N_4 and it contains both α and β Si_3N_4. In reaction-bonded materials, the required shape is first made from silicon powder (by isostatic pressing [5], flame spraying [6], slip casting [7] and injection moulding [8] etc). which is then nitrided in molecular nitrogen at about 1500°C. However there is a limit of about 10 mm to the section thickness [4] which can be nitrided. Normally the compacted silicon powder is partially nitrided to a machinable compact which is then machined to the final shape and is further nitrided for higher density. The original dimension of the machined compact remains virtually unchanged during the final nitriding, because the shrinkage due to the elimination of pores is closely matched by the volume expansion on conversion of silicon to silicon nitride and hence quite complex shapes can be obtained. However the final product contains about 25% porosity and therefore the components of this material are unsuitable for high stress-temperature engineering applications.

The work of Popper [9] showed that dense SiC could be produced by mixing SiC powder with a small amount of carbon and infiltering molten silicon, which bonds the grains together through a reaction and is known as "self-bonded" SiC. The dimensional change during the reaction is negligible and therefore has a fabrication advantage similar to reaction-bonded Si_3N_4. Different forms of self-bonded SiC are produced commercially (e.g. "Refel" SiC, KT SiC etc.) and they contain varying amounts of free silicon and free carbon. The strength of these materials at low temperatures is superior to that of reaction-bonded Si_3N_4 ceramics but melting of unreacted silicon causes a large drop in strength [4] at about 1400°C. Very strong SiC has been produced by hot-pressing SiC powder with small amounts of Al_2O_3 (~ 2% volume) at 2200°C [4]. These materials

also exhibited strength degradation at high temperatures ($\sim 1300^{o}C$) and softening of grain boundary phase has been suggested as the reason for this [10].

1.2 Hot-pressed Silicon Nitride (HPSN)

In an attempt to obtain high density and high strength materials, in 1961 Deeley et al [11] discovered that fully dense Si_3N_4 could be produced by hot-pressing α-Si_3N_4 powder with a small amount of MgO (1% - 5%) as an additive. Typically the powder is hot-pressed ($\sim$ 15 MNm^{-2}) for one hour at a temperature about $1800^{o}C$ to give a fine grained product (0.1-2 μm) of full density with fully transformed β-Si_3N_4. The details of the manufacturing process have been discussed by Lumby et al [12]. Fully dense (3.18 Mgm^{-3}) HPSN are available commercially with very high strength ($\sim$ 900 MNm^{-2}). These materials are very hard and complex shapes have to be diamond machined.

The mechanism for conversion of elongated α-Si_3N_4 to equiaxed β-Si_3N_4 and the role of MgO during the hot-pressing were not well understood until recently [13,14]. It was suggested that the MgO additive reacts with free surface silica on α-Si_3N_4 particles to form a Mg-rich silicate. Si and N atoms from α-Si_3N_4 are dissolved in this silicate liquid and reprecipitated as β-Si_3N_4, leaving a residual grain boundary silicate phase. The transmission electron microscopic observation [14] of most β grains with faceted shapes and the presence of intergranular glass provided a strong evidence for this liquid phase densification. The impurities (Ca, Al etc.) present in the initial materials may reduce the liquidus temperature and will accelerate densification. However, further studies [10,15,16] indicate that the impurities, in particular

Ca, in the starting materials are detrimental to high temperature properties of HPSN. Evidence [10,17,18,19] suggests that the observed strength degradation above 1000°C in HPSN is due to the presence of the grain boundary phase which becomes a viscous fluid at high temperature allowing grain boundary sliding and associated slow crack growth.

At this point, the central problem faced by researchers was to find a way to eliminate the grain boundary phase or to make it more refractory. In attempting to obtain materials without the grain boundary phase a different manufacturing route was used. Thin layers (maximum $\sim$ 1 mm) of Si_3N_4 [20] and SiC [21] have been produced by chemical vapour deposition (C.V.D.) in the temperature range 1200°C - 1800°C. The C.V.D. materials are still at an experimental stage and the mechanical strength is not yet satisfactory.

Two approaches have been used to make the grain boundary phase more refractory. The first approach was to reduce the amount of impurities, in particular Ca, in the starting materials. This has led to the production of various high purity commercial grades such as HS130 and NC 132 (Norton Co.). The high purity HPSN showed some improvement in high temperature strength. However the properties of the low-impurity silicate phase (Mg-silicate) remained the limiting factor and gave rise to a fall in strength [4] above a critical temperature (1200°C). The second approach was to improve the refractoriness of the boundary phase by using a hot-pressed additive such as Y_2O_3 [22]. To obtain a maximum strength it was found that larger amounts (10-15% Y_2O_3) of refractory additives are needed for hot-pressing. Although some improved properties have been demonstrated for the Si_3N_4 - Y_2O_3 additive system, a problem with strength degradation at 1000°C has been reported and further studies [23,24] have shown that this behaviour is due to cracking of specimens

arising from severe oxidation of this refractory phase at 1000°C.

Therefore it is clear that high temperature strength of these strong ceramics is ultimately controlled by their relatively weak grain boundary phase. This phase mainly contains the metallic silicates derived from the hot-pressing and which is essential to obtain high density. However the recent developments in "Sialon" ceramics following the discovery [25,26] of solubility of Al_2O_3 in Si_3N_4 have demonstrated the possibility of producing single phase materials using ceramic alloying techniques.

1.3 Si-Al-O-N Ceramics

"Sialons" are a series of compounds resulting from the substitution of aluminium for silicon and, simultaneously, oxygen for nitrogen within the β-Si_3N_4 crystal structure. This substituted β-Si_3N_4 (subsequently called β') has an hexagonal structure similar to β-Si_3N_4, but with only a small increase in unit cell parameters *a* and *c*. The structural unit [27] of β'-sialon is (Si, Al) $(O,N)_4$.

The early sialon ceramics were prepared either by hot-pressing or pressureless sintering a suitable mixture of the stoichiometric compounds α-Si_3N_4 and Al_2O_3. However these materials were not single phase [28] and Lumby et al [29] showed that by adding an increasing amount of AlN to Si_3N_4-AlN-SiO_2 mixtures, the excess surface SiO_2 can be balanced to give single phase materials. Similarly, mixtures of Si_3N_4, Al_2O_3, SiO_2 and AlN or mixtures of any three components (Fig. 1.2) can be hot-pressed to give single phase β' sialons. (The single phase region is marked β'). These balanced compositions are approximately identifiable with general formula $Si_{6-x}Al_xO_xN_{8-x}$ [29] where x gives the Al substitution level and

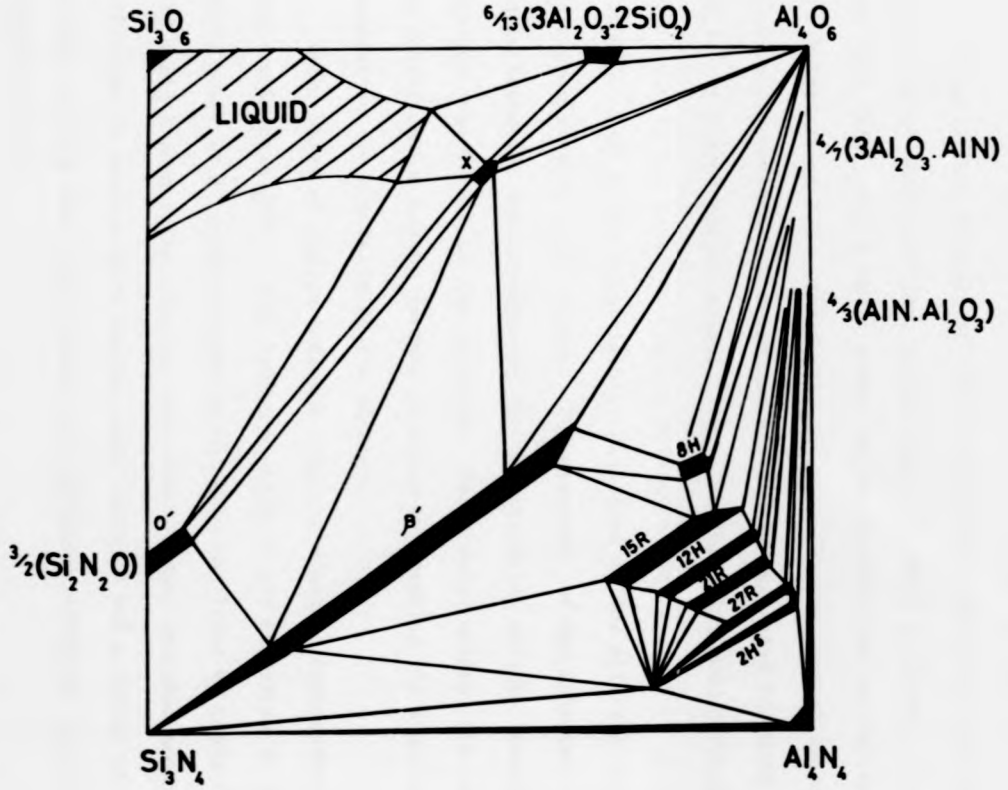

Fig. 1.2: Isothermal Phase Diagram for the System Si_3N_4-AlN-Al_2O_3-SiO_2 at 1760°C [30]

a series of materials can be obtained for different x values up to $x \simeq 4$ (maximum possible Al^{3+} substitution level). The unbalanced compositions would give second phases which were identified [30] as AlN-polytypes (15R, 12H, etc.) and X-phase. (Fig. 1.2)

A significant feature of this balanced composition is the increased difficulty of densification, particulary for small x values. To overcome this difficulty a small amount of metal oxide such as MgO was added as a hot-pressing aid. The densification mechanism is similar to the solution-reprecipitation mechanism previously suggested for HPSN ceramic [13,14] with some modifications [31]. The initial liquid formation is mainly due to the reaction between surface silica and AlN at about $\sim 1600^{o}C$. α-Si_3N_4 is progressively dissolved in the silicate liquid and reprecipitated as β' sialon. The presence of MgO enhances the liquid formation and accelerates the densification rate by lowering the liquidus temperature of the silicate. Using metal oxides such as Mn_3O_4 the densification can be further improved by lowering the liquidus temperature and viscosity of the silicate.

These balanced sialon ceramics showed a dramatic improvement in creep resistance [29]. This indirect evidence for reduction in residual second phase at β' grain boundaries has been confirmed by Lewis et al [31] using transmission electron microscopy. This provided some motivation to produce more single phase ceramics and a series of carefully balanced sialons were hot-pressed with different additives (at Lucas Research Centre).

The present research work has been carried on from this point to understand the structure, deformation and fracture processes associated with grain boundaries in these nominally single phase ceramics composed of intrinsically-strong covalently bonded crystals.

1.4 Objectives of the Research Programme

One of the key questions in ceramic alloy development is the extent to which one can improve intercrystalline cohesion by removing residual grain boundary phases in order to improve mechanical properties and, in particular, the resistance to sub-critical crack growth at elevated temperatures. This microstructural limit has already been approached [31] in hot-pressed sialon ceramics which have a carefully "balanced" O/N ratio to achieve the single phase condition, but with inevitably increased difficulty in densification. It has been shown by Auger spectroscopy [31], that these nominally single-phase β′ materials contain "segregate" intergranular layers which contain atoms of the densifying aid and of accidental impurities. One of these materials (specimen A in the present study) has been shown previously [32] to retain the problem of sub-critical crack growth above a threshold temperature which shows little improvement over the earlier silicon-nitrides which contain an intergranular glass phase. However, the preliminary K_{1c}-temperature study in the present programme revealed a marked difference in behaviour between the single phase sialon ceramics with different additives. This indicated that this difference in behaviour with additive chemistry would be clearly demonstrated in crack-propagation (K_I-V), creep behaviour and in high resolution electron microscopy. The aims of this research programme were therefore:

1. To make a detailed ultramicrostructural study of the ceramic grain boundary in carefully balanced sialons using (a) conventional diffraction contrast and high resolution lattice imaging of neighbouring grains, and (b) Auger electron spectroscopy of intergranular fracture surfaces.

2. To identify the high temperature deformation mechanisms for sialon ceramics with different additives via, determination of creep parameters (stress exponent - n and activation energy for creep - Q), examination of the microstructure of creep specimens, and to correlate with the grain boundary structure and chemistry analysed in (1).

3. To determine the influence of additive/segregate type and concentration on the susceptibility to sub-critical crack growth and on the magnitude of K_{1c}. To determine the fracture mechanisms in detail it was hoped to extend this study to determine crack propagation data (stress intensity exponent - n and activation energy for crack propagation - Q) over a temperature range close to the decomposition point of these materials and to correlate with the microstructure obtained in (1).

4. Finally, combining (1), (2) and (3) to answer the key question raised at the beginning of this section and to make some suggestions for further development of these ceramics with improved high temperature properties.

CHAPTER TWO

A REVIEW OF HIGH TEMPERATURE DEFORMATION AND FRACTURE OF CERAMICS

In this chapter various high temperature creep and fracture mechanisms are discussed, with their application to different ceramic systems. In creep the main emphasis is given to diffusional mechanisms because they are the most probable rate-controlling mechanisms operating in fine-grained ceramics with low dislocation mobility, similar to materials studied in this programme.

2.1 High Temperature Creep

The plastic deformation of a material over extended periods, under the action of a constant load, which is often considerably less than the fracture level, is called creep. This time-dependent deformation occurs in ceramics mainly at elevated temperatures, and usually follows the form generally accepted for metals. A transient or primary creep, in which the creep rate decreases with time, is followed by a steady-state period where the creep rate is constant. There may be a short third region of accelerating creep prior to the failure of the material. In some instances polycrystalline ceramics may exhibit steady state behaviour immediately on application of the load without a primary stage. Creep curves of this type are characteristic of deformation mechanisms, which do not require the formation of substructure, such as diffusional creep. This behaviour has been observed in polycrystalline NaCl [33].

Primary stage creep is often small compared to steady-state creep, which may extend over a long period of time before failure, under typical

stress and temperature conditions for a structural component. Therefore a better knowledge of the precise deformation mechanism occurring during steady state creep is essential. Laboratory creep tests are normally undertaken to correlate the steady-state creep behaviour with that predicted by one of several specific creep mechanisms.

2.1.1 Deformation Mechanisms

A polycrystalline ceramic material can undergo deformation by several different mechanisms. If the temperature is high enough it may deform by diffusional flow of matter from boundaries which are under compression to those under tension. In 1948 Nabarro [34] and in 1950 Herring [35] analysed the problem of grain elongation by stress directed lattice diffusion and obtained the following relation for steady state creep rate ($\dot{\varepsilon}$) of a polycrystalline solid.

$$\dot{\varepsilon} = \frac{14\Omega D_\ell \sigma}{kTd^2} \qquad (2.1)$$

where σ is the stress, D_ℓ is the lattice diffusion coefficient, Ω the molecular volume, d grain size and kT has it's usual meaning. In 1963 Coble [36] made a similar calculation, but assumed diffusion along the grain boundary and obtained the following relation for steady state creep rate.

$$\dot{\varepsilon} = \frac{14\pi\sigma\Omega\delta D_b}{kTd^3} \qquad (2.2)$$

where D_b is the grain boundary diffusion coefficient and δ is the effective grain boundary width. Coble creep has a stronger grain size dependence than Nabarro-Herring creep, but a similar linear stress dependence. Nabarro-Herring and Coble creep have been reported for many

polycrystalline ceramics. (See Table 2.1).

However, Nabarro, Herring and Coble only considered the creep of a single grain in a polycrystalline solid. In 1963 Lifshitz [37] analysed diffusional flow in a dense aggregate of grains and showed that grain boundary sliding is required to maintain compatibility at all grain boundaries. Raj and Ashby [38]have studied this process of sliding with diffusional accommodation and obtained identical relations for Nabarro-Herring and Coble creep. They pointed out that the stress directed diffusion and sliding processes are not independent. For boundary sliding to occur, it must be accommodated by diffusional deformation of grains.

According to the above creep models stress-directed diffusional flow will cause grain elongation and increase the diffusion distances which may result in a gradual effective hardening as deformation proceeds. It has been shown by Ashby and Verrall [39], based on a "diffusion-accommodated flow" model, that the polycrystals could undergo deformation without elongating their grains, if significant rearrangement of the grains occur by changing their neighbours and rotating. In this model, the volume of matter transported by diffusion per unit strain and diffusion distance are far less than that for earlier models and therefore the creep rate is faster. The strain rate expression was similar to Nabarro-Herring and Coble equations, but the coefficient was higher by a factor of about 7. Several other models [40,41] have been suggested to explain the topological changes during diffusional creep. However in a real polycrystal, in three dimensions, the grain rearrangement may be much more complicated than described in these models. Ashby and Verral claimed that their idealized model contains the essential physics involved in a real case even though the exact calculations are exceedingly difficult.

A number of qualitative features of this model appear to be supported by experiment [42,43].

The initial consideration of diffusional creep was for single component materials and so the theories were most directly applicable to pure metals. However these theories can be applied to ceramic systems by using effective diffusivities and atomic volumes [44,45]. In oxide ceramics both cations and anions must participate in the diffusive process and, in the steady state condition, the total flux of the two components must be in the stoichiometric ratio [44,45]. The other complication is that the two atomic species may diffuse along different paths. The observed creep rate is then determined by the movement of the slower diffusing species along the fastest diffusion path. Hence four possible rate controlling mechanisms exist in the diffusional creep of two component materials (e.g. MgO, Al_2O_3, NaCl) and the temperature and grain size determines which mechanism will be dominant.

As the stress is increased at high temperatures dislocations become mobile and the creep rates will obey a 'power-law' relationship rather than a linear stress dependence. In this region the creep rate is controlled by dislocation mechanisms such as glide and climb and the steady state creep rate can be well described by the semi-empirical power law equation [46]

$$\dot{\varepsilon} = \frac{A\, D_v\, Gb}{kT} \left(\frac{\sigma}{G}\right)^n \qquad (2.3)$$

where G is the shear modulus, b is the Burger's vector and D_v the bulk diffusion coefficient. The stress exponent n has been related to the nature of specific dislocation creep mechanisms [46-48] and n values normally found to vary from ~ 3 to ~ 5. There is no grain-size dependence in dislocation creep.

Polycrystalline ceramics can therefore deform by a number of different processes, depending on the microstructure (grain size etc.) and the range of stress and temperature considered.

2.1.2 Deformation Mechanism Maps

A useful way of presenting this data is in the form of a diagram which is generally known as a 'deformation mechanism map'. There are three different types of maps based on, (i) constant grain size, (ii) constant temperature and (iii) constant stress. These maps can be constructed using actual creep data or theoretical equations for each process if the requisite diffusion parameters are known. Detailed procedures of constructing these maps have been described elsewhere [49-52]. Fig. 2.1 is a constant grain size (10 μm) map for polycrystalline MgO [53] and normalized shear stress τ/G (G-shear modulus) is plotted as a function of homologous temperature T/T_m (T_m - absolute melting temperature). The deformation mechanisms which are dominant in a particular stress-temperature region are shown as fields. The heavy lines on the map are the boundaries between fields, and these are the loci of points where the two adjacent deformation mechanisms have equal strain rates. The thin lines are contours of constant strain rate.

It can be seen that at high stress levels (shear stress > 5×10^{-3}G) the dominant deformation process in polycrystalline MgO is controlled by dislocation movement. At stress levels below this, movement of dislocation is difficult and deformation is controlled by diffusional mechanisms. The diffusional creep process changes from Nabarro-Herring (O^{2-} lattice diffusion) at high temperatures to Coble creep (O^{2-} and Mg^{2+} boundary diffusion) at temperatures below 0.42 T_m. Generally this transition temperature increases with decreasing grain size due to strong grain

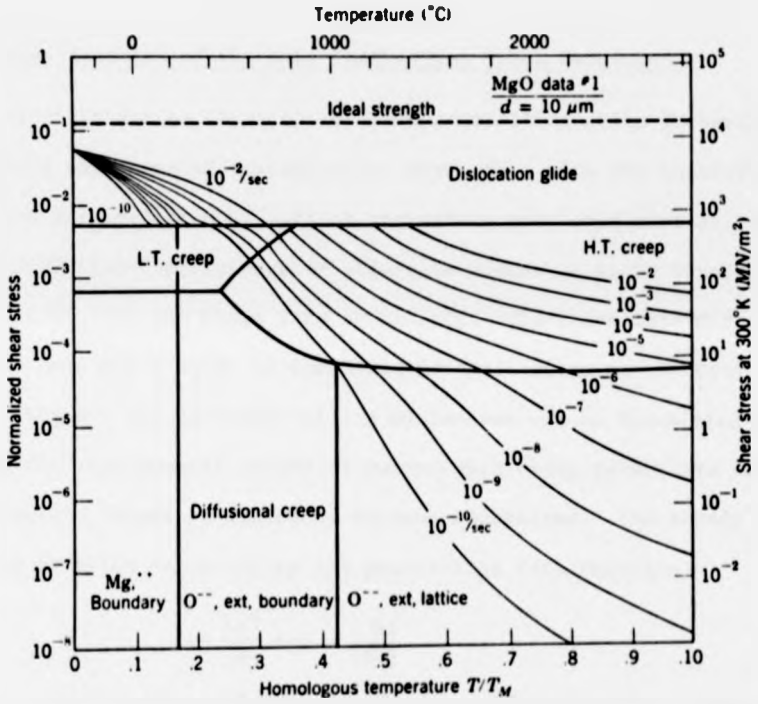

Fig. 2.1: Deformation mechanism map for MgO at a constant grain size of 10 μm [53].

size dependence of Coble creep. In this way a considerable amount of information can be presented on a single diagram. For given stress and temperature the map gives both the steady-state creep rate and the rate controlling mechanism.

2.1.3 Identification of the Rate Controlling Creep Mechanism

It is difficult to identify the rate controlling creep mechanism by comparing experimental stready state creep rate with the theoretical rates which are predicted by various mechanisms mentioned earlier. For example, diffusion coefficients or effective widths of grain boundary for Coble creep are not known very accurately. Therefore this direct comparison does not provide an immediate identification of the creep process. However the rate-controlling mechanisms can be identified by comparing the experimental values of macroscopic creep parameters with the theoretical values predicted by various mechanisms. The steady state creep rate is often expressed by the generalised rate equation

$$\dot{\varepsilon} = \frac{A\sigma^n}{d^m} \exp - \left(\frac{Q}{RT}\right) \qquad (2.4)$$

where Q is the apparent activation energy (which contains the diffusion term D) for the creep mechanism, n and m are stress (σ) and grain size (d) exponents, respectively. A is a constant and RT has it s usual meaning. Particular integer values of n and m charcterise different creep mechanisms (Eq. 2.1 - 2.3). These integer values together with examples for each creep mechanism are summarized in Table 2.1.

n	m	Rate Controlling Creep Mechanism	Examples with References
1	2	Nabarro-Herring	MgO [54-58], BeO [59], Al_2O_3 [60,61], UO_2 [43]
1	3	Coble	MgO [58-63] (Fine grained Fe-doped) SiC [64], UO_2 [43] (Fine grained) NaCl [33] (coarse grained) Al_2O_3 [65,66] (coarse grained)
∿3	0	Dislocation Movements	MgO [67-70], Al_2O_3 [71,72], BeO [73] UC [74]
∿5	0	Dislocation Movements	KCl [75] LiF [76]

Table 2.1: Predicted values of n and m for various creep mechanisms and examples.

(If the grain boundaries do not act as perfect sources and sinks for vacancies, exponent values may change in diffusional creep to n = 2, m = 1 at very low stresses and deformation becomes interface-reaction controlled [77,78,39]).

Experimentally n is determined by obtaining the dependence of creep rate on stress, keeping other variables constant in equation 2.4. Similarly m can be determined if it is possible to vary the average grain size of the test material. Finally, the atomic species which controls the diffusion process can be identified by comparing the creep activation energy with that for the diffusion process. There are several problems associated with this comparison because of the uncertainty of diffusion coefficients for many ceramic systems.

2.1.4. Creep Deformation of Related Polycrystalline Ceramics

A substantial amount of data exists on creep of polycrystalline ceramics, particularly pure and doped polycrystalline MgO and Al_2O_3. Different rate-controlling mechanisms have been identified for these two materials under different creep conditions, and are summarised in Tables 2.2a and 2.2b.

(a) MgO

In general, Coble creep has been observed in fine grained Fe-doped materials and Nabarro-Herring creep in intermediate grain size (20 μm) materials at higher temperatures. In most of these tests [56,58] the occurrence of simultaneous grain growth has complicated the interpretation of an exact diffusional mechanism. Some workers [58,84] have reported that impurities, notably Fe^{3+}, promote this diffusional deformation. The trivalent Fe ions increase the vacancy concentration in the MgO crystal (two Fe^{3+} ions replace three Mg^{2+} ions for electrical neutrality) and enhance the diffusivity. In Nabarro-Herring creep the rate-controlling diffusion species appears to be Mg^{2+} ions [56] which is an unexpected behaviour (see the deformation mechanism map Fig. 2.1) since the oxygen ions are known to be the slower diffusing ions in MgO lattice and should therefore be rate controlling. To overcome this anomaly it was suggested that oxygen diffuses along the grain boundary faster than Mg^{2+} diffuses through the lattice [53].

At higher stresses (> 120 MNm^{-2}) and larger grain sizes (> 70 μm) the deformation is dominated by dislocation creep mechanisms characterized by a third-power stress dependence.

Material (MgO)	Grain size μm	Temperature °C	Test mode and Stress MNm^{-2}	Activation Energy k $Jmol^{-1}$	n	m	Mechanism	Reference
Pure	1-3	1180-1220	Bend (4-40)	∿310	∿1	-	Nabarro-Herring	54
Pure	4-50	1200-1500	Bend	∿436	> 1	-	Mg^{2+} lattice diffusion Small amount of dislocation movement and grain growth	56
Pure	2.5 - 5.5	1380-1800	Bend (5-35)	402	1.5		Cavitation observed	55
Pure	5.5 - 20	1380-1800	"	226	∿1	2.5	Nabarro-Herring or Coble	55
Fe-doped	4 - 60	1000-1450	Bend (5-50)	490 - 340	0.97 - 1.39	2-3	Nabarro-Herring or Coble	57, 58, 79
Fe-doped	0.1 - 1	700-1050	Compressive (50 - 140)	403	1.1	2.85	Mg^{2+} boundary diffusion	63
Pure	12 - 52	1200	Compressive (10 - 60)	214	3.3		Dislocation movement	67
Pure	10 - 14	∿1200	"	440	∿3		"	68, 69
Pure	100 - 190	1300-1400	"	319	3.2		"	70

Table 2.2a: Creep data and deformation mechanisms for polycrystalline MgO

Material Al_2O_3	Grain size μm	Temperature °C	Test Mode and stress MNm^{-2}	Activation Energy k J mol^{-1}	n	m	Mechanism	Reference
MgO doped	7-34	1500-1800	Bend (1-70)	-	∿1	∿2	Nabarro-Herring	80
Fe and Ti doped	15-63	1373-1523	"	615	1.1-1.3	-	Al^{3+} lattice diffusion	61
Cr-doped	4-9	"	"	478	∿1.3	-	Al^{3+} lattice diffusion	
Pure	∿18	∿1450		550	∿1.3	1.8	Al^{3+} lattice diffusion	
Cr-doped	15-30	≈1450	"	535	1-1.3	∿2	Al^{3+} lattice diffusion	66
Fe-doped	32-107	∿1450	Compressive	500	0.9-1.29	2.34-2.98	O^{2-} grain boundary	
MgO doped	∿65	1580-1800	"	525	∿1	-	Nabarro-Herring or Coble	65
Pure	15-45	1450-1800	(7-45)	452	1.33	2.68*	Low Stress levels	81
Ni-doped	15-30	"	"	624	0.74-1.98	-	diffusional creep cavitation observed.	
Pure	3-13	1600-1800	Compressive	546	∿1	∿2	Nabarro-Herring	71
Pure	50-100	1600-1800	∿ 10μv	776	∿4		Dislocation movement	
Pure	∿65	1650-1950	" Compressive (6-60 μm)	-	3		Dislocation movement	72

* For grain sizes (2.5-4 μm)

Table 2.2b: Creep data and deformation mechanisms for polycrystalline Al_2O_3.

(b) Al_2O_3

There are many similarities in creep behaviour, between Al_2O_3 and MgO. As in the case with Fe^{3+} doped MgO, Al_2O_3 showed enhanced creep rates [61] with increasing amounts of either divalent or tetravalent impurities [Fe^{2+} and Ti^{4+}]. As expected, trivalent impurities such as Cr_2O_3 added to Al_2O_3 showed similar creep rate to that of pure Al_2O_3 [61]. Many workers have identified Al^{3+} lattice diffusion as rate controlling, which is also contrary to the expected behaviour since O^{2-} is the slower diffusing ion in Al_2O_3. As for MgO this requires faster diffusion of oxygen along the grain boundary.

Crosby et al [81] suggested the possibility of simultaneous operation of several creep mechanisms, due to the non-integral values of both the stress and grain size exponents observed for pure and Ni-doped Al_2O_3. More cavitation and microcracking were observed in Ni-doped material than that in pure material and this has been suggested as the reason for a higher activation energy observed in Ni-doped material. The cavitation could also lead to non-integral stress exponents ($n > 1$). The non-integral values of the grain size exponent ($2 < m < 3$) indicate some mixed contribution of boundary and lattice diffusion to the deformation and this situation could arise if the grain sizes, stress and temperature at which m is determined fall in a transitional region of mechanisms.

As in MgO, at larger grain sizes (> 70 μm) and higher stress the deformation is dominated by dislocation creep mechanisms characterized by third power stress dependence.

(c) SiC

Creep of hot-pressed polycrytalline SiC [64,82] in four point bending has been investigated in the temperature range 1900°C to 2200°C and stresses between 21 MNm^{-2} and 207 MNm^{-2} on 26 μm grain size material. A linear dependence of creep rate on stress and an activation energy of

306 ± 63 kJmol^{-1} was determined for the creep process. Neither grain growth nor cavitation were observed after the deformation. Therefore the authors concluded that the creep process is diffusional and suggested that grain boundary diffusion of carbon is probably rate limiting. Recently Seltzer [83] performed compressive creep on similar commercial material (NC 203) at 1400°C and stresses between 275 - 550 MNm^{-2}. Limited data show that the rate controlling mechanism is diffusional (n = 0.88).

Creep of 'Refel' SiC has been studied by Marshall et al [85] in four-point bending in the temperature range 1000°C - 1200°C and steady-state creep has not been observed. They found a stress exponent n = 1 at 1000°C and n = 2 at higher temperatures. The activation energy for this primary region was 230 ± 80 k J mol^{-1}, and normally lower than that for the secondary region. In this material micro-cracks were observed on the tensile side of the specimen after creep testing. A clear mechanism was not proposed, but it was pointed out that free Si could play a useful role in accommodating grain boundary sliding. A tensile creep study [86] of 'Refel' SiC shows primary and secondary creep between 1200°C and 1400°C, but above 1400°C no creep was detected, and failure was brittle. The derived activation energy from the primary process was very low (117 kJ cal mol^{-1}) and no clear mechanism has been suggested, but it was concluded that creep of 'Refel' SiC is governed by free silicon present between the grains.

2.1.5. Creep in Si_3N_4

Creep behaviour of Silicon Nitride has been studied by several investigators. Kossowsky et al [87] have performed tensile creep on commercial hot-pressed silicon nitrides (Norton HS 130 and HS 110) in different environments. They obtained stress exponents n = 2 at 1149°C

and n = 4.8 at 1315°C in air and n = 3 at 1260°C in He for stresses between 40 - 100 MNm^{-2}, for high purity material (HS 130). Values of the activation energies of 535, 630 and 546 kJ mol^{-1} were obtained for HS 130 tested in air, HS 130 in He and HS 110 in He respectively. The creep mechanism is described as grain boundary sliding of rigid grains controlled by viscous flow of the grain boundary glass phase. This view was supported by the fact that the activation energy for creep deformation is in good agreement with that for viscous flow of silicate glasses ($\sim$ 600 kJ mol^{-1}). This boundary phase was identified [16] as a silicate of magnesium, containing Ca, Al, Na and K,using Auger electron spectroscopy. Many workers [16,88,89] have indicated that dislocation motion in Si_3N_4 is unlikely to occur at temperatures below 1700°C. Evans et al [90] and Kossowsky [91] have observed very low dislocation densities in HPSN using electron microscopy. It has also been observed by Kossowsky et al [87] that there was no change in the density of dislocations before and after creep deformation. They pointed out that if the dislocations were mobile at temperatures below 1400°C their contribution to the total strain could not exceed 10^{-5} which is a few orders of magnitude less than the observed creep strain. Therefore, the non-Newtonian (n > 1) character of sliding was explained as a consequence of local stress increase due to intergranular cavitation. However, the effect of cavitation on temperature variation tests, hence possible higher apparent activation energy has not been considered. They presented a simple model (rigid grains separated by a viscous grain boundary film) and obtained an expression for creep life time and found a reasonable agreement between measured value and predicted value. Based on this model they explained the higher creep rate in air than in He in terms of capillary feeding of surface silicate down the intergranular region.

Four-point bend creep of hot-pressed Si_3N_4 (Norton HS 130) in the temperature region 1200°C - 1400°C has been investigated by Salah Ud din and Nicolson [92]. They have reported an activation energy of 588 kJ mol^{-1} and a stress exponent of 1.7. Triple point voids and, in some cases, adjacent dislocation activity were observed and therefore grain boundary sliding with some accommodation by dislocation movement was suggested as the creep mechanism. They also suggested that the non-integral value of stress exponent is due to this "mixed" mechanism.

Birch and Wilshire [93] and Zeltzer [83] have recently reported results of compression creep tests on HPSN in the temperature range 1300°C - 1400°C. An activation energy of 650 - 700 kJ mol^{-1} and stress exponent of 1.8 to 2.4 have been reported and they are similar to those reported in tension and in bending. The accommodation of sliding by grain boundary microcrack development was described as the rate controlling process. This was further supported by the observation that a ten-fold difference in stress is required to obtain the same creep rate in tension and compression [93,94]. In the compression test the maximum tensile stresses developed are only about one tenth of the applied compressive stress [95] and the formation of grain boundary cavities and cracks depends on the tensile stresses developed across the boundaries.

Creep measurements of reaction bonded Si_3N_4 have shown higher creep strength than hot-pressed material under similar test conditions. Some workers [83,93,96] have reported similar values for n and Q and some [97] have reported slightly lower values for n and Q than hot-pressed materials. However the triple point cavitation and non integral stress exponent values indicate the similar behaviour of the two materials at high temperatures.

2.1.6. Summary

It can be seen that much of the creep data found in the literature for fine grained ceramics is not characterised by exact integer values of n and m. If deformation is accompanied by cavitation (this is the normal behaviour of many ceramics) it would give rise to higher values of n and Q, which may lead to a wrong interpretation of creep mechanism. The occurence of grain growth in some materials during a creep test could add further complications. However, many doubts can be clarified by incorporating electron microscopic observations, particularly examination of the specimens after the creep tests.

2.2. HIGH TEMPERATURE FRACTURE

Two types of fracture normally occur in ceramic materials; brittle fracture and delayed fracture or static fatigue. Brittle fracture occurs by rapid extension of pre-existing flaws at the fracture stress. Delayed fracture is caused by slow extension of flaws, and occurs at stress levels below that for catastrophic failure. Normally, in ceramics, slow crack growth occurs at elevated temperatures, but in some cases it occurs at room temperature in a particular chemical environment.

2.2.1 Fast Fracture

2.2.1 (a) The Concept of the Critical Flaw

The fracture strength of a given material is not in general highly reproducible and depends on the specimen dimensions and test technique. In practice the measured fracture strength is a few orders of magnitude lower than that of the theoretical value. This discrepancy was first explained by Griffith [98] in 1920, pointing out that flaws in brittle materials can act as stress concentrators. This localized stress can exceed the ideal strength of the material and can cause fracture, even under a low applied stress. The fracture strength of brittle materials is therefore determined by pre-existing flaws. In general flaws arise during the preparation of specimens and occur mainly in the surface of the material and are widely and randomly distributed in size, location and orientation. Although the equivalence between grain size and flaw dimension is not well established, a few investigators have reported [99, 100] that this assumption gives good strength correlation. However in Si_3N_4 and SiC the flaw size is much larger than the grain size [4].

The statistical nature of the distribution of flaws explains the scatter of results normally found in the strength of brittle materials. As a result, statistical theories of flaws have received a great deal of attention.

2.2.1 (b) Statistical Approach

The basic concept in the statistical approach is that the specimen fails when the stress intensity at the flaws reaches the critical value for crack propagation. The first important contribution to statistical analysis was made by Weibull [101]. In recent years, progress has been made in incorporating other factors such as microstructure [102] and slow crack growth [103] into Weibull's weakest-link theory.

In Weibull analysis the probability of failure P of a specimen subjected to a stress σ is given by [4]

$$P = 1 - \exp\left[-\int_V \left(\frac{\sigma - \sigma_v}{\sigma_o}\right)^m dv\right]; \quad \sigma > \sigma_v \tag{2.5a}$$

$$P = 0 \qquad ; \quad \sigma \leq \sigma_v \tag{2.5b}$$

where σ_v is a threshold stress below which the failure probability is zero, σ_o is a normalising factor and m is known as the Weibull modulus. m measures the scatter in the strength data and a high value of m describes a more consistent material. Application of this theory to test specimens or to specific components in a standardised way can be achieved by making several assumptions. These assumptions and methods for determination of Weibull parameters from strength data have been discussed by Edington et al [4] and Stanley et al [102].

There are some limitations to the statistical approach [104]. Firstly the random distribution of flaws may vary from specimen to specimen, especially in samples subjected to different treatment, e.g. mechanical polishing, chemical etching etc. Therefore, no generalized statistical theory can be expected to hold for all materials. Secondly,

the most dangerous flaws will lie in the tail of the distribution curve and accuracy of prediction is very low. Finally, the statistical approach does not provide enough information (temperature, environment etc. effects) to understand the physical nature and origin of the fracture process.

2.2.1. (c) Fracture Mechanics Approach

From the critical flaw concept, two approaches have been evolved. The first approach is based on the suggestion that the creation of a new surface is the only mode of energy dissipation when the crack propagates. This approach led to the familiar Griffith equation [98];

$$\sigma_f \propto \frac{1}{y}\left(\frac{\gamma E}{a}\right)^{\frac{1}{2}} \qquad (2.6)$$

where σ_f = fracture stress, E = Young's modulus and y is a geometric factor determined by flaw and specimen geometry and loading configuration. The second approach, which led to a similar equation, considers directly the stress concentration in the vicinity of the tip of a flaw. However Orowan [105] pointed out that in general γ is not the true surface energy as assumed by Griffith, since other energy dissipation mechanisms operate in fracture processes. To avoid this confusion Irwin [106], replaced the surface energy term in the Griffith equation by the strain-energy release rate (or crack-extension force) $\mathcal{G}$, including all possible energy release mechanisms. $\mathcal{G}$ increases with crack length until a critical value $\mathcal{G}_c$ is reached, at which the crack becomes unstable and propagates rapidly in brittle manner. Hence the Griffith relation can be written

$$\sigma_f = \frac{1}{y}\left(\frac{E\mathcal{G}_c}{2a}\right)^{\frac{1}{2}} \qquad (2.7)$$

This analysis was further developed by the introduction of a stress intensity factor K, related to $\mathcal{G}$.

According to fracture mechanics theory the tensile stress normal to the crack plane near the crack tip (r, θ) is given by [107]

$$\sigma = \frac{\sigma_a \cdot \sqrt{\pi a}}{\sqrt{2\pi r}} \cdot \text{Cos}\,\frac{\theta}{2}\left(1 + \sin\frac{\theta}{2} \cdot \sin\frac{3\theta}{2}\right) + \ldots \qquad (2.8)$$

where σ_a is the applied stress and (r, θ) are polar co-ordinates centered at the crack tip.

It can be seen from this equation that the stress intensification near the crack tip is determined by the quantity $\sigma_a\sqrt{\pi a}$. This quantity is defined as stress intensity factor, K. Hence, for a small internal crack in a tensile body:

$$K = \sigma_a\sqrt{\pi a} \qquad (2.9)$$

In general,

$$K = \sigma_q y\sqrt{a} \qquad (2.10)$$

where y is a numerical constant which depends on the geometry of both the loading system and the crack. Therefore, whatever the geometry, the stress field close to the crack tip is entirely characterized by K.

For mode I (Fig. 2.2) crack opening, the stress-intensity factor is denoted by K_1. There are two other modes [104]; Mode II (sliding mode) and Mode III (tearing mode). Most of the crack propagation studies in ceramics have been confined to the opening mode (Mode I).

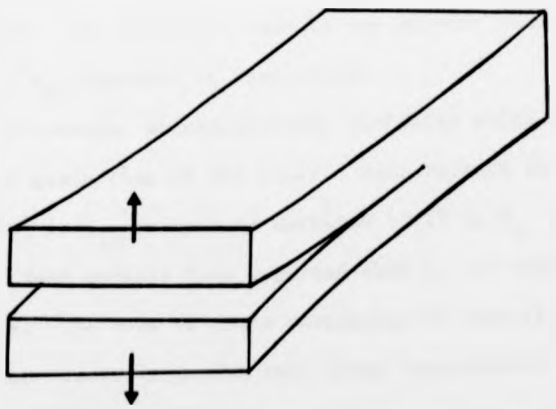

Fig. 2.2. Mode I (opening mode); Normal separation of crack surfaces under the action of tensile stresses.

For the plain strain condition, i.e. mode I crack opening, $\mathcal{G}_1$ and K_1 are related by the equation

$$\mathcal{G}_1 = \frac{(1 - \nu^2)K_1^2}{E} \qquad (2.11)$$

where ν is Poisson's ratio.

K_1 has a direct relationship with $\mathcal{G}_1$ and therefore there will be a critical value K_{1c}, related to $\mathcal{G}_{1c}$ at catastrophic failure.

2.2.1. (d) The Critical Stress Intensity Factor K_{1c}

Both $\mathcal{G}_{1c}$ and K_{1c} measure the resistance of a material to high speed crack propagation. Unlike the "fracture stress" K_{1c} is insensitive to surface flaws and to measurement techniques. Therefore K_{1c} is a true material parameter. In general K_{1c} has received most attention as a parameter to characterise the basic fracture resistance of a pre-cracked specimen, and in comparing fracture toughness of different materials. There are several other alternative parameters such as critical crack opening displacement [108] and J_{1c}-integral [109] which can be used to express fracture mechanics measurements. These parameters are related to K_{1c} and are suitable for materials which exhibit substantial crack-tip plasticity. The materials used in the present study are brittle and hence the K_{1c} approach is appropriate.

There are several microstructural variables which can affect K_{1c}. The effect of grain size is not clear. Data related to this shows an increase [110] in K_{1c} as well as decrease [111] in K_{1c} with increasing grain size. Some workers have reported that K_{1c} is independent [112,113] of grain size. The role of grain morphology is more significant and higher K_{1c} values may result if grains have large length/width ratios. This

has been observed in hot-pressed Si_3N_4 [18] containing elongated α-Si_3N_4, and Al_2O_3 [100] ceramics. Porosity has a relatively small effect on K_{1c} and intergranular porosity generally tends to reduce it [45]. Other variables that effect K_{1c} are impurities, second phases and 'in-situ' transformations which modify the stress intensity at the tip of a propagating crack.

The influence of temperature on K_{1c} has been investigated by several workers on different ceramic materials [19,32,114,115]. A rapid rise in K_{1c} above 1000°C has been observed for most of the materials (SiC [115] has shown a slight decrease above 1000°C). The onset of viscous deformation of the grain boundary phase of these materials above this temperature, is thought to be responsible for this rapid increase and a model has been suggested [116] based on the grain-boundary sliding-assisted slow crack growth.

2.2.2. Slow Fracture

It is well known that brittle materials loaded to stresses lower than the instantaneous fracture strength can fail some time after the application of load. This time-dependence of strength is known as 'delayed-fracture' and occurs in metals, plastics and glasses as well as in ceramics. This phenomenon occurs as a result of slow growth of cracks below the fracture stress. To avoid structural failures it is essential to have thorough understanding of the mechanisms that controls the crack growth and also the extent of crack growth, under the operating conditions. One means of gaining this understanding is through fracture mechanics, and the knowledge can be used to improve the design criteria of structural components and also to develop better materials with high resistance to slow crack growth.

2.2.2. (a) Slow Crack Growth and the K_1-V Relation

The stress intensity factor K_1 at the tip of a inherent flaw under the applied stress (σ_a) increases with crack growth ($K_i = \sigma_a y\sqrt{a}$) and when it reaches the critical value K_{1c}, catastrophic failure occurs. This crack growth below the critical value K_{1c} is often known in the literature as subcritical crack growth or slow crack growth.

The stress intensity factor is the controlling mechanical parameter for crack extension and it has been established that for most slow-crack growth processes there is a unique relationship between crack velocity V and stress intensity factor K_1 at the tip of the crack [117-121]

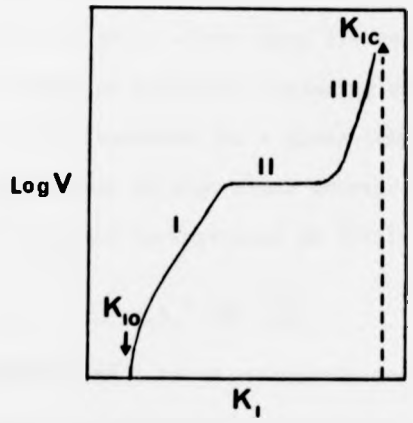

Fig. 2.3. Four regions of slow crack growth in K_1-V diagram.

A maximum of four regions of slow crack growth have been observed in this relationship (Fig. 2.3) prior to catastrophic failure [122]. In many materials a minimum stress intensity (K_{10}) is required to promote slow crack growth [122]. In regions I and III V increases as K_1 increases. Various equations have been suggested to describe the K_1-V relation for

these two regions. Some of these were suggested on the basis of theoretical models of crack growth and others were suggested because they give good empirical fits of the experimental data.

In region II (plateau region) crack growth is stress independent $[V \neq f(K_I)]$. This region is purely due to an environmental effect and diffusion of corrosive species to the crack tip is rate controlling. This region has been observed at low temperatures in many silicate glasses in water [123,124], polycrystalline alumina in humid air and toluene [125], porcelain in water [126], and sapphire in humid air [127].

At elevated temperatures slow crack growth can occur in ceramic materials in the absence of an adverse environment. The empirical relation $V = A K_I^n$ has shown a very good fit for many slow crack growth processes in a variety of materials including ceramics [19,115,125]. Parameters A and n are constant for a given temperature and environment and n measures the extent of slow crack growth. The general form of crack growth relation can be expressed as [115]

$$V = \alpha K_I^n \exp\left(\frac{-Q}{RT}\right) \tag{2.12}$$

where α is a constant and Q is an activation energy for crack propagation.

The parameter n also can be evaluated from indirect experiments such as dynamic fatigue [10] and delayed fracture [114,128].

2.2.2. (b) Failure Prediction

The most important engineering application of a K_I-V diagram is the prediction of failure times of ceramic components under operating conditions. The failure time t_f at constant stress is given by [45]

$$t_f = \frac{2}{\sigma^2 y^2 A(n-2)} \left[\frac{1}{K_{Ii}^{n-2}} - \frac{1}{K_{Ic}^{n-2}}\right] \tag{2.13}$$

where K_{Ii} is the initial stress intensity factor at the most deleterious flaw. Failure time under variable stress, temperature and constant velocity can be obtained in a similar way.

Once the crack propagation data have been obtained (n, A and K_{Ic}) then the failure time is determined only by K_{Ii} or initial flaw size. To evaluate K_{Ii} three basic approaches are available, statistical, flaw detection and proof testing. The proof testing seems to be the most effective technique for ceramic systems [129].

2.2.2. (c) Slow Crack Growth Mechanisms

Several mechanisms have been suggested to explain the high temperature slow crack growth process in polycrystalline ceramics, but the theoretical basis for quantitative prediction of crack growth is not well-established. These mechanisms can be divided into three groups; theories based on (i) crack tip plasticity (ii)diffusional mechanisms and (iii) thermally activated bond rupture.

Two main forms of plasticity related to slow crack growth can occur in ceramic materials; dislocation-assisted slow crack growth and grain boundary sliding - induced slow crack growth. A model for the dislocation-related process has been developed by Evans [116] assuming that grain boundaries act as dislocation sources. However, the K_I-V relation based on this model does not provide a correct quantitative prediction of crack growth. Slow crack growth data obtained on alumina have shown a qualitative consistency with this model [116].

Slow crack growth can also occur, by grain boundary sliding and a model has been suggested by Evans [116] based on sliding of rigid grains separated by a viscous grain boundary film. Grain boundary sliding occurs adjacent to the crack tip due to high tensile stress field and intergranular cracks form ahead of the primary crack. The crack extension

occurs by the linking of these secondary cracks. The detailed analysis led to a functional relationship between V and K_I with the K_I-exponent equivalent to the stress exponent in the sliding equation. This predicted K_I-exponent is rather small compared to experimental values in many ceramics. However this model was used to explain the slow crack growth in Si_3N_4 [19,116], SiC [115] and Al_2O_3 [130] at elevated temperatures.

Mechanisms for subcritical crack growth involving diffusion have been proposed by Stevens and Dutton [131] and by Hasselman [132]. Stevens and Dutton [131] obtained crack growth relations for three possible transport mechanisms (bulk diffusion, surface diffusion, and evaporation/condensation) assuming that the driving force for the crack motion is the difference in chemical potential between the highly stressed atoms at the tip of the crack and those in the bulk of the solid. They compared the theory with high temperature ($950^{o}C$ - $1900^{o}C$) data on alumina and found that at low stress levels the surface diffusion mechanism and at high stress levels the evaporation/condensation mechanism reasonably describe the crack growth behaviour in alumina.

Finally, the thermally activated bond-breaking process is considered as an alternative mechanism for slow crack growth. Thomson et al [133] considered the discrete nature of the atomic configuration at the crack tip. They found that a critical stress is required for a crack extension and a second lower stress for crack healing.The crack is stable between these two stresses and this region is known as the "lattice trapping" region. However, if thermal activation is sufficiently high the trapped crack can move forward by overcoming the barrier resisting the bond rupture.

Although the complete analysis of this approach has not yet been developed it has been suggested that this process is responsible for the vacuum slow crack growth in sapphire [134] and several glasses [135].

2.2.3. Test Methods - K_{Ic} and the K_I-V Relation

There are several test methods available for the determination of K_{Ic} and the K_I-V relationship. Recently, these test methods have been reviewed by Evans [136] and Evans and Langdon [45] and are summarized in table 2.3. These test methods could be selected according to the material availability, machining capabilities and test facilities. Due to simplicity in machining and testing the bend test is widely used in measuring K_{Ic}.

The mathematical relationship between K_I and the experimental parameters of applied load, specimen geometry and elastic constants is obtained either from compliance calibration or analytical methods (finite element method etc). The specimens in which K_I is independent of crack length, (constant K specimens) have extensive application in ceramic systems. Three specimens of this type are available; the tapered cantilever beam [137] the double torsion [138,139] and the constant moment [140]. The simplest specimen to machine and test is the double-torsion which has an advantage in eliminating many difficulties inherent in measuring fracture parameters in ceramic materials at elevated temperature. Conventional slow crack growth measurements require continuous monitoring of crack length, using optical [123,127], electrical resistance [141] and crack opening displacement [142]. None of these methods are suitable for measuring crack velocities at elevated temperatures (> 1000°C). However in the double-torsion technique, simultaneous measurement of K_I and V is possible for a wide range of V. The other test methods impose an additional gripping problem at elevated temperatures. It is not possible to use metallic components (> 1000°C) and ceramic tensile loading systems are expensive. These unique features make the double-torsion specimen attractive for measuring crack propagation data at elevated temperature and in adverse environments.

In the present study, the double torsion and bend specimens have been used and it will be discussed in detail in Chapter 4.

Data Required	Critical Stress Intensity Factor K_{1c}					Crack Growth Rate vs. K_I or ΔK_I	
	Slow Loading Rate				Fast Loading Rate	Ambient Temperature	High Temperature
	Ambient Temperature		High Temperature				
	Porous Material	Non-porous Material	Porous Material	Non-porous Material			
Specimen Configuration	Tapered Cantilever Beam Double Torsion Constant Moment	Double Cantilever Beam Three (Four) point bend Compact Tension Double Torsion	Double Torsion	Three (Four) point bend Double Torsion	Three point bend	Tapered Cantilever beam Double Torsion Constant Moment Double Cantilever beam	Double Torsion

Table 2.3: Fracture Mechanics Test Techniques [45].

Data Required	Critical Stress Intensity Factor K_{1c}					Crack Growth Rate vs. K_I or ΔK_I	
	Slow Loading Rate				Fast Loading Rate		
	Ambient Temperature		High Temperature			Ambient Temperature	High Temperature
	Porous Material	Non-porous Material	Porous Material	Non-porous Material			
Specimen Configuration	Tapered Cantilever Beam Double Torsion Constant Moment	Double Cantilever Beam Three (Four) point bend Compact Tension Double Torsion	Double Torsion	Three (Four) point bend Double Torsion	Three point bend	Tapered Cantilever beam Double Torsion Constant Moment Double Cantilever beam	Double Torsion

Table 2.3: Fracture Mechanics Test Techniques [45].

CHAPTER THREE

MATERIALS AND MICROSTRUCTURAL ANALYSIS

This chapter describes, (i) the chemical composition and fabrication procedures for the Si-Al-O-N ceramics used in the research programme and, (ii) imaging, diffraction and microanalytical techniques used in defining their microstructure.

3.1. Ceramic Compositions and Fabrication

The present research programme is based on two hot-pressed Si-Al-O-N ceramics which have a carefully "balanced" O/N ratio, to achieve the single phase condition corresponding to the substituted β′ crystal composition $Si_{6-x}\ Al_x\ O_x\ N_{8-x}$. Both ceramics have a substitution level of $x \simeq 1$ but differ in the composition of the addition used to enhance the densification process. The first ceramic (separate hot-pressed 'tiles' A and B) contains MgO, Mn_3O_4 (and ZrO_2) additives and the second ceramic (specimen C) contains only a MgO additive. The purpose of adding Mn_3O_4 is to improve the densification further by lowering the liquidus temperature and viscosity of the silicate liquid sintering aid during hot-pressing. The exact chemical compositions and other parameters are summarised in Table 3.1a.

The powder mixtures listed in Table 3.1a were colloid milled in an isopropyl alcohol slurry to effect particle size reduction (mainly for AlN) to < 5 μm and adequate dispersion. The dried powders were hot-pressed in a graphite die at a pressure of 15.4 MNm^{-2} at ∿ 1800°C (The exact holding periods and temperatures are listed in Table 3.1a). These hot-pressed materials have densities which are (within experimental precision of the Archimedian technique) equivalent to the theoretical value based on the lattice parameters (3.14 g cm^{-3}). The hexagonal unit cell parameters (a and c) vary with the Al substitution level (x)

Si-Al-O-N	Si_3N_4	AlN	SiO_2	Al_2O_3	MgO	Mn_3O_4	ZrO_2	Density (ρ) gm cm^{-3}	Lattice Parameters a nm	c nm	x* value	Hot-pressing temperature and Holding periods
A	80.06	13.46	4.87	1.62	0.375	1.5	.2	3.11	0.7647	0.2937	0.99	1800°C 1 hr
B	79.2	13.2	5.7	1.9	0.375	1.5	.2	3.12	-	-	-	1200°C 1 hr 1580°C 1 hr 1780°C 1¼hr
C	79.2	13.2	5.7	1.9	1.0	0	0	3.10	0.7644	0.2938	0.98	1800°C 1 hr

*Aluminium substitution level.

Table 3.1a: Chemical Compositions in wt.% and other Parameters of Si-Al-O-N Ceramic Samples (Supplied by the Lucas Group Research Laboratories).

Si-Al-O-N	Modulus of rupture+ at 20°C (MNm^{-2})	Weibull Modulus at 20°C (m)	% creep* at 1227°C and 77 MNm^{-2}
A	614	12	0.222 (24 hrs)
B	551	8	-
C	518	16	0.103 (48 hrs)

+ Measured in 3-point bending.

* Measured in 4-point bending (Lucas standard creep tests)

Table 3.1b: Mechanical Data (Supplied by the Lucas Group Research Laboratories).

and the substitution level can be obtained from the measured lattice parameter values.

These materials were produced at the Lucas Group Research Centre where the preliminary mechanical strength tests were performed (Table 3.1b). Although the room temperature strength of ceramic C is slightly inferior to that of ceramics A and B, the standard creep test data show a higher creep strength. The high Weibull modulus of ceramic C indicates that this material is more consistent than the other two.

3.2. Microstructural Analysis

3.2.1. Transmission Electron Microscopy

3.2.1. (a) Preparation of Electron-Transparent Sections.

Although the method of preparation of ceramic specimens for Transmission Electron Microscopy (TEM) is now well known it is worth describing the method briefly with a few additional precautions which were taken particularly to produce extensive thin regions ($\sim$ 300 Å) necessary for high-resolution electron microscopy.

Thin slices $\sim$ 0.2 mm thick, were cut from the bulk material using an annular diamond saw and were mounted on glass slides with "Lake side" thermoplastic cement. After grinding on SiC papers (240, 400 and 600 grit respectively) both surfaces were diamond polished (0.25 μm grit) to remove scratch marks and to obtain a uniform thin section $\sim$ 30 μm thick. The thin sections were mounted on 3 mm diameter brass rings with "Araldite" resin. This specimen was mounted in the rotating specimen holder of an ion-beam thinning apparatus and both surfaces of the specimen were

sputtered with 5 kV argon ions at a low angle ($\sim 20^{o}$) to the surfaces. The electron transparent specimen was coated with a thin evaporated carbon film to prevent the build up of static charge on the specimen due to the electron beam.

Most of the lattice and conventional TEM images were obtained using a JEOL 100C microscope (side entry eucentric tilting goniometer stage) operating at 100 kV and fitted with an energy dispersive X-ray analyser (EDAX). Some lattice images were also recorded with a JEOL 100 CX with improved resolution over the 100C instrument. A few low magnification micrographs were taken with a JEOL JEM 200 electron microscope operating at 200 kV with a top-entry double-tilt goniometer stage.

3.2.1. (b) Electron Microscope Imaging

The fine-grained polycrystalline structure is imaged mainly via the different diffracting conditions operating for β' grains in random orientation with respect to the incident electron beam. Fig. 3.1 is a low magnification electron micrograph of ceramic B. This microstructure is almost identical to that previously observed in ceramic A [32]. The average β' grain size is 1.18 μm (based on $\sim$ 500 intercepts) and was determined by the linear intercept method [143]. These β' grains can easily be identified by selected area diffraction and EDAX analysis showed that Al and Si levels are typical of $x \approx 1$ materials. In the Mn containing ceramic (A and B) an inhomogeneous and low density distribution of small particles (0.05 - 0.5 μm) were observed mainly at the grain boundaries (Fig. 3.2). Edax analysis shows that these particles contain varying amounts of Mn, Si, Fe (Fig. 3.3) and occasionally small amounts of Zr (Zr is an additive and Fe is probably due to impurity contamination during the ball milling of the starting particles). As suggested previously [32] these particles may be either transition metal silicates or silicides.

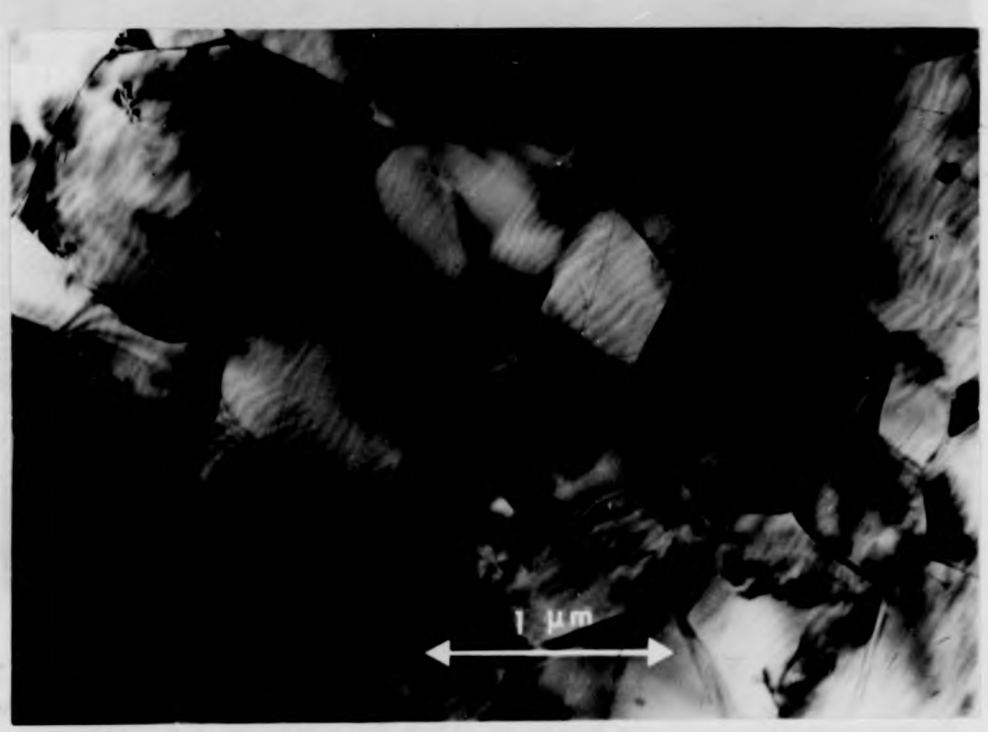

Fig. 3.1: Low magnification T.E.M. showing the general microstructure of Si-Al-O-N B.

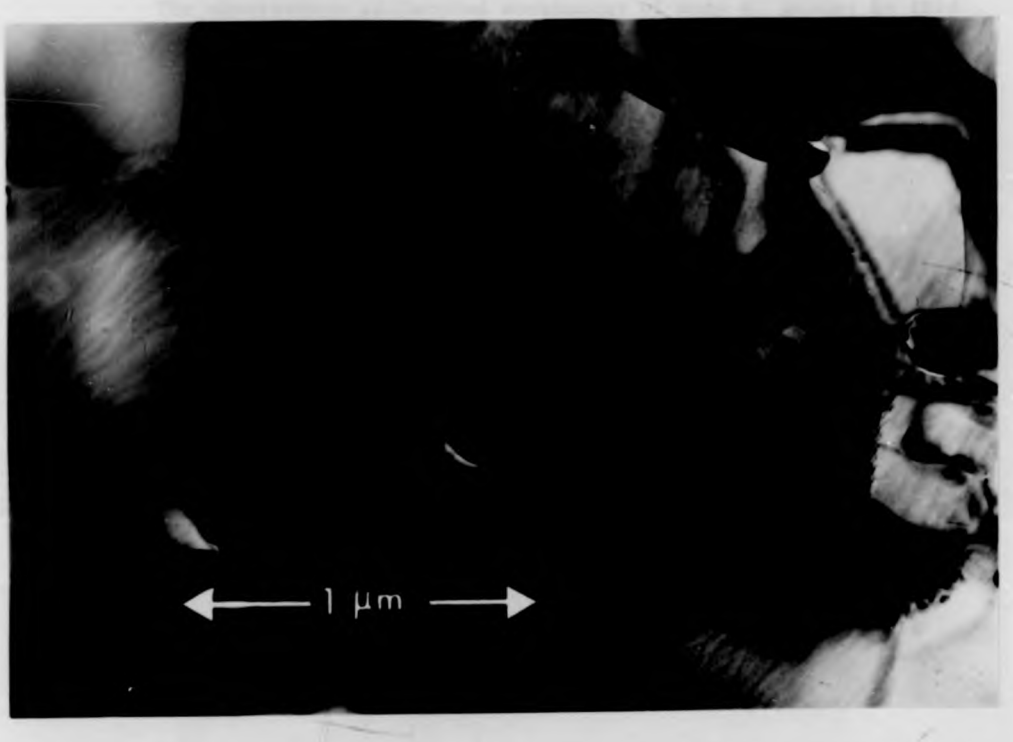

Fig. 3.2: Mn-rich particles in Si-Al-O-N B.

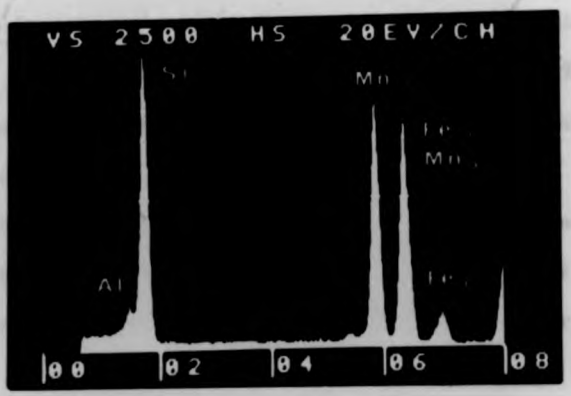

Fig. 3.3: EDAX analysis of Mn-rich particles.

The observation of faceted morphology of many β′ grains in this material indicates that they have grown into a liquid phase at the final stage of sintering. High magnification microscopy has revealed that most of the triple junctions of ceramic A and B contain extremely small amounts (∿ 500 Å) of glass (Fig. 3.4a). Occasionally it was found that some triple junctions contained a larger amount (∿ 1000 Å) of glass (Fig. 3.4b). These non-crystalline regions were identified by their lack of change in diffraction contrast with the specimen tilt. These regions also showed irradiation damage under the electron beam. Similar irradiation damage of glassy regions has been observed [14] in HPSN and in early sialons [28]. Satisfactory EDAX analysis could not be carried out to identify the composition, because these regions were too small. However analysis indicated that the triple junction glass contains Mn and Ca (Al and Si peaks mainly due to the neighbouring grains) (Fig. 3.5).

The microstructure of ceramic C (Fig. 3.6) shows a similar average grain size (1.25 μm) to that of ceramics A and B. However in ceramic C many grain boundaries are smoothly curved interfaces with sharp triple junctions. These features were revealed mainly by thickness contours at the boundaries between diffracting crystals. In contrast to ceramics A and B high magnification microscopy shows (Fig. 3.7) no evidence for the presence of a residual glass phase at triple junctions. The microstructure of ceramic C is very similar to that earlier reported for single phase sialon ceramics [31].

Apart from the triple junctions no visible glass phase was detected between β′ grain boundaries in both ceramics (C, A and B). If a residual glassy phase is present at the grain boundaries of these materials, it must be extremely thin and therefore it is essential to use a very

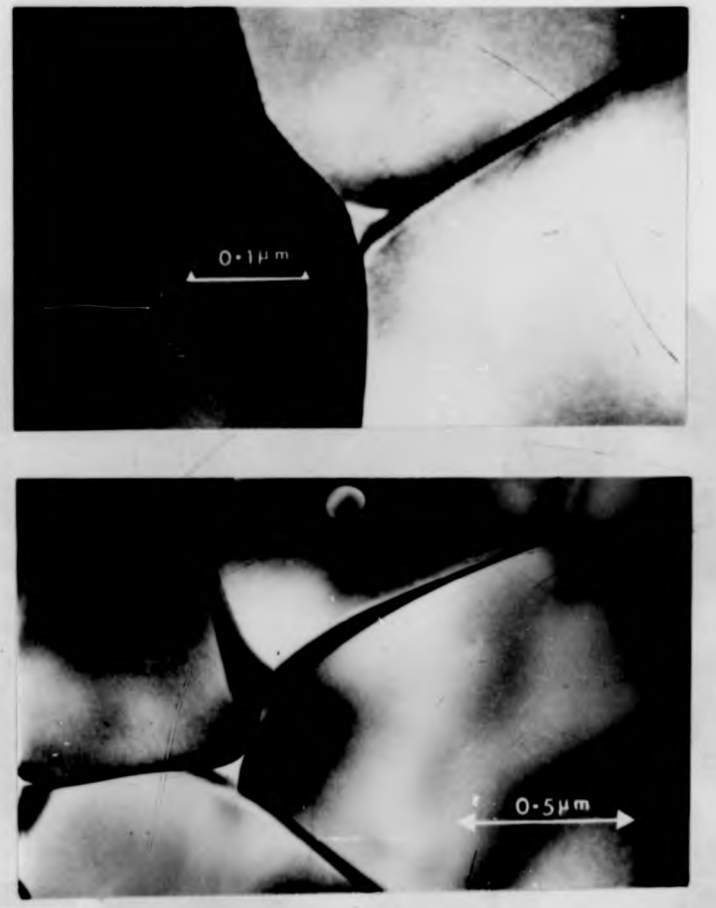

Fig. 3.4: Triple-junction glass in Si-Al-O-N B.

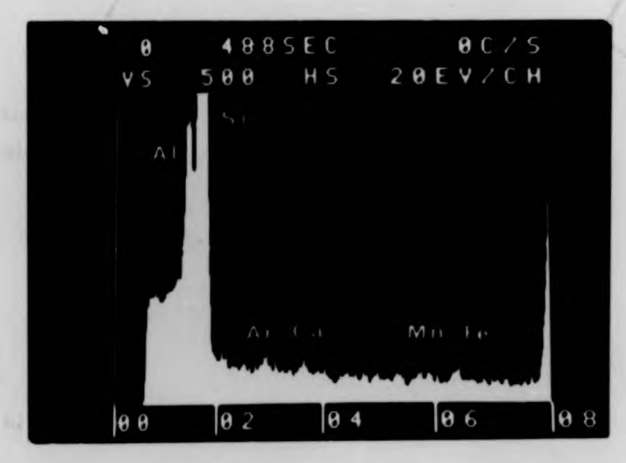

Fig. 3.5: EDAX analysis of triple-junction glass in Si-Al-O-N B.

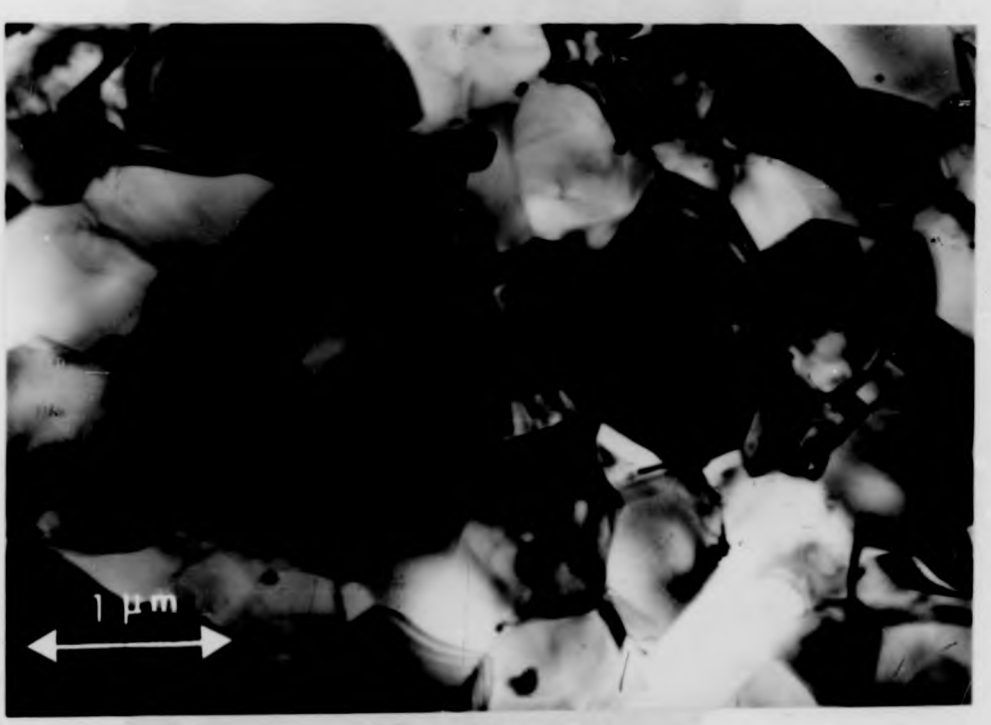

Fig. 3.6: Low magnification T.E.M. showing the general microstructure of Si-Al-O-N C.

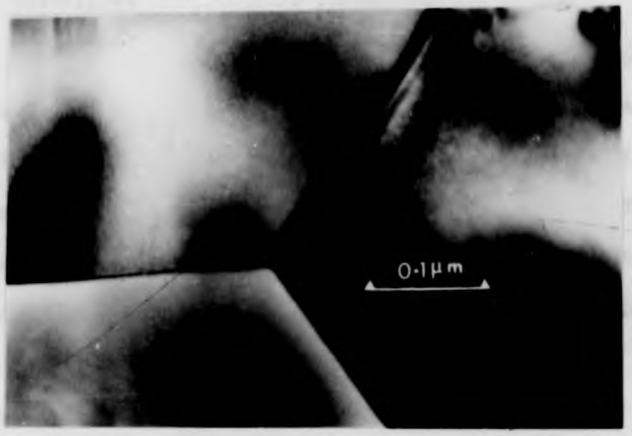

Fig. 3.7: Sharp triple-junctions in Si-Al-O-N C.

high resolution technique such as lattice imaging to detect it.

3.2.1. (c) High-Resolution 'Lattice' Imaging

(i) Principles

If two coherent beams (e.g. the direct beam and one diffracted beam) are selected with the objective aperture to form the image, a fringe image can be generated with a periodicity equal to the spacing between the planes of atoms giving rise to the diffracted beam. The lattice fringes arise from the interference between the two coherent beams. It is also possible to use many diffracted beams together with the direct beam to form "two dimensional" lattice images. The intensity of the lattice fringes depends on the orientation of the diffracting crystal planes and for high visibility of the fringes, the specimen should be in a strong Bragg diffracting condition. Deviation from this condition will also lead to slight variations in fringe spacing [144]. There are several instrumental and specimen-dependent effects such as spherical aberration, chromatic aberration and astigmatism which influence the resolution and contrast of the lattice fringes. Spherical aberration in the objective lens is a major instrumental defect and this introduces a phase delay $\frac{\pi c_s \alpha^4}{2\lambda}$ [145] to the diffracted beam, with respect to the undeviated beam, where c_s is spherical aberration coefficient of the objective lens, λ the wavelength of the electron beam and α is the angle between the diffracted beam and the optic axis. This effect can be minimised by imaging lattice fringes at a certain 'under-focused' (Δf) condition. The relative phase change between the diffracted beam and the undeviated beam due to Δf $\left(\frac{\pi \alpha^2 \Delta f}{\lambda}\right)$ [146] will compensate that due to spherical aberration. However the influence of spherical aberration is very high for off axis beams and therefore in practice only low order

diffracted beams are allowed to reach the image by introducing a suitable objective aperture.

Inelastically scattered electrons from the specimen introduce chromatic aberration effects in the objective lens. However using very thin specimens and thereby reducing inelastic scattering the chromatic effects can be minimised considerably. Thin specimens also increase the image intensity which reduces the exposure time needed for recording the image. This is essential in high resolution microscopy to minimise the effect of specimen drift during the exposure time.

Astigmatism arises from the asymmetry in the objective lens magnetic field (sometimes the specimen itself also introduces some astigmatism) and can be corrected accurately with stigmator controls by observing a uniform 'Fresnel' fringe contrast around the edge of a hole in the specimen.

Considerable gain in the resolution limit can be obtained (via. reducing the spherical and chromatic aberration effects) by tilting the illuminating system of the microscope until the undeviated and the diffracted beams pass symmetrically with respect to the optic axis. Tilted illumination can also be used to produce "dark field" lattice images in which only the diffracted beams contribute to the final image.

In most crystalline materials the interatomic spacing is comparable with the resolution limit of the electron microscope and therefore to obtain lattice fringes it is essential to optimise the conditions mentioned earlier.

It is possible to detect extremely thin residual grain boundary phases in polycrystalline materials by lattice imaging two adjacent grains simultaneously [147]. However, to obtain lattice fringes from two grains the optimum experimental conditions described earlier must be satisfied simultaneously by both grains. Furthermore, to identify the grain boundary phase unambigously it is essential to have the

boundary plane parallel to the electron beam. These conditions make it extremely difficult to apply the technique of lattice imaging to study the grain boundary structure. This technique has previously been used to demonstrate the existence of a grain boundary phase in hot-pressed Si_3N_4 [148,149].

(ii) Procedure and Experimental Observations

Before commencing lattice imaging the alignment of the electron beam was checked and objective lens astigmatism was corrected using a very small hole in the thin area of the specimen. The microscope was then switched to the diffraction mode and the specimen translated under the beam to find a pair of strongly diffracting adjacent grains. Normally prism plane $(10\bar{1}0)$ reflections were selected to produce the lattice images because this prism plane spacing is the largest atomic spacing (6.7 Å) in these materials. The microscope was then switched to the imaging mode to see whether the boundary plane was parallel to the electron beam.

To obtain lattice fringes from both grains a suitable objective aperture (80 μm) was introduced to include only a direct beam and both first order diffracted beams (Fig. 3.8a) or single first order diffracted beams from each grain (Fig. 3.8b). The microscope was then switched back to the imaging mode at high magnification (250,000 x) and lattice fringes were observed on the fluorescent screen with the aid of the binocular viewer. At this magnification the intensity is normally very low and therefore it is advantageous to have a brighter electron gun for high resolution work.

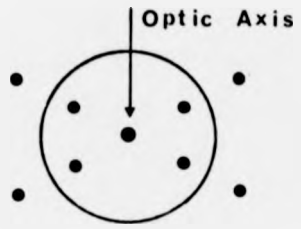

Fig. 3·8 a

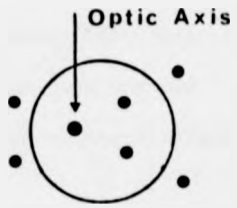

Fig. 3·8 b

At this stage astigmatism was further corrected to give high visibility fringes and the mechanical stability of the specimen was checked. During these operations the same area of the specimen was exposed to the beam for a considerable time and the contamination of the specimen gave rise to an additional problem. However by keeping the cold-trap and the anti-contaminator filled with liquid nitrogen throughout the lattice imaging it was possible to minimize this effect.

After selecting a suitable illumination on the screen (typical exposure times were 5-8 seconds) a 'through-focus' series of images were recorded to obtain the best fringe contrast at the correctly under-focused condition.

In this study the tilted illumination technique was also used for lattice imaging. After obtaining strong diffraction spots from a pair of adjacent grains a suitable objective aperture was introduced such that the direct beam and one first-order diffracted beam from each grain were symmetric with respect to the optic axis (Fig. 3.8c)

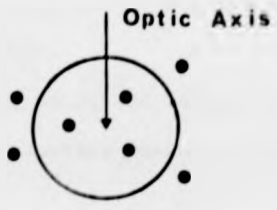

Fig. 3·8 c

As in the case with two dimensional lattice images [145] this method did not show a marked improvement in the resolution for two grain lattice. However this technique gave very high contrast single grain lattice fringes (Fig. 3.9).

Fig. 3.10 and 3.11 are lattice images of ceramic B and C respectively. In Fig. 3.10 the lighter region (marked G) is triple-junction glass. It is evident from the images that the grain boundary 'width' is similar to the atomic spacing of the prism planes. Therefore if a residual glassy phase is present at the boundaries the maximum possible width is about $\sim$ 7 Å. Since this width is comparable with the inter-planar spacing it is also possible that this region is the disordered region between crystalline β' grains. The other interesting feature (observed either via. 'two-grain' or single grain lattice imaging) of the boundaries in Mn-containing ceramics is the high proportion of boundaries parallel to the prism planes of one of the grains (see Fig. 3.10). These faceted (probably low energy) surfaces indicate the retention of a liquid phase at an advanced stage of sintering. Similar types of boundary have been observed [148,149] in HPSN. In contrast, the lattice images of ceramic C showed that the boundaries contain many steps rather than large areas of facet plane parallel to the boundary. This appearance arises from the curved nature of the boundary interface in this material (Fig. 3.11). It can also be seen that only a small region of the boundary plane is parallel to the electron beam. This non-faceting feature is evidence for the absence of a liquid phase at the final stage of sintering. The absence of triple junction glass in this material (Fig. 3.12) is further evidence for this suggestion.

The information obtained by the lattice-imaging technique may be criticised as being too selective because the requirements of parallelism

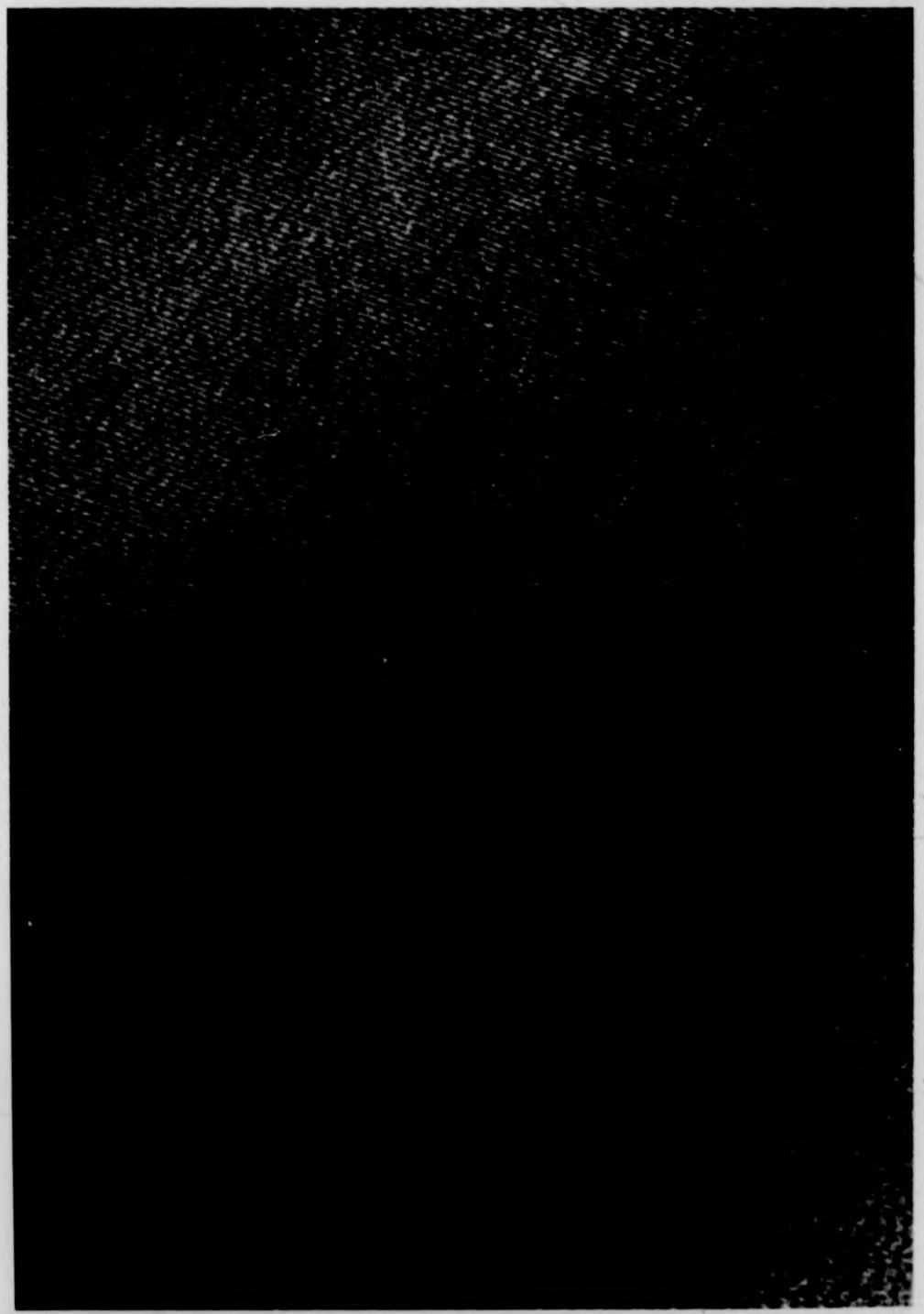

Fig. 3.9: Single β′-crystal lattice-fringe image (Prism-plane spacing 6.6 Å).

Fig. 3.10: Lattice-fringe image of two adjacent grains of Si-Al-O-N B showing β′-β′ interface structure (Lattice spacing 6.6 Å). Lighter region, marked G is triple-junction glass.


G

Fig. 3.11: Lattice-fringe image of two adjacent grains of Si-Al-O-N C showing β′-β′ interface structure (lattice spacing 6.6 Å)

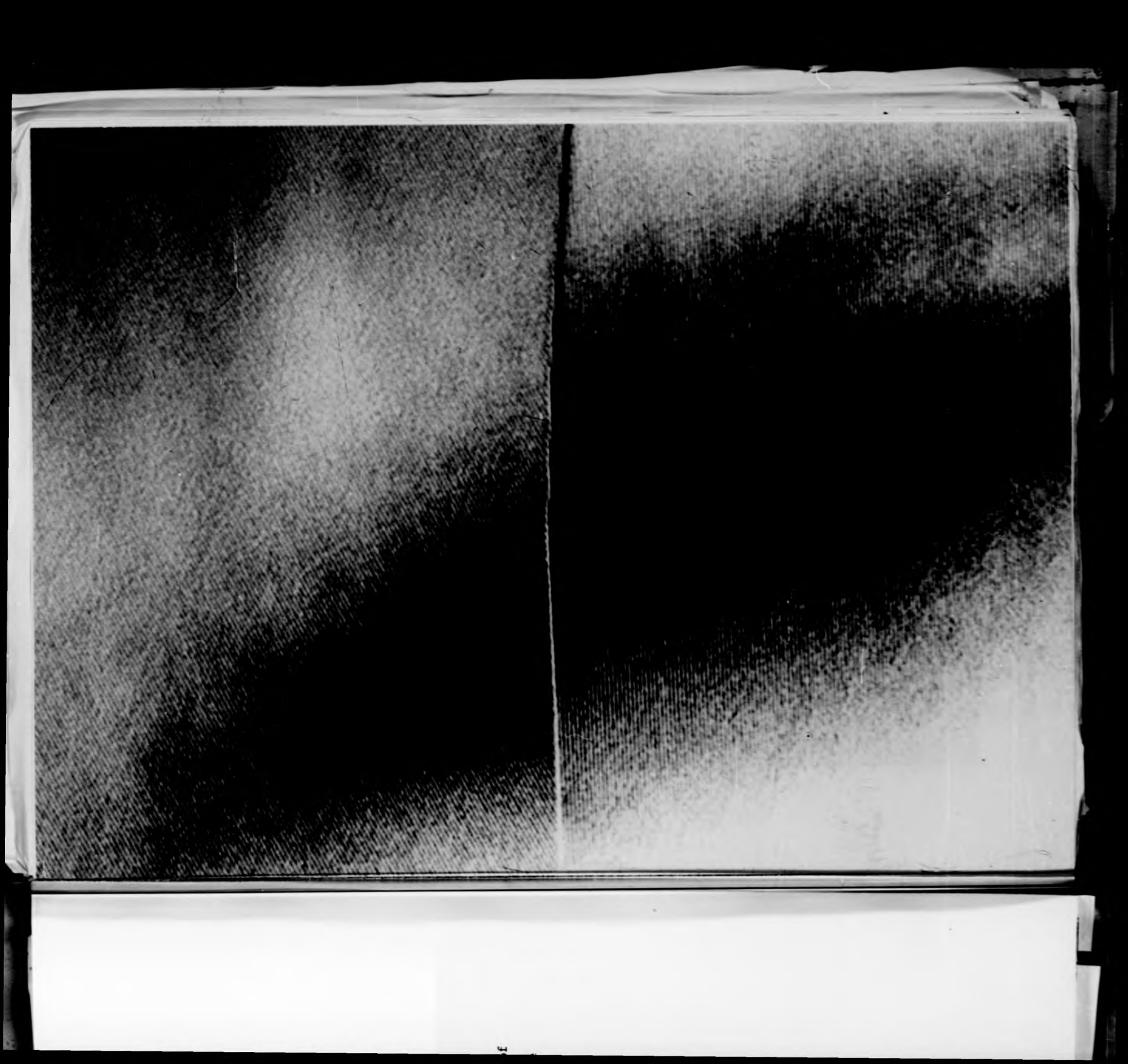

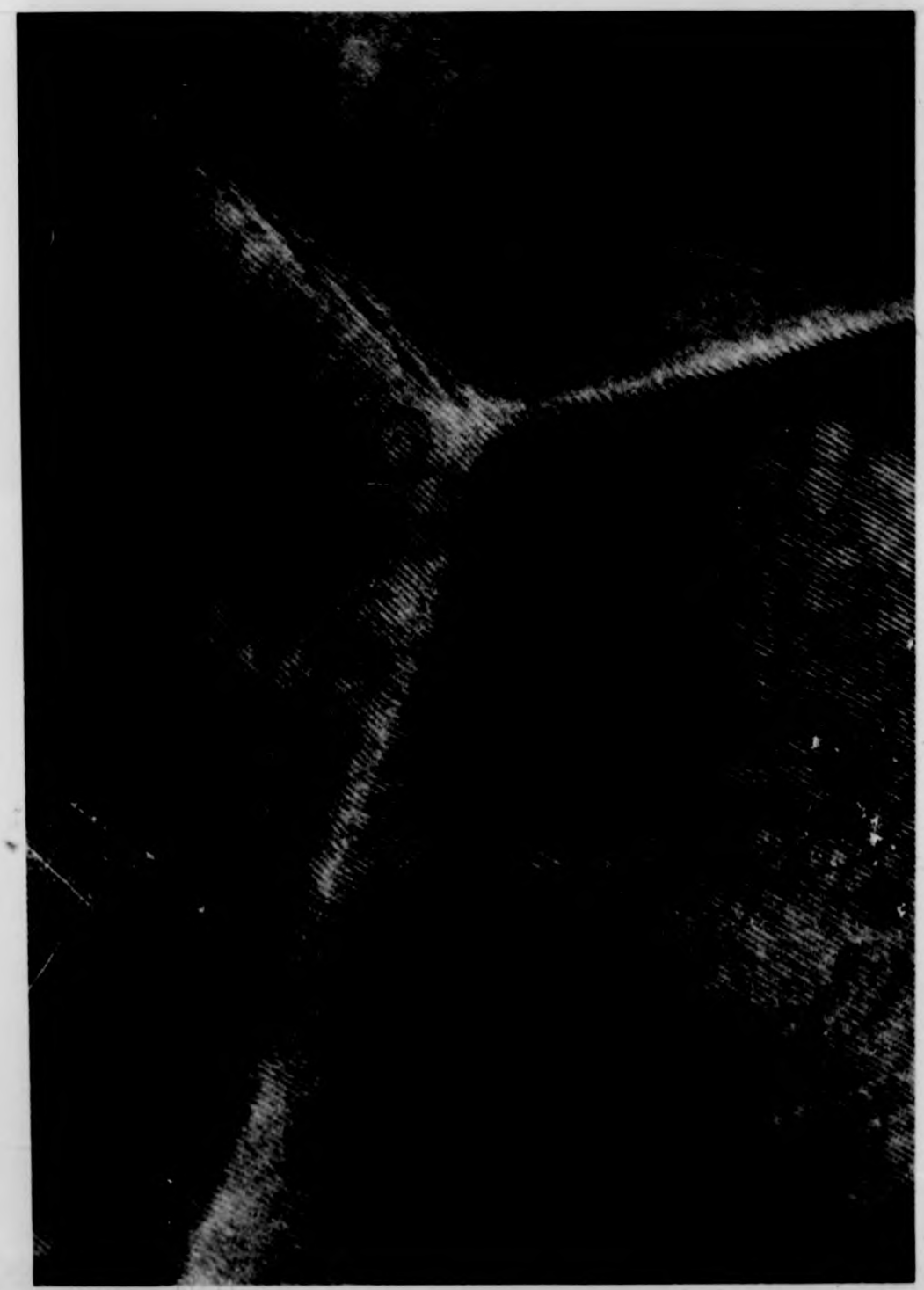

Fig. 3.12: Lattice-fringe image of a three-grain junction in Si-Al-O-N C.

of electron-beam, grain boundary and prism planes in adjacent β′ crystals. However, the boundaries which have been observed in lattice imaging are the most common boundaries of these materials (for example curved boundaries of specimen C) found in the general microstructure. The other important requirement is the correct orientation of the boundary with respect to the electron beam. If the boundary plane is slightly disoriented with respect to the electron beam it will lead to a wrong estimate of the boundary 'width'. In Mn-containing ceramics the faceted grain boundaries provide an ideal situation for observing the grain boundary exactly parallel to the electron beam. In ceramic C only a small region of this boundary can be observed exactly parallel to the electron beam because of the curved nature of the interface. However this small region shows the correct boundary width.

High resolution lattice imaging provides little or no information about the chemical structure of the grain boundaries. Impurities often segregate to grain boundaries even in single phase ceramics with no glassy film. Impurity segregation to the grain boundaries plays an important role in relation to the boundary diffusion, intercrystalline cohesion and other boundary properties which could influence the creep and fracture properties of ceramics. Therefore to study the impurity segregation Auger electron spectroscopy was performed.

3.2.2. Auger Electron Spectroscopy

3.2.2. (a) The Technique

Auger electron spectroscopy (AES) is a powerful technique for studying composition of the first few atomic layers (1-5 atomic layers) of the surface of a sample. In AES, an electron beam of energy 1 - 5 keV is incident on the surface and the energies of the ejected electrons (Auger electrons) are analysed. The sensitivity of AES is generally improved by differentiating the secondary electron energy distribution [150]. Details of the "Auger" process can be found in many publications [151,152] and only a brief description is presented here.

The primary electron beam strikes the specimen and causes the ionisation of an inner electron level of the atoms. These excited atoms can relax by releasing energy which can either be used in ejecting an electron or emitting a photon. However at low primary energies used in AES, the probability of photon production is very low. The ejected electron is known as an "Auger" electron which has a well defined energy specific to the element from which it escaped. Therefore the Auger process provides a method for compositional analysis. Furthermore, the Auger process involves low energy electrons and only those emitted from atoms close to the surface can escape and contribute to the Auger spectrum. Hence the analysis is surface-specific.

AES has been used by a number of workers to analyse grain boundary segregation in polycrystalline ceramics [16,31,153,154]. The technique is based on the chemical analysis of exposed grain boundaries (intergranular fracture areas) on the fracture surface. Using 'inert-gas' ion sputtering together with Auger analysis it is also possible to determine the concentration of impurities as a function of distance from the grain boundary [31,154].

3.2.2. (b) Observations and Discussion

In order to analyse grain boundary segregation, the grain boundaries must be exposed by fracture and this is normally done inside the vacuum chamber of the spectrometer to minimise the surface contamination. However these room temperature fracture surfaces normally contain a large proportion of transgranular fracture. It was observed by scanning electron microscopy (SEM) that fracture of the present sialon ceramics is mainly intergranular at temperatures above 1300°C. Therefore it was decided to use high temperature ($\sim$ 1400°C) fracture surfaces for the Auger analysis. The fracture tests were carried out in a vacuum furnace to minimise oxidation of the fracture surfaces (see Chapter 4).

The AES was performed in an experimental system constructed in the Physics Department at Warwick, which consists of a thermionic emission electron gun (probe diameter about 50 μm) and a cylindrical mirror analyser for the energy analysis. The specimens (fracture area 3 mm x 5 mm) were mounted on a rotating holder and placed in the vacuum chamber of the Auger system. The evacuated chamber was then 'baked' at 250°C for 24 hours to remove the residual surface-reactive gases. When a high vacuum ($\sim 10^{-10}$ torr) was established the fracture surface was positioned normal to the axis of the analyser and the primary electron beam was incident nearly normal to the surface. The Auger spectrum from 'as-loaded' fracture surfaces showed a large carbon peak and an oxygen peak. This carbon contamination is due to exposure of the fracture surface to the atmosphere. To remove carbon contamination the specimen was rotated towards the argon ion gun and bombarded with 5 keV argon ions with ion current density of about 5 μAcn^{-2} in a pressure of argon at $\sim 10^{-5}$ torr. This sputtering was carried out in a controlled manner. After a few minutes of sputtering the carbon peak was rapidly reduced and several other peaks appeared in the spectrum. The chemical

profile normal to the fracture surface was determined using the sputtering technique and AES analysis alternately. The sputtering times were increased gradually from 2 to 15 minutes. The removal rate of atoms from the fracture surface due to argon-ion sputtering was calculated from the argon-ion current density, assuming that the sputtering was uniform and there is no preferential removal of one element. (The sputter yield value for this calculation was obtained from [155]). This calculated sputtering rate ($\sim$ 4.5 Å per minute) may be subject to considerable error. After repeated bombarding of the fracture surface with argon ions, surface charging occurred which disturbed the Auger emission. In order to prevent this, moderate primary energies (1.5 keV) were used. Charging results from the poor electrical conductivity of the specimen. When working with insulators it is important to use primary energies which produce a secondary yield (defined as the number of secondary electrons created per incident primary) greater than one. Then the only effect of charging is a relative shift of the entire spectrum by a few eV [156]. For many insulators this primary energy region lies between 100 - 2000 eV [157].

Fig. 3.13 is a set of Auger spectra taken from ceramic B. Each spectrum shows the different element concentrations at various depths from the intergranular surface. The figures against each spectrum are the estimated thicknesses of material removed by sputtering. After identifying carbon and oxygen peaks the other peaks (Al, Si, N, Ca and Mn) were identified by calculating their relative position with respect to oxygen using the standard Auger energies [158]. However the observed position of the Si peak ($\sim$ 85 eV) is slightly shifted away from its standard position for pure Si (92 eV). A similar shift in the Si peak has been observed in Auger spectra from fracture surfaces of Si_3N_4 [151] and Sialon ceramics [31]. It has also been observed [151] in

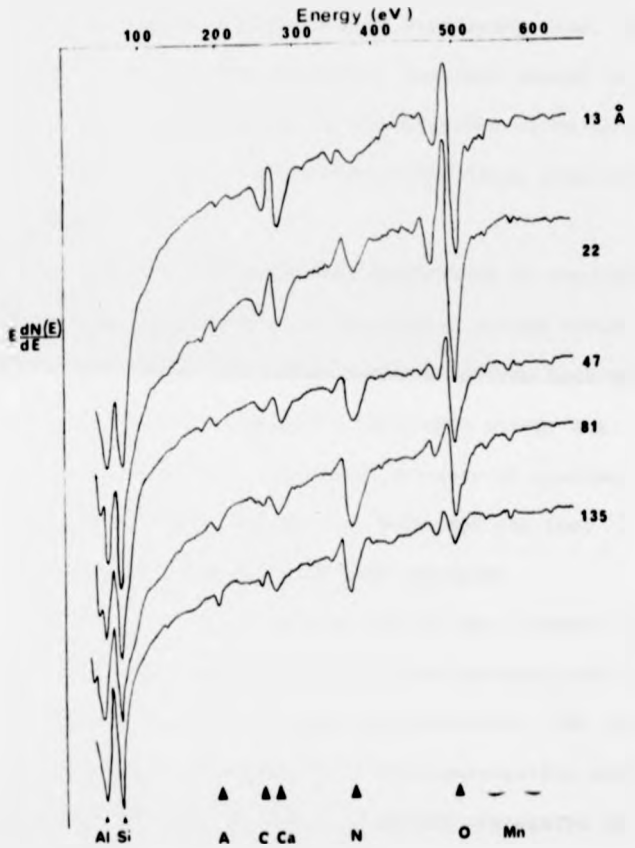

Fig. 3.13: Set of Auger electron spectra showing the increase or decrease in different element concentrations with distance from an intergranular fracture surface of Si-Al-O-N B.

The figures against each spectrum are the estimated thicknesses of material removed by sputtering.

Si_3N_4 that the position of the Si peak from a bulk specimen and from a fracture surface was not identical and it was pointed out that this is due to the change in chemical environment of the silicon atoms. The Mn peaks show only a small variation with sputtering time. This indicates that the Mn concentration is nearly constant normal to the fracture surface which is probably due to the presence of Mn-containing particles in the material (the particle size being large compared to the thin boundary film).

The small argon peak is due to surface adsorption or implantation of argon ions during the sputtering. In the higher energy scale closer to 1200 eV a very small peak (just resolvable from back-ground noise) was observed and this is possibly a Mg higher energy Auger peak. The higher energy analysis was not successful because of specimen charging due to a higher primary energy (> 3 keV) and the poor performance of this Auger spectrometer at high energies.

The chemical profiles of the concentration of the elements (Fig. 3.14) normal to the fracture surface were obtained assuming that the peak height is proportional to the element concentration. The nitrogen peak is used as a reference. The rapid fall in concentration within a few atomic layers indicates that Ca and O is mainly segregated at the grain boundaries. The growth of the nitrogen peak with sputtering is also partly responsible for this rapid drop in concentration.

The low energy (0 - 600 eV) AES on ceramic C showed similar impurity segregation (except Mn) to that of ceramic A. The higher energy range of AES did not function successfully due to specimen charging and the low signal level. However it has previously been shown [31] in a similar single-phase material (1% MgO) that Mg is mainly segregated at grain boundaries (Fig. 3.15). For comparison with the Mn containing ceramic, O/N and Ca/N profiles from reference 31 are also included in fig. 3.15.

Fig. 3.14: Variation in concentration of impurity elements indicated by variation in Auger peak height with distance from the intergranular surface of Si-Al-O-N B.

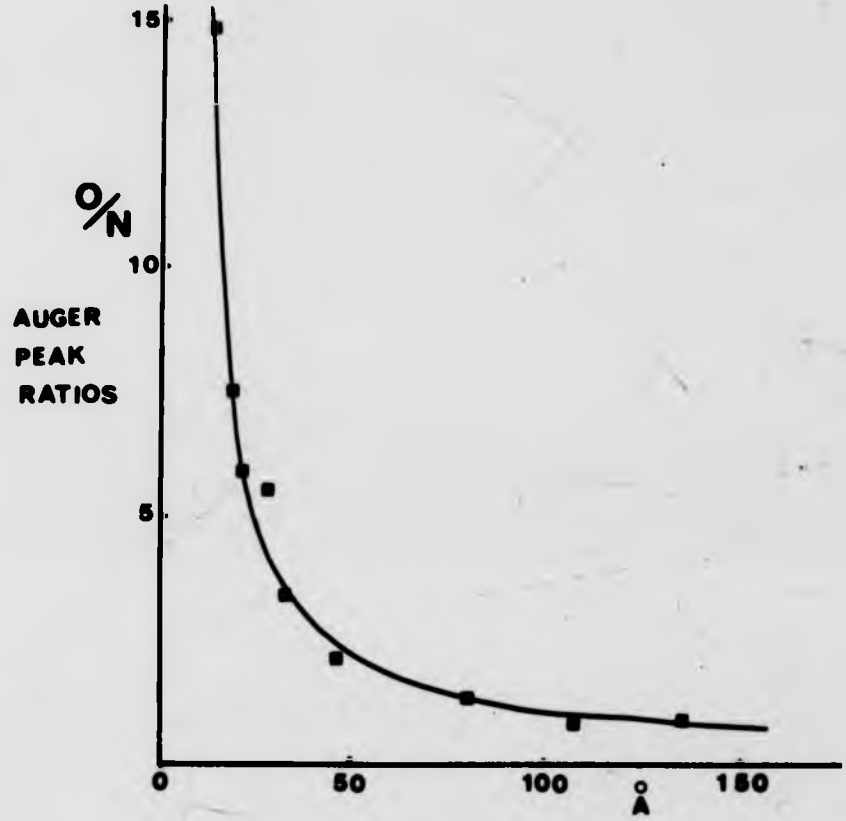
O/N
AUGER
PEAK
RATIOS
15
10
5
0
50
100
150
Å

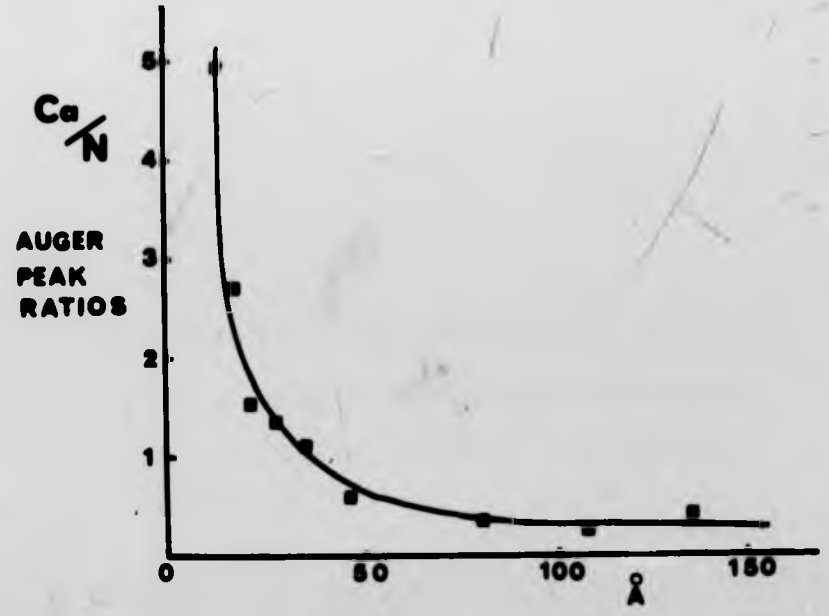
Ca/N
AUGER
PEAK
RATIOS
5
4
3
2
1
0
50
100
150
Å

Fig.3·14

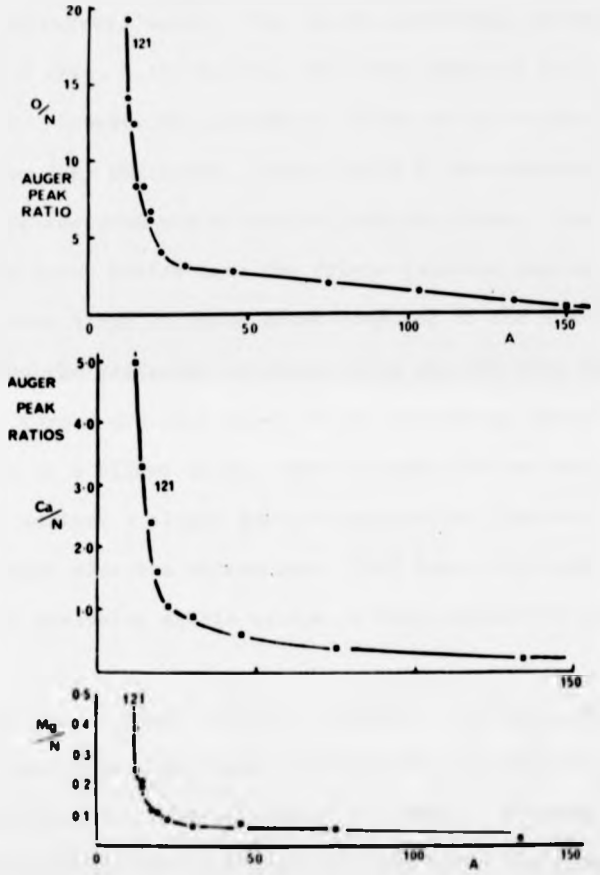

Fig. 3.15: Variation in concentration of additive and impurity elements with distance from the intergranular surface of Si-Al-O-N 121 [31]

If allowance is made for the initial contamination layer the approximate thickness of the boundary phase can be estimated from the AES profiles. (It was assumed that the fracture surface contains only half of the segregated layer). For the Mn containing ceramic this thickness is $\sim$ 20 Å (Fig. 3.14) and for the other material it is $\sim$ 15 Å (Fig. 3.15). However the estimated values may be slightly higher than the boundary thickness, particularly in Mn-containing material because of the presence of triple junction glass. The thickness of this segregated layer varies near the triple junction regions and the thickness is very large in these areas compared to the boundary regions. Therefore the estimated thickness from the AES data obtained from a large area (probe diameter about 50 μm) containing thousands of grains will result in a higher value. This problem can be avoided if it is possible to analyse a single grain intergranular fracture surface. Modern Scanning Auger electron microscopes [159] have this high resolution and are capable of analysing single grains of fine grained ($\sim$ 1 μ) materials.

More recently the fracture sample of ceramic C has been analysed using a JAMP 10 high resolution (probe diameter 0.6 μm) Auger scanning electron microscope (at the JEOL Laboratory in Tokyo). Although the chemical profiling has not been performed in this study the compositional analysis shows very good agreement with the earlier observations.

3.2.3. Summary of Microstructural Analysis

In Mn containing ceramics (A and B) most of the residual glass is localised at triple junctions. It is difficult to conclude whether this glassy phase is also present as a continuous thin film between the grains because the observed width of this boundary region is same as the interplanar spacing used in lattice imaging. Apart from triple junctions, there is no resolvable difference between β′ grain

boundaries in the two ceramics, down to an approximate limit set by the prism-plane spacing in adjacent β′ crystals. The estimated thickness (15 - 20 Å of the boundary segregate of these materials from AES data is larger than the value obtained by lattice imaging (∿ 7 Å). This may be mainly due to the inaccuracy in thickness determination in AES technique and also the uncertainty in defining the boundary width in the AES profiles. Although a precise compositional analysis could not be carried out on the fracture surfaces AES data show that the grain boundaries contain the hot-pressing additives (Mn and Mg), Oxygen and impurity Ca. Previous work on Si_3N_4 [151] shows that the grain boundary phase is a glass containing Si, Mg and Ca oxides. The exact composition of the boundary phase has been estimated by comparison with the Auger spectrum from a glass standard. Using a similar comparison the compositon of the grain boundary segregate in the Mg-containing Sialon ceramic, has been [31] estimated as 0.076 CaO 0.42 MgO 0.22 Al_2O_3 2 SiO_2.

In Si_3N_4 the shift in the low energy Si peak position has been used [151] to distinguish Si in the grain boundary silicate glass and that in β-Si_3N_4 crystals. However in sialons there is no visible shift in Si peak with progress of surface sputtering. This indicates either that the position of the Si peak from β′ crystals is the same as its position from a silicate glass or the observed Si peak is mainly from β′ crystals.

Finally, the AES data suggest the composition of the triple junction glass observed in the Mn-containing material is a silicate of Ca, Mn, Al and Mg which is possibly the cooled residue of the liquid sintering medium. It is believed that the essential difference between the two ceramics lies in the partitioning of Mg and Mn between the silicate phase and β′ crystals. Hence, a smaller solubility of Mn in β′ stablises the silicate phase in triple junctions after grain impingement and remains

as a residual glassy phase on cooling. It is likely that Mg has some solid solubility in β′ crystals and this results in simultaneous solid solution of oxygen in β′ crystals for charge neutrality. This removal of oxygen reduces the residual glass in ceramic C. The observation of triple-junction glass in both Mn-containing ceramics (A and B - prepared separately) supports the above suggestion and does not favour the possibility of an accidental difference in O/N balance from the β′ requirement ($Si_{6-x}O_xAl_xN_{8-x}$).

CHAPTER FOUR

EXPERIMENTAL TECHNIQUES

In the first part of this chapter the design, construction and operation of a high-temperature creep apparatus, which could easily be adapted to perform bend and uniaxial compression creep is described.

The second part contains a description of the construction of a high temperature double torsion jig and analytical procedures used in determining the K_1-V relationship.

4.1. Creep Testing

Most creep experiments on ceramic materials are performed in bending to avoid the problems of gripping and buckling associated with tensile and compression tests. Although the bending experiments are relatively easy to carry out there are several problems concerning interpretation of experimental data. One major criticism about the bend test is it s inhomogeneous stress distribution. The creep strain and stress relations are normally derived under elastic condition for small strains and hence the relations are true only if (see Appendix A4.1) (a) the strain rate is directly proportional to the stress (stress exponent n = 1), (b) the creep properties in tension and compression are identical and (c) the total plastic strain is small, normally less than about 2%.

As the strain increases additional problems arise due to non-vertical forces at load and support points and this may reduce the applied stress. However in this programme many creep tests were performed in four-point bending and later some tests were repeated in compression as confirmation experiments.

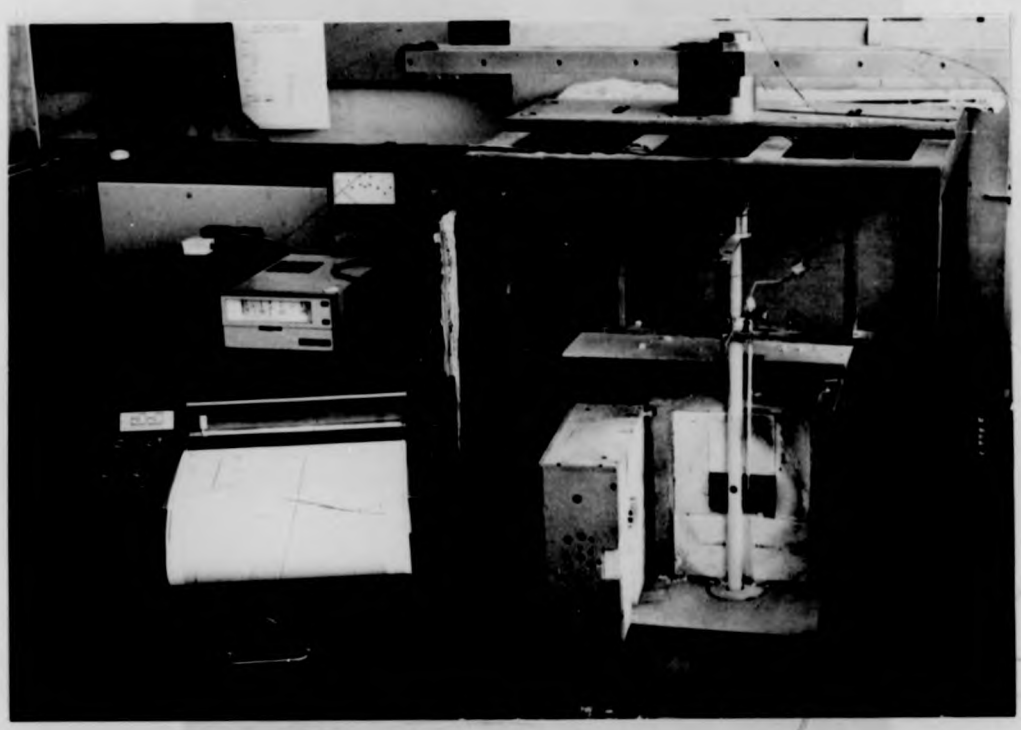

Fig. 4.1: The creep rig and furnace.

Fig. 4.2: Four-point bend creep jig.

substantial length (within inner loading points) of the specimen. Even for large deflections of 20° to the horizontal at the outer loading points, the variation is about 2.8% [160].

The four-point creep jig (Fig. 4.2) was machined from recrystallised alumina and it consists of three basic components; an upper loading hemispherical head (A), a tube (B) as the outer loading points and a concentric inner tube (C) to guide the loading head to give a symmetrical four-point loading on the specimen. The hemispherical head (A) permits equal vertical loading of the specimen via two knife edges. (Fig. 4.3) To ensure stability, this alumina piece was made sufficiently long so that it s centre of gravity lies below the specimen. Preliminary creep tests confirmed that there was no detectable deformation of the knife edges (The loads used for the bend tests were very small) or reaction between ceramic specimens and alumina jig during creep tests.

The specimen span was 40 mm and inner knife edge span 20 mm. This span ratio ($\frac{L}{a} \sim 2$), falls in the limit of n (stress exponent) insensitivity to strain equation [161] and gives rise to measurable deflection rates over a wide range of stress. (See Appendix A4.1). The load was applied to the specimen by means of a lever system (2:1 ratio) which was counter-balanced by a dead weight. The load point displacement was monitored with a linear differential transformer (LVDT, type 500 DC supplied by Electromechanisms Ltd) and recorded on a potentiometric chart recorder, (CR 650 S supplied by J. J. Instruments Ltd.). The LVDT body was initially mounted rigidly on the metal frame and the core was placed on the lever arm. The outer fibre strain and stress were calculated using the following equations [161] assuming elastic conditions and n = 1 (See Appendix A4.1)

$$\sigma_{max} = \frac{P\ (L-a)}{2bh^2}\ \frac{(2n+1)}{n} \qquad (4.1)$$

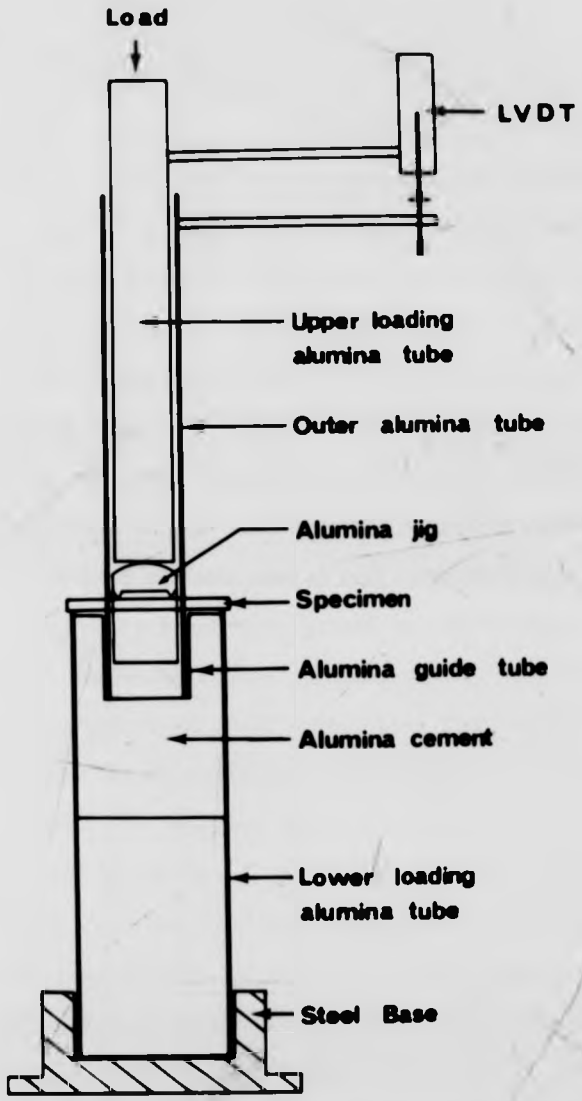

Fig. 4·3 Four-pt. bend creep measuring arrangement

$$\varepsilon_{max} = \frac{2h\ (n+1)}{(L-a)\left[L+a(n+1)\right]} \cdot Y_L \qquad (4.2)$$

where P, h, b, L, a and Y_L are the load on the specimen, specimen height, width, outer span, inner span and load point deflection respectively.

The creep strain was initially monitored satisfactorily with this measuring arrangement at constant ambient temperature. However the room temperature fluctuations, especially day and night variations, gave rise to extraneous variations in creep curves. This was due to transducer movement caused by the thermal expansion or contraction of the metal frame and other components of the test rig. To obtain constant ambient temperature conditions, the rig was surrounded by thick insulating "Asbestos" fibre boards. Although this helped to remove thermally-induced variations in the creep curves at higher creep rates the thermal expansion caused disturbances at lower creep rates (10^{-7} h^{-1}). This arrangement was clearly not suitable for compressive creep rates which are normally very small. To overcome these extraneous problems most investigators have used two or more transducers. However, if the transducers are not identical in output voltage per unit displacement this arrangement may give rise to inaccurate creep rates. In practice even the same type of transducers have slightly different output voltages per unit displacement. Hence the thermal expansion could produce a few millivolts differential output (instead of zero output) which can be a significant fraction of the total output due to creep deformation, particularly in compression.

After careful consideration of these problems involving strain measurement, a different LVDT mounting was designed. (Fig. 4.3). In this new arrangement the LVDT body was rigidly clamped by an Al rod to the loading alumina rod and the LVDT core was placed on a small Al platform

rigidly joined to the outer alumina tube which also guides the loading rod. The platform was adjusted to the required position with a micrometer screw gauge. The important feature of this system is that the LVDT mounting is now free from the metal frame and the major part of the measuring system is at a constant furnace temperature. However if there is any thermal variation, expansion of the components would occur in the same direction and hence minimize the resultant displacement of the LVDT body and its core. Therefore in this measuring system the LVDT gives the correct creep deformation without any extraneous effect due to thermal variations.

To stop heat flow towards the LVDT, the top of the furnace was covered with 'Safil' wool (I.C.I. product) and this helped to keep the temperature around the LVDT to a lower level ($\sim 60^{o}C$). However, the LVDT was calibrated under this ambient temperature condition and this value (410 mV per mm) rather than the manufacture's value (500 mV per mm) was used to calculate creep strain.

The performance of this system was extremely succesful and therefore a similar measuring arrangement was used in designing the compression jig.

4.1.1. (c) Compression Creep

One of the major problems in compressive creep is specimen buckling. In general, buckling is more likely to occur in specimens having a large ratio of length ℓ, to width ω. Very low ℓ/ω ratios can result in 'barrelling' of the specimen, because of specimen end constraint [95]. However these two effects can be avoided using a ℓ/ω ratio in the range 1.5 to 2.5 [81]. The other important factor is correct alignment because non-axiality of loading can also cause buckling and introduces multiaxial stresses. These requirements together with the ability to measure small strains and to eliminate extraneous effects were achieved by

using a simple arrangement as shown in Fig. 4.4. The LVDT arrangement of this jig was similar to that described earlier for four-point bending. "Refel" SiC (U.K.A.E.A. Springfield) loading rods were used within the furnace instead of alumina rods to minimize any possible deformation of the loading rods due to high compressive loads at the furnace temperature. The SiC rods were not extended to the outside of the furnace to reduce the thermal conduction loss along SiC rods. The other disadvantage of using "Refel" SiC rods is oxidation and melting of free silicon at high temperatures. These oxide and free silicon products on the surface of the rod could disturb the smooth movements inside the outer alumina tube. To overcome this the SiC rods were enclosed in alumina tubes as shown in Fig. 4.4.

The specimens, 3 mm x 3 mm x 5 mm ($\frac{\ell}{\omega} \approx 1.7$) were introduced into the jig through the windows, drilled on either side of the alumina tube, (Fig. 4.5) and placed exactly on the centre of the circular silicon carbide platens using a plastic jig, to obtain exact axial loading. The long outer alumina tube guides the inner loading rods axially up to the specimen ends from both sides and hence provides an accurate self alignment. The whole arrangement was kept rigidly in the vertical position in a metal base and the load was applied to the upper alumina rod by means of a lever system having a 10:1 ratio. The desired load was applied by lowering appropriate slotted weights onto the load plate in the lever. A preliminary test was carried out without a specimen at 1375^{o}C with a 25 kg weight on the load plate (i.e. 250 kg weight on loading rods) for nearly 50 hours to ensure thermal stability and negligible deformation of the loading rods. This was confirmed by observing zero creep rate on the chart recorder.

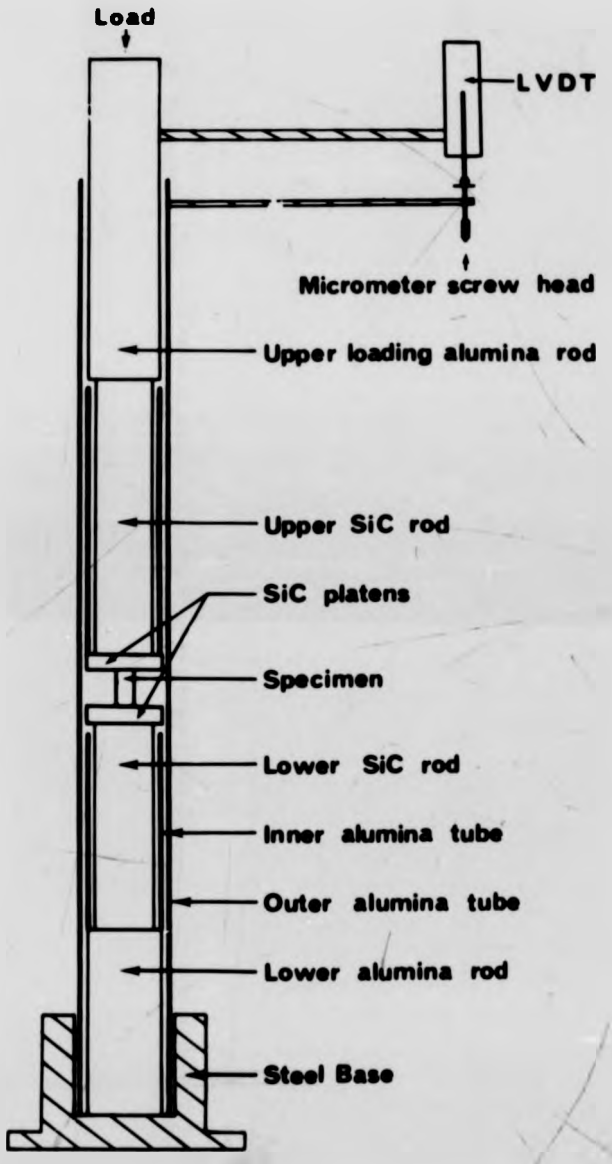

Fig.4·4 Compressive creep measuring arrangement

Fig. 4.5: Compressive creep jig.

4.1.1. (d) Specimen Preparation

3 mm slabs were cut parallel to the hot-pressing direction from each tile on a surface grinder fitted with a diamond slitting wheel. 3 mm x 3 mm x 50 mm or 3 mm x 3 mm x 5 mm specimens were cut with a thin annular saw for bend and compressive creep tests respectively. Special care was taken to cut the width normal to the length in compressive creep specimens. This was done by mounting a long 3 mm x 3 mm bar parallel to the edge of the mounting block, which was perpendicular to the cutting wheel. Rectangular specimens were cut rather than 'dumb-bell' shaped specimens for compression creep to avoid complex machining. It has been shown [95] that both type of specimens have the same steady state creep rates. The specimens were polished using SiC papers (600 grit) in order to maintain the same surface condition for all specimens.

4.1.2. The Testing Procedure

The furnace was heated to the required temperature (1100°C - 1450°C) without load on the specimen and left overnight before the test. This allowed ample time for thermal stabilization. To avoid experimental scatter between specimens and also to save a great deal of time an incremental stress technique was used to obtain a value for n. In this method creep rates were measured on a single specimen at different increasing stress levels under isothermal conditions. Similarly, creep rates were measured on lowering stress levels from higher values. The stress exponent n was determined by plotting logarithmic strain rate *vs* logarithmic stress.

The grain size dependence on creep rate could not be investigated due to lack of different grain size materials.

Temperature-change tests were carried out under constant load conditions to determine the activation energy for the creep process. Again the creep rates were measured on a single specimen at different temperatures keeping the stress constant to avoid structural differences between individual specimens. In bend specimens the temperature was raised from 1100°C to 1450°C, but in compressive tests a maximum temperature was restricted to 1375°C (strength degradation occurs in "Refel" SiC at ∿ 1400°C due to the melting of free silicon). In both stress-change and temperature-change experiments, care was taken to allow sufficient time for transient effects accompanying the parameter changes, and to re-establish the steady state conditions. Typically these changes were made with a periodicity of ∿ 24 hours in the increasing sense and ∿ 36 hours in the decreasing sense and 24-48 hours was allowed for initial primary creep. At high stresses and temperatures the periodicity was reduced to ∿ 10 hours.

True stress and true strain were not calculated in compression test because the variation in cross-sectional area and the length of the specimens were very small during the creep deformation of these ceramics. In bend tests, if the material did not fail before nearly 2% total strain, normally tests were terminated. At the end of the tests, the total creep strain was calculated directly from the pure bend section of the specimen and compared with that from chart recorder reading. A similar comparison was made with compression specimens. There was a good agreement between the two values within experimental limits. No detectable impression was observed on the SiC platens even after many successive creep tests. The stress variation and temperature variation tests were repeated to check the reproducibility of creep data.

4.2. FRACTURE TESTING

4.2.1. K_1-V Relation

Stress intensity factors (K_1) and crack velocities (V) were obtained on double torsion (D.T) specimens at elevated temperatures (1100°C - 1500°C) using an Instron machine equipped with a vacuum furnace. These tests were performed in vacuum (10^{-5} torr) to preserve the fracture surfaces from oxidation and enable subsequent examination in an SEM.

4.2.1. (a) Vacuum Furnace

The vacuum furnace consists of a SiC spiral shaped heating element (CRUSILITE element type RM, hot zone 150 mm), a recrystallised alumina tube with water cooled ends inside the heating element and a larger alumina tube outside the element as shown in Fig. 4.6. The inner tube is connected to a vacuum system containing a rotary pump and an oil diffusion pump. The water cooled stainless steel upper loading rod is extended to the hot zone with a threaded recrystallised alumina rod (diameter ∿ 20 mm) and the lower loading alumina tube is placed in the collet of the lower loading rod.

The furnace was mounted in such a way that it could be moved smoothly up and down along the metal rods and weights were used together with a pulley system to counter-balance the weight of the furnace. Temperature was controlled (± 2°C) in a similar way to that described for the creep furnace using a stepless Eurotherm controller with Pt/Pt 13% Rh thermocouple. The controller-thermocouple was placed in between the inner alumina tube and the heating element. The controller temperature was calibrated accurately using another thermocouple inside the inner alumina tube closer to the specimen position and later these calibrated values were used to determine the specimen temperature in each test.

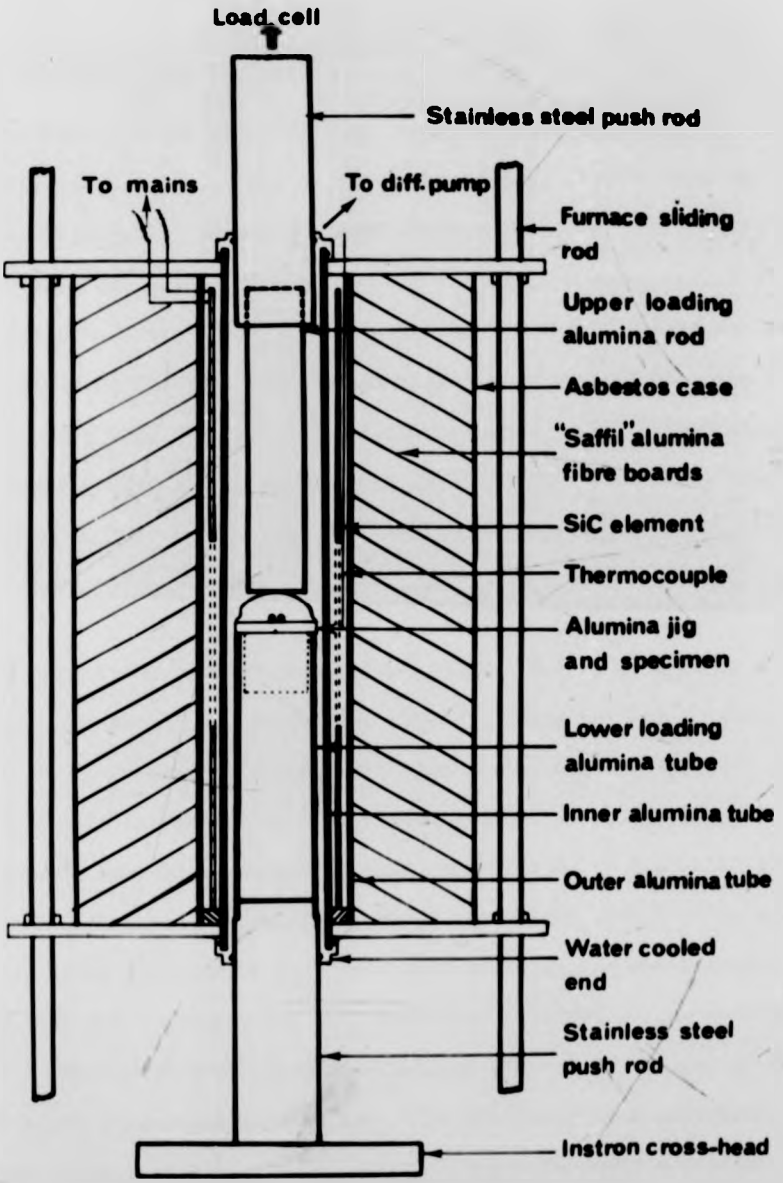

Fig. 4·6 Vacuum Furnace

4.2.1. (b) Double Torsion Jig

The D.T. jig was machined from recrystallised alumina (Fig. 4.7). Basically, this jig consists of three components; alumina tube (A) with two rectangular holes, U-shaped alumina piece (B), sitting in the tube between the rectangular holes, and the upper loading head (C) which could be moved smoothly inside the tube. The D.T. specimen was placed horizontally on B and a small plastic jig used to position the upper loading head symmetrically on the specimen. The hemispherical upper loading head (C) is designed to transmit the load evenly down to the one end of the specimen via. two knife edges (Fig. 4.7).

4.2.1. (c) Double Torsion Specimen and Constant K_1 Calibration

The specimens were cut from larger slabs into 20 mm x 15 mm x 2 mm or 20 mm x 15 mm x 3 mm rectangular plates. These specimens were mounted on a uniformally thick steel base plate, exactly parallel to it s base with thermoplastic 'Lake-side' cement. This was gripped on the magnetic base of a surface grinder, and grooved to approximately one half of the specimen thickness along the length with a slitting wheel of blade thickness 1 mm. This reduced thickness was introduced to ensure crack propagation in a direction parallel to the specimen length. Specimens were notched to a depth of 5 mm at one end of the groove using an annular diamond saw. The specimens were polished using SiC paper (600 grit) in order to maintain the same surface condition for all specimens.

Kies and Clark [138] have indicated in their analysis of the D.T. specimen that the stress intensity factor K_1 is independent of crack length. Later Williams and Evans [139] derived the following mathematical expression relating Load (P) and specimen dimensions to stress intensity factor. (See Appendix A4.2).

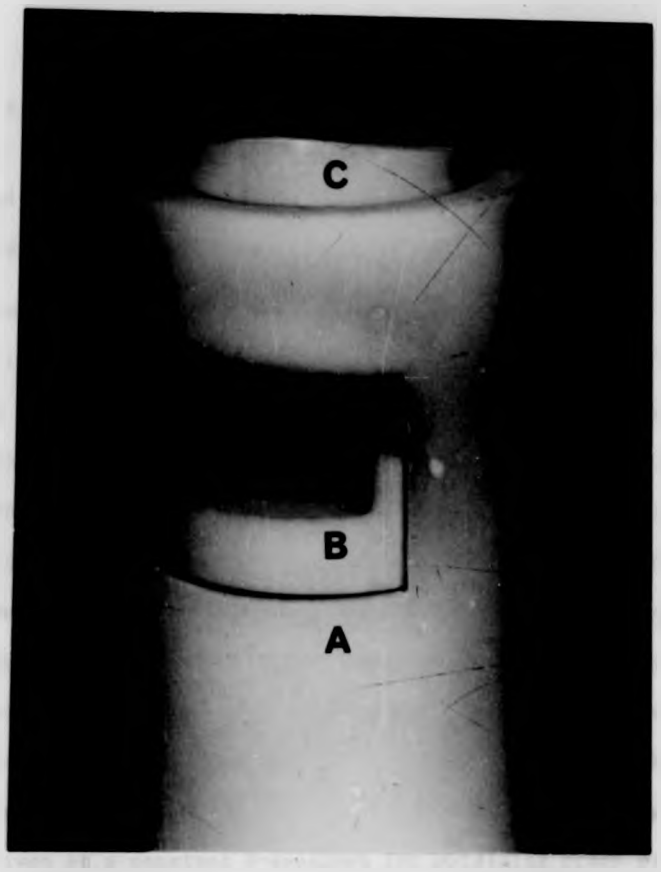

High-temperature D·T· test jig

Fig.4·7

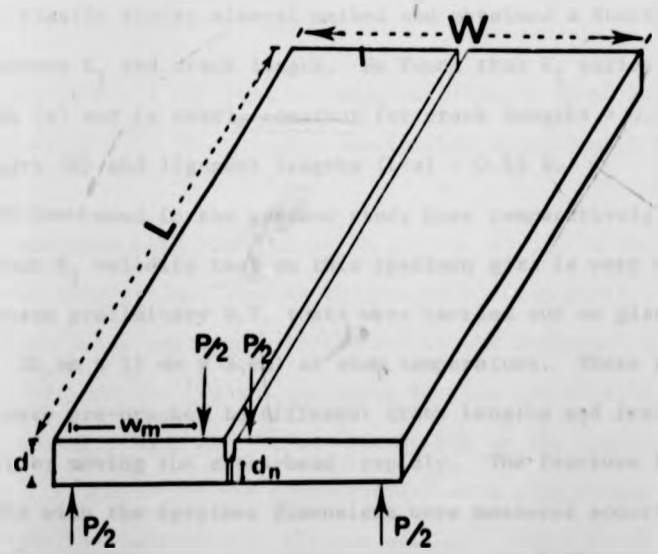

Fig.4·8

$$K_1 = P\ Wm \left[\frac{3(1+\nu)}{Wd^3 d_n}\right]^{\frac{1}{2}} = A.P \qquad (4.3)$$

where ν is Poisson's ratio, P is the applied load and other symbols are specimen dimensions (Fig. 4.8).

This relation shows that K_1 is independent of crack length. Here, they treated the D.T. specimen as two elastic torsion bars, each having a rectangular cross-section loaded at one end. This assumption neglects the possibility of either shear strains in the individual bars or flexture of the uncracked position of the specimen. This implies that the above relation is valid only for crack lengths close to the middle of the specimen. Williams and Evans [139] checked the validity of the relation by performing compliance tests on steel and found a very good fit of experimental data with calculated values for relatively large crack lengths and a slight departure for small crack lengths. However it can be seen in literature that many investigators have used the D.T. specimen as a constant K-specimen for obtaining crack propagation data in various materials.

Recently Trantina [162] analysed the D.T. specimen using a 3-dimensional elastic finite element method and obtained a functional relation between K_1 and crack length. He found that K_1 varies with crack length (a) and is nearly constant for crack lengths > 0.55 x specimen width (W) and ligament lengths (L-a) > 0.65 W.

The specimens used in the present study were comparatively small and a constant K_1 validity test on this specimen size is very important. For this reason preliminary D.T. tests were carried out on glass specimens (20 mm x 15 mm x 2 mm) at room temperature. These glass specimens were pre-cracked to different crack lengths and fractured in the D.T. jig by moving the cross-head rapidly. The fracture level (P_f) together with the specimen dimensions were measured accurately and substituted in equation 4.3 to calculate K_{1c} for different crack

lengths. The K_{1c}-crack length calibration obtained in this way is shown in Fig. 4.9. This shows that K_1 is constant only between crack length 5 mm to 15 mm for the specimens used in this study. This is the reason for introducing the 5 mm notch at one end of the groove.

4.2.2. The Test Methods and the Testing Procedure

There are a number of test techniques available to obtain crack propagation data. At low temperatures it is easy to follow a crack optically [123,127] to obtain the crack growth rate for a given load. At elevated temperatures the D.T. specimen can easily be used in the Instron testing machine for slow crack growth measurement under fixed grip conditions where the crack growth rate is determined directly by the rate of load relaxation.

4.2.2. (a) Load Relaxation Method

Williams and Evans [139] developed this method and derived the following expression for crack velocity (see Appendix 4.2).

$$V = - \frac{a_i P_i}{P^2} \left(\frac{dP}{dt}\right) \qquad (4.4)$$

The crack velocity can thus be obtained directly from the rate of load relaxation $\left(\frac{dP}{dt}\right)$ (Fig. 4.10), the initial crack length a_i and initial load P_i.

A D.T. specimen with known crack length was placed in the jig and introduced into the hot zone of the vacuum furnace until it was positioned just below the upper loading rod in the furnace. (A small gap was kept between the jig and the upper loading rod to allow for thermal expansion). When the furnace was heated to the required temperature, the cross-head was moved rapidly to a predetermined load P_i (just below the fracture load P_f) and stopped. The rate of load relaxation was measured from the Instron chart record. In this way a

Fig. 4.9: Constant K_1-calibration for D.T. specimens.

Fig. 4.10: Typical load-relaxation curve.

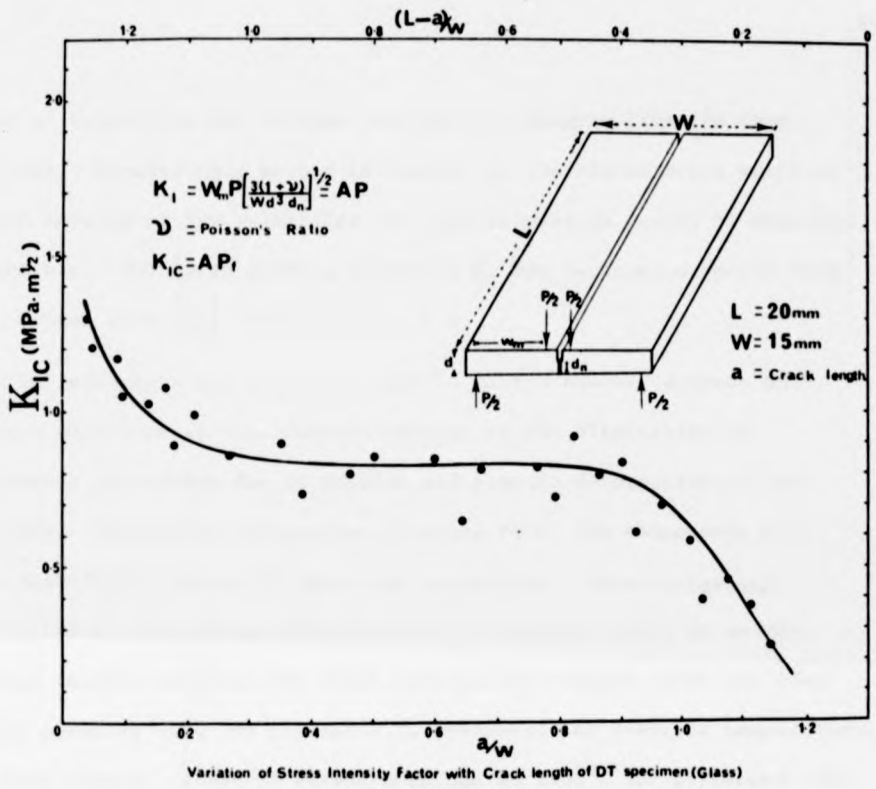

Variation of Stress Intensity Factor with Crack length of DT specimen (Glass)

Fig. 4·9

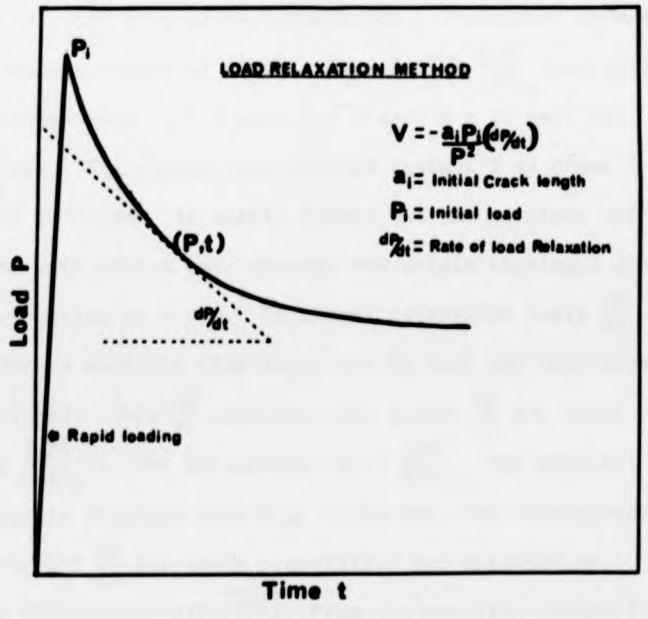

Fig.4·10

range of velocities was obtained on the K_I-V diagram from the same specimen. However this method is limited to the higher crack velocity region because at low velocities the load relaxation cannot be measured accurately. The corresponding values of K_I can be found directly from load P (for each $\left(\frac{dP}{dt}\right)$) via. equation 4.4.

The effective use of the relaxation method however depends on certain experimental requirements related to the elimination of extraneous relaxation due to machine and plastic deformation of the specimen. The machine relaxation (loading rods, jig components etc). is a significant factor of the total relaxation. This background relaxation was determined from auxiliary relaxation tests on an un-grooved thicker specimen (No crack propagation occured under the load levels normally used for thinner D.T. specimens) at previous temperatures and load levels. A set of curves obtained at 1400°C for different load levels is shown in Fig. 4.11b (Here in this background relaxation is denoted by $\left(\frac{dP}{dt}\right)_B$). Two factors, load P and time t, determine the rate of load relaxation $\left(\frac{dP}{dt}\right)$ at a given temperature. Therefore, from the background relaxation curves at 1400°C (Fig. 4.11b) $\left(\frac{dP}{dt}\right)_B$ was obtained after specific times (e.g. t = 0 sec. t = 6 sec. t = 12 sec) for different P values. The values were plotted against P as shown in Fig. 4.11a. The relation is nearly linear and the straight lines representing the data points pass through the origin showing a correct zero rate of relaxation at P = 0. In actual relaxation tests $\frac{dP}{dt}$ was measured after a specific time (e.g. t = 12 sec) and the corresponding P value was obtained. This $\frac{dP}{dt}$ contains both actual $\frac{dP}{dt}$ for crack propagation and $\left(\frac{dP}{dt}\right)_B$. The background value $\left(\frac{dP}{dt}\right)_B$ for specific time (e.g. t = 12 sec) is obtained from Fig. 4.11a via. the corresponding P value. The correct $\frac{dP}{dt}$ for crack propagation was obtained by subtracting the background value $\left(\frac{dP}{dt}\right)_B$ from the observed relaxation. This procedure is illustrated in Fig. 4.11c. This corrected $\frac{dP}{dt}$ value

Fig. 4.11: A method for elimination of machine relaxation.

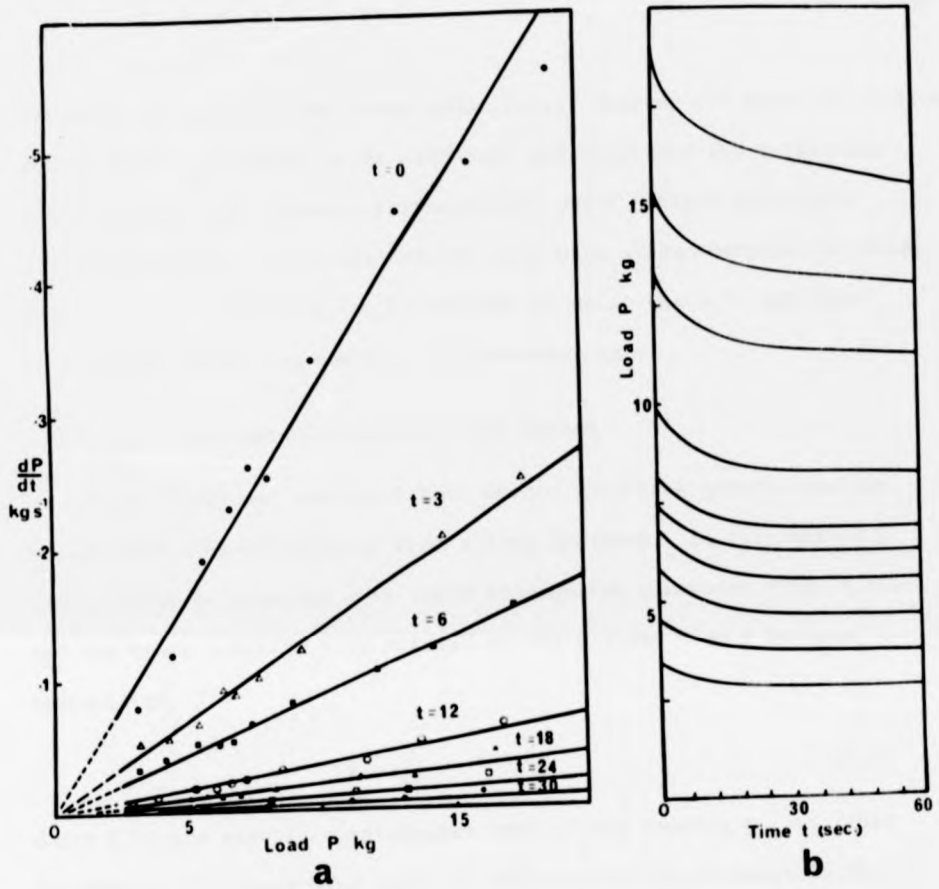
t = 0
t = 3
t = 6
t = 12
t = 18
t = 24
t = 30
dP/dt kg s⁻¹
Load P kg
Time t (sec.)
a
b

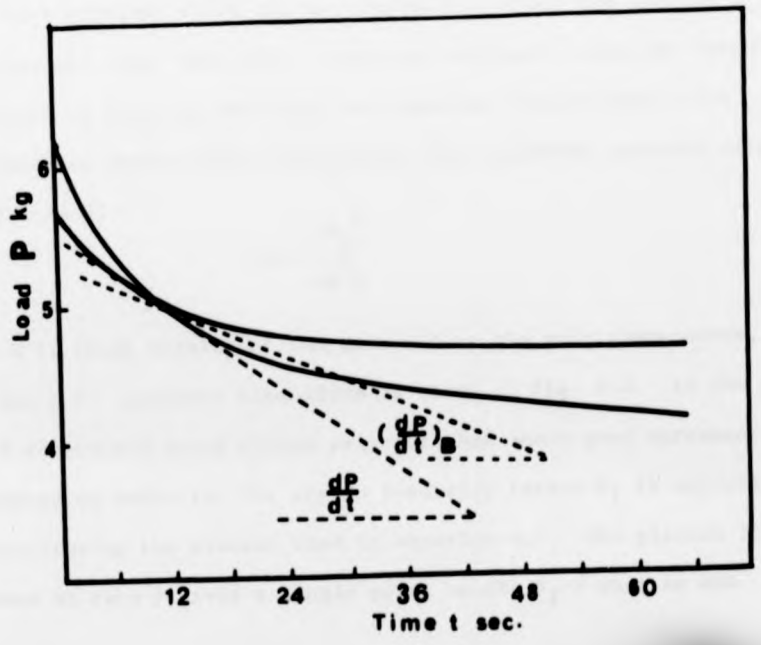
Load P kg
(dP/dt)₀
dP/dt
Time t sec.
c

Fig. 4·11

was used to calculate the crack velocities. However the exact correction due to plastic deformation is difficult and therefore the relaxation method is not very accurate for materials which exhibit relatively large plasticity. (This was not the case with sialon ceramics studied). However, this difficulty can be avoided by using the D.T. specimen in different modes, at constant displacement rate.

4.2.2. (b) Constant Displacement Rate Method

Evans [125] has developed this method and crack growth data can be obtained very efficiently from a long specimen. In this method a load plateau is observed when crack propagation commences (Fig. 4.12) and the crack velocity V is related to the plateau load P by (see Appendix A4.2)

$$V = \frac{\dot{y}}{BP} \tag{4.5}$$

where $\dot{y}$ is the elastic displacement rate at the loading points (This is equal to the cross-head speed if the plastic displacement is small) and B is a constant which can be determined either empirically by measuring the time taken for a crack to propagate along the length of a specimen at constant velocity in a constant displacement rate experiment or analytically [139] using the following equation (see Appendix A4.2)

$$B = \frac{3W_m^2}{Wd^3G} \tag{4.6}$$

where G is shear modulus of the material at the test temperature, W_m, W, d are D.T. specimen dimensions as shown in Fig. 4.8. In the present work B determined using either procedure has shown good agreement. The corresponding value for the stress intensity factor K_1 is calculated by substituting the plateau load in equation 4.3. The plateau load obtained at each $\dot{y}$ gives a single point on the K_1-V diagram and

Fig. 4.12: An illustration of the constant displacement method.

Fig. 4.13: An illustration of the constant load method (inset; SEM showing a typical crack during slow propagation).

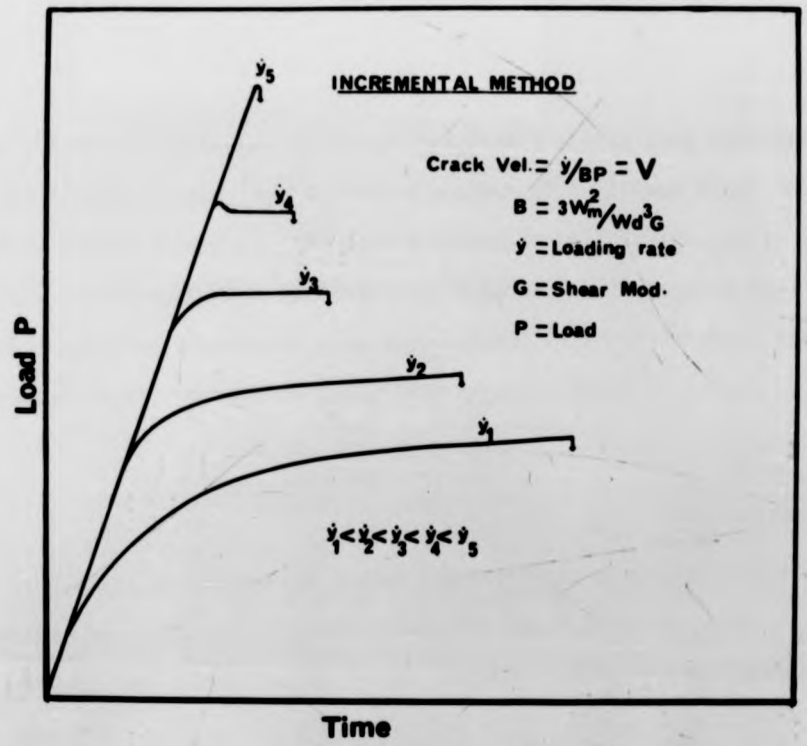

Fig. 4·12

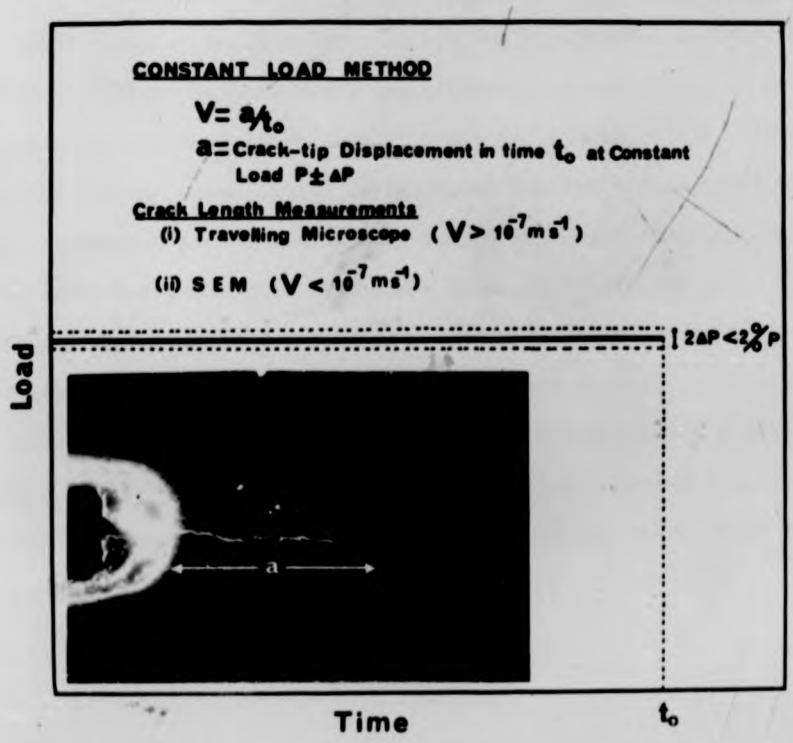

Fig. 4·13

usually several points can be determined from a single long specimen. For the specimens used in this work a maximum of 3 plateau loads were obtained before fracture. The data obtained in this manner, at constant temperature, can be readily used to calculate n value in $V = AK_I^n$ equation by substituting displacement rates and plateau loads in the following expression [125] (See Appendix A4.2)

$$n = \log \left(\frac{\dot{y}_1}{\dot{y}_2}\right) \Big/ \log \left(\frac{P_1}{P_2}\right) - 1 \qquad (4.7)$$

Similarly, an activation energy (Q) for crack propagation can be calculated by determining plateau loads (P_1 and P_2) for constant displacement rate $\dot{y}$ for two different temperatures T_1 and T_2 [125] (see Appendix A4.2)

$$Q = \frac{RT_1T_2}{(T_2-T_1)} (n+1) \ln \left(\frac{P_1}{P_2}\right) \qquad (4.8)$$

The upper limit of crack velocity which can be obtained in this way depends on the highest cross-head speed available in the machine. For low cross-head speeds non-plateau behaviour was observed ($\dot{y}_1$ in Fig. 4.12). It indicates that the plastic contribution to the total applied displacement and valid parameters can no longer be obtained from equation 4.5, because $\dot{y}$ is indeterminate. This limits the velocity range that gives the valid fracture mechanics parameters. (In this study, at 1400°C, plateau behaviour is observed only at velocities higher than 10^{-5} m s^{-1}). However, the velocity range below this is a crucial one for failure prediction and a suitable method is essential for measuring very small crack velocities. Hence the'constant-load' technique described below was used to measure small crack velocities.

4.2.2. (c) Constant Load Method

In this method a predetermined constant load, corresponding to a low K_1 value, was applied to the specimen by means of the load cycling facility of the Instron machine. As shown in figure 4.13, the cycling amplitude was adjusted to a minimum possible value to get very small load variations, ($2\Delta P < 2\%$ P). At constant load, crack propagation occurs at constant K_1 and hence with constant velocity. The crack velocity was obtained by direct measurement of crack tip displacement Δa in a predetermined time interval Δt ($V = \Delta a/\Delta t$). Previously [116,163] crack lengths were measured using fluorescent dye penetrant and very low crack velocities ($\sim 10^{-9}$ ms^{-1}) were obtained by applying a constant load for time interval up to 48 hours. Instead of this method a SEM was used to measure crack lengths and hence crack velocities one order of magnitude smaller (10^{-10} ms^{-1}) within 24 hours (a typical SEM image is shown in Fig. 4.13). Relatively long crack lengths (velocities corresponding to $> 10^{-7}$ ms^{-1}) were measured optically using a travelling microscope. One advantage of carrying out this experiment in vacuum is to obtain a clearer image of the crack, free from oxidation products.

This direct approach, although rather laborious has some advantages over the other two methods, particularly when crack propagation is accompanied by gross plasticity. (This is common in many ceramic materials at elevated temperatures). This method is not affected by other factors such as machine relaxation or variation in thermal equilibrium and this is the only method available to obtain data in the low velocity range of the K_1-V diagram.

In all these three methods the stress intensity factor K_1 was determined from the load using equation 4.3. Hence it is important to consider the effect of plastic displacement on relation between load and stress intensity factor. Fracture mechanics principles cannot generally be applied when crack propagation is accompanied by gross plastic deformation. In fact this is the normal behaviour of many ceramics materials at elevated temperatures. Analysis and experiments [129] have shown that the stress intensity factor after plastic deformation of the loading arms is less than the value calculated from equation 4.3, but the decrease is rather small even for plastic displacements several times the specimen thickness. Therefore the effect of plastic displacements on the stress intensity factor-load relation is very small at low crack velocities and negligible for materials which have very small plastic displacements. (This is the situation with sialon materials studied). Therefore the standard relation (equation 4.3) can be used to evaluate K_1 from load P at any temperature from a knowledge of Poisson's ratio corresponding to that temperature.

A room temperature Poisson's ratio was determined very accurately using sonic techniques [164]. Elastic modulus E and shear modulus G were determined from the resonance frequency of a rectangular bar (3 mm x 3 mm x 110 mm) and Poisson's ratio ν was calculated from following relation

$$\nu = \left(\frac{E}{2G} - 1\right) \qquad (4.9)$$

values of E and G were on average of six readings from 3 bars using both rectangular sides (Table 4.1).

Si-Al-O-N	Elastic modulus (E) G Pa	Shear modulus (G) G Pa	Poisson's ratio ν
B	278.0 $\pm$ 3.4	110.8 $\pm$ 0.92	0.25 $\pm$ 0.005
C	289.8 $\pm$ 3.6	113.4 $\pm$ 0.95	0.28 $\pm$ 0.005

Table 4.1: Elastic constants of ceramic B and C

The variation of elastic modulus with temperature was indirectly determined by measuring load deflection rates $(\frac{dP}{dt})$ of a four-point bend specimen in an Instron machine in a temperature range 20°C-1400°C. The elastic modulus is directly proportional to the deflection rate and at any temperature value was calculated from the room temperature resonance value, E_{RT}

$$E_T = E_{RT} \times \left[\left(\frac{dP}{dt}\right)_T \Big/ \left(\frac{dP}{dt}\right)_{RT}\right] \qquad (4.10)$$

There was a small load deflection rate due to the machine components and this was eliminated by performing an auxiliary experiment. Although this method is not very accurate (at high temperatures, due to a strain rate effect, values obtained in this method are normally lower than the actual values) the approximate variation with temperature can be obtained. The elastic modulus variation with temperature for ceramics B and C is shown in figure 4.14. Each point is an average of four readings from two specimens and the error-bars indicate an estimated error. Ceramic C shows an increase in elastic modulus at temperatures ∿ 800°C and then a slight reduction. This behaviour is similar to that reported [4] for bend strength variation with temperature (0°-1400°C) in CVD SiC and the apparent increase in strength is not understood. The behaviour of ceramic B is similar to that observed for hot-pressed Si_3N_4 [87]. In Si_3N_4 Poisson's ratio does not appear to change with temperature. This is possible if the elastic modulus and shear modulus vary in similar manner with temperature. This similar variation of E and G with temperature was also assumed here and the room temperature Poisson's ratio value was taken for all temperatures. It was not possible to obtain the variation of shear modulus with temperature experimentally and, therefore, it was calculated from Poisson's ratio value and elastic

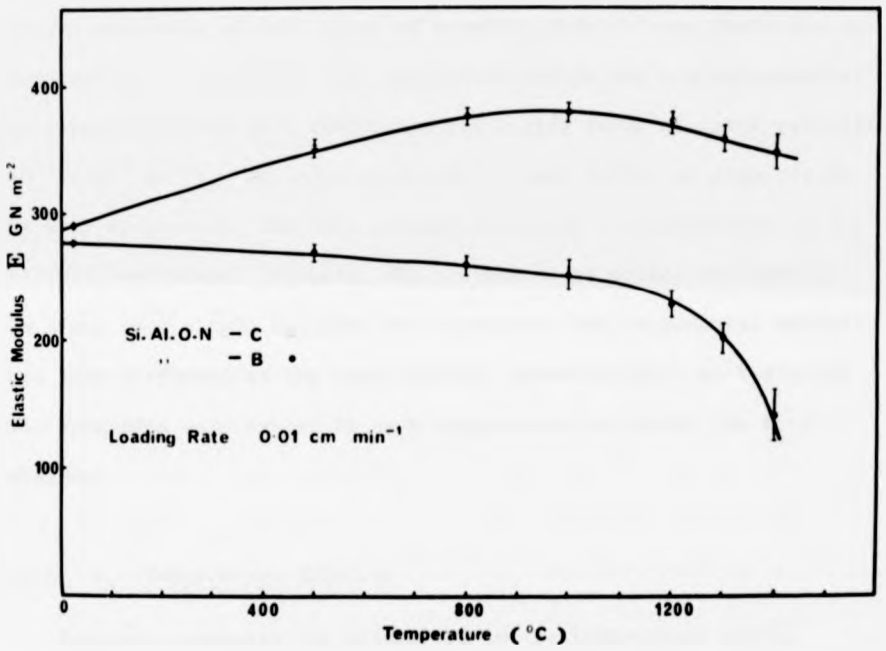

Fig. 4.14: The variation in Young's modulus with temperature for Si-Al-O-Ns B and C.

modulus value at the required temperature. These values were used together with specimen dimensions to calculate K_I and V. Special care was taken in measuring the thickness of the specimen because of it's third power dependence on K_I.

The validity of these three techniques was separately tested on several specimens of both types of ceramics (B and C) and there was an excellent fit to straight-line logarithmic plots for a given material and temperature and good continuity for a wide range of crack velocities (10^{-10}-10^{-2} ms^{-1}). In order to obtain as many points as possible on the K_I-V diagram all the test methods were used in combination in the following procedure. Firstly, the constant load method was used a few times on a single specimen and relaxation and incremental methods were then performed on the same specimen respectively. At least six D.T. specimens were tested at each temperature to obtain the K_I-V relation.

4.2.3. K_{Ic}-Temperature Relation

Fracture toughness was determined in the temperature range 20°C-1500°C using the single-edge notched beam (SENB) test in the four point bending mode in the vacuum furnace described in section 4.2.1 (a). The four-point bending mode was used in preference to three-point loading to avoid the difficulty of positioning the single upper loading point in three point loading and also to obtain a pure bending region. Furthermore, in three point loading the upper loading point is directly above the notch of the specimen and the contact stress of the upper loading point can interact with the stress at the root of the notch [165].

4.2.3. (a) K_{1c} Jig

The four-point jig consists of a recrystallised alumina tube, as the outer loading points and two small recrystallised alumina rods in a hemispherical alumina head, as inner loading points (Fig. 4.15). The hemispherical head permitted equal vertical loading on the specimen. Two small slots were made on either side of the alumina head to allow the specimen to fall down to the cooler region of the furnace immediately after fracture to avoid any possible oxidation even in the vacuum $\sim 10^{-5}$ torr. (These specimens were used for subsequent AES and SEM examination).

4.2.3. (b) Test Specimen Preparation

The specimens were machined with an annular diamond saw from larger pieces into rectangular bars (25 mm x 6 mm x 3 mm) which were notched to a depth of 1.8 mm (30% of the bar width). It has been shown [166] that a suitable relative notch length ($\frac{a}{W}$) for ceramic materials lies over a range $0.1 < \frac{a}{W} < 0.6$. As shown previously [167,168] it is not necessary to produce a sharp crack in ceramics to get accurate K_{1c} data. It is assumed that machining creates an atomically sharp crack at the root of the notch in ceramics. However it has been reported [166] that there is an increase in K_{1c} with increase in notch radius. Therefore the thinnest possible blade (notch radius $\sim$ 100 μm) was used for machining the notch. In ceramics, due to limited plasticity, the ratio of K_{1c}/σ_y (σ_y is the plastic yield stress) which determines the thickness b $\left[b > 2.5 \left(\frac{K_{1c}}{\sigma_y}\right)^2\right]$ of the test piece [142] is generally small. Therefore unlike in metals, small specimens can be used to obtain a reliable value for K_{1c}.

Fig. 4.15: The K_{1c}-jig.

Fig. 4.16: The K_{1c}-specimen.

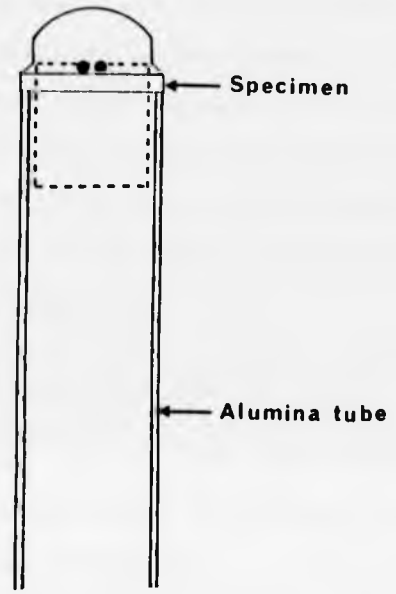

Fig. 4·15

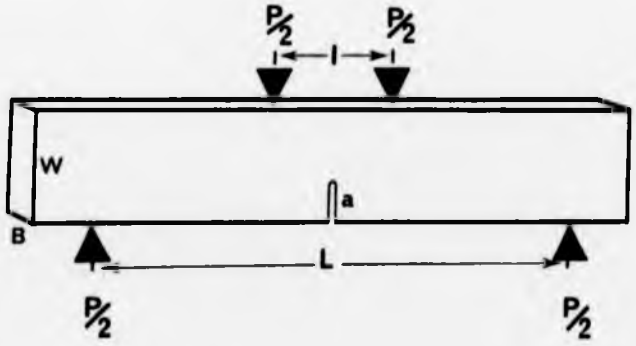

Fig. 4·16

4.2.4. The Testing Procedure

The SENB specimen was placed on the jig and introduced into the hot zone of the furnace (A small gap was kept between the jig and the upper loading rod to allow for thermal expansion). When the vacuum furnace was heated up to the required temperature the cross-head was moved slowly (speed $\sim$ .005 cm min^{-1}) until fracture occurred. The dimensions of the sample and fracture level P_f were substituted in the following formula to evaluate K_{1c} [169]

$$K_{1c} = \frac{3P_f d}{BW^2} \cdot a^{\frac{1}{2}} \left[3.86 - 6.15 \left(\frac{a}{W}\right) + 21.7 \left(\frac{a}{W}\right)^2\right]^{\frac{1}{2}} \qquad (4.10)$$

where d is bending arm = $\frac{(L-I)}{2}$ and L is outer span ($\sim$ 22 mm), I is inner span ($\sim$ 5 mm), W is specimen height, B is specimen width and a is depth of the notch as shown in Fig. 4.16.

There are four other relationships which can be used to determine K_{1c}, but it has been shown that K_{1c} is best evaluated for ceramics using the above relation [167].

APPENDIX 4.1

Stress and Strain Equations for Four-point Bend Creep Tests

The four-point bend creep test is analysed here in terms of creep compliance [161] and the general expressions are developed which relate the stress (σ) and strain (ε) to specimen dimensions (Fig. A4.1), applied load (P), load point deflection (Y_L) and to the stress exponent (n). In this treatment the neutral axis is assumed to be at the centre of the beam. (i.e. creep properties in tension and compression are identical). The strain ε at a distance z from the neutral axis is

$$\varepsilon = \frac{z}{\rho} \qquad \text{(A.1.1)}$$

where ρ is the radius of curvature of the neutral axis within the loading points.

In non-linear mechanics creep compliance J can be expressed in the form

$$J = \frac{\varepsilon}{\sigma^n} \qquad \text{(A.1.2)}$$

where σ is stress and n is the stress exponent.

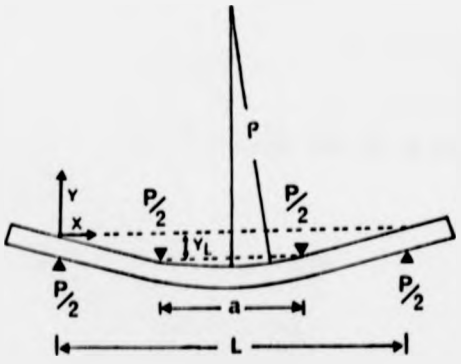

Fig. A 4·1

Combining equations A.1.1 and A.1.2

$$\sigma = \left[\frac{\varepsilon}{J\rho}\right]^{1/n} \qquad \text{(A.1.3)}$$

For a rectangular beam of width b and height h, the bending moment about the neutral axis (M) is defined as

$$M = \int_{-\frac{h}{2}}^{\frac{h}{2}} z\, \sigma b dz \qquad \text{(A.1.4)}$$

Substitution of Eqn. A.1.3 into A.1.4 and subsequent integration gives

$$M = \frac{I_n}{[J\rho]^{1/n}} \qquad \text{(A.1.5)}$$

where

$$I_n = \frac{2b\ (\frac{h}{2})^{\frac{2n+1}{n}}}{(\frac{2n+1}{n})}$$

and is defined as the complex moment of inertia.

The stress at a distance Z from the neutral axis

$$\sigma(Z) = \frac{Z^{1/n}(\frac{2n+1}{n})\ M}{2b(\frac{h}{2})^{\frac{2n+1}{n}}} \qquad \text{(A.1.6)}$$

Stress in the outer fibre, i.e. at $Z = \frac{h}{2}$

$$\sigma_o = \frac{2\ (2n+1)}{bh^2}\ M \qquad \text{(A.1.7)}$$

Bending moment (M) varies along the beam and it is constant and maximum within the loading points.

$$M = \frac{P}{2} \times \frac{(L-a)}{2} \quad \text{for } \frac{L-a}{2} < x < \frac{L+a}{2} \qquad \text{(A.1.8a)}$$

and $$M = \frac{Px}{2} \qquad 0 < x < \frac{L-a}{2} \qquad \text{(A.1.8b)}$$

$$\text{and} \quad \frac{L+a}{2} < x < L$$

Therefore the maximum outer fibre stress

$$\sigma_{max} = \frac{(L-a)}{2bh^2} P \frac{(2n+1)}{n} \qquad (A.1.9)$$

For a small beam deflection the radius of curvature is given by

$$\frac{1}{\rho} = \frac{d^2y}{dx^2} \qquad (A.1.10)$$

(y is the deflection at a position x along the beam, see Fig. A.1.1)

Substitution of Eqn. (A.1.10) into Eqn. (A.1.5) gives

$$\frac{d^2y}{dx^2} = J \left(\frac{M}{I_n}\right)^n \qquad (A.1.11)$$

This equation can be solved for load point deflection Y_L, using boundary values of M (Equations A.1.8a and A.1.8b) and also applying the following conditions

$$\frac{dy}{dx} = 0 \qquad \text{at} \quad x = \frac{L}{2} \quad \text{(mid point)}$$

and $$y = 0 \qquad \text{at} \quad x = 0 \quad \text{(end points)}$$

(It is assumed that $\frac{dy}{dx}$ is continuous at $x = \frac{(L-a)}{2}$).

The solution is therefore

$$Y_L = - J \left[\frac{P}{I_n}\right]^n \left(\frac{L-a}{2}\right)^{n+1} \left[\frac{L+a(n+1)}{2(n+2)}\right] \qquad (A.1.12)$$

(Note that Y_L is measured in the opposite sense to the y axis).

At the maximum stress and strain the creep compliance

$$J = \frac{\epsilon_{max}}{(\sigma_{max})^n} \qquad (A.1.13)$$

Combining equations (A.1.13), (A.1.12) and (A.1.9) gives

$$\epsilon_{max} = \frac{2h\ (n+2)}{(L-a)\left[L+a(n+1)\right]} Y_L \qquad (A.1.14)$$

When n = 1 (viscous creep), equations A.1.9 and A.1.14 reduce to simple elastic beam equations:-

$$\sigma_{max} = \frac{3(L-a)P}{2bh^2} \qquad (A.1.15)$$

and

$$\varepsilon_{max} = \frac{6h}{(L-a)(L+2a)} Y_L \qquad (A.1.16)$$

Since n is unknown these two equations (A.1.15 and A.1.16) are normally used to calculate creep strain and stress. However if n > 1 these are no longer valid.

The Influence of Span Ratio $(\frac{L}{a})$ on the Strain Calculation

Equation (A.1.14) can be written as

$$\varepsilon_{max} = K(n)\ Y_L$$

The proportionality constant K(n), in addition to its dependence on n, is also a function of L and a. The sensitivity of K(n) to n and to the ratio $\frac{L}{a}$ is shown in Fig. A.4.2 [161] in which ratio K(n)/K(1) is plotted for various values of L/a. (Where K(1) is the value of K(n) when n = 1). It is evident that as $\frac{L}{a}$ increases K(n) becomes more and more sensitive to the creep exponent and strain is much larger than that calculated from the elastic equation. In fact the constant K(n) for three-point bending (a = 0) has the maximum sensitivity to n. For small $\frac{L}{a}$ ratios the elastic equation gives a good approximation. However too small $\frac{L}{a}$ values may reduce the experimental sensitivity of the creep measurement. $\frac{L}{a}$ values near 2 fall in the limit of n insensitivity and give rise to reasonable experimental precision.

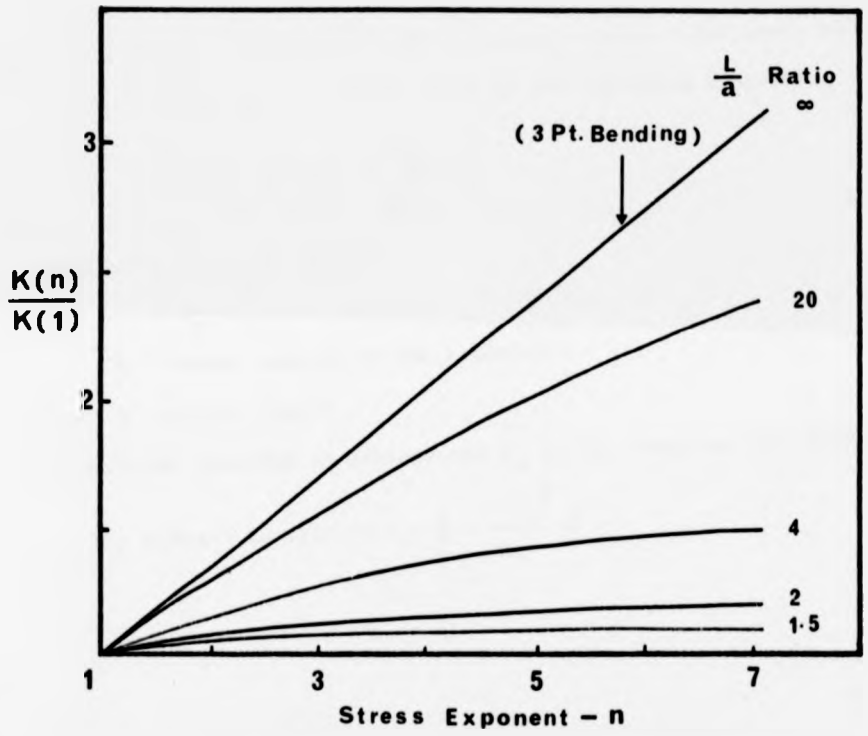

Fig. A.4.2. Outer-fibre strain sensitivity vs stress-exponent-n for different $\frac{L}{a}$ ratios.

APPENDIX 4.2

Stress Intensity Factor and Crack Growth Relations for the Double Torsion Technique

The double torsion specimen can be considered as two elastic torsion bars each having a rectangular cross-section loaded as indicated in fig. A4.3 to a load of $P/2$. The torsional strain θ for small deflections y for the bars with W >> d is given by the following expression [139]:

$$\theta \sim \frac{y}{W_m} = \frac{6\,\tau a}{Wd^3 G} = \frac{6\,W_m}{Wd^3 G} \times \frac{P}{2} \qquad \text{(A.2.1)}$$

where τ = Torsional moment

$= W_m \times \frac{P}{2}$

G = Shear modulus of the material

a = Crack length

W and d are specimen dimensions and W_m is the length of the bending arm.

The elastic compliance $C = \frac{y}{P} = \frac{3\,W_m^2}{Wd^3}\,\frac{a}{G}$ (A.2.2)

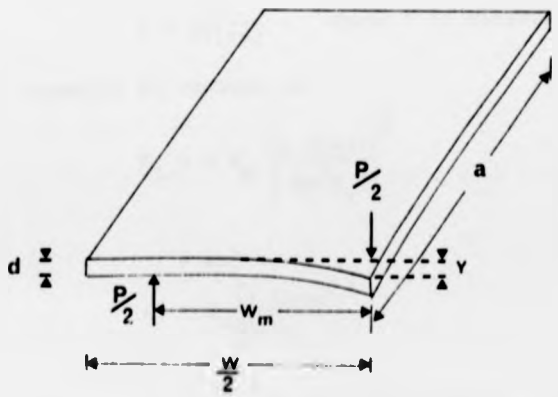

Fig. A 4·3

The strain energy release rate for crack extension, $\mathcal{G}$ is related to the specimen compliance by the expression

$$\mathcal{G} = \frac{P^2}{2}\left(\frac{dC}{dA}\right) \qquad (A.2.3)$$

where A = area of the crack.

If the shape of the crack front is independent of crack length (except for cracks approaching the end of the specimen);

$$A = a \times d_n$$

where d_n = plate thickness in the plane of the crack.

Then $$\mathcal{G} = \frac{P^2}{2d_n}\left(\frac{dC}{da}\right) \qquad (A.2.4)$$

By differentiating equation A2 with respect to a and substituting in equation A4 we get

$$\mathcal{G} = \frac{P^2}{2d_n} \cdot \frac{3\,W_m}{Wd^3G} = \frac{3P^2W_m^{\,2}}{2Wd^3d_nG} \qquad (A.2.5)$$

The stress intensity K is related to $\mathcal{G}$ by

$$K_1 = (E\,\mathcal{G})^{\frac{1}{2}} \qquad (A.2.6)$$

where E is elastic modulus, so

$$K_1 = \left[\frac{3\,EP^2W_m^{\,2}}{2\,Wd^3d_nG}\right]^{\frac{1}{2}} \qquad (A.2.7)$$

Since E and G are related by

$$G = \frac{E}{2(1+\nu)} \qquad \text{where } \nu \text{ is Poisson's ratio.} \qquad (A.2.8)$$

Therefore equation A7 reduces to

$$K_1 = P\,W_m\left[\frac{3\,(1+\nu)}{Wd^3d_n}\right]^{\frac{1}{2}} \qquad (A.2.9)$$

$$= A.P$$

where $$A = W_m\left[\frac{3\,(1+\nu)}{Wd^3d_n}\right]^{\frac{1}{2}}$$

The numerical factor 3 in this expression increases slightly

with the increase in specimen thickness. The value 3 is approximately correct (equation A1) as $\frac{W}{d}$ decreases [170]. Therefore for thicker specimens K_1 is higher than that given by equation A9 and it is better to use following equation [171]:

$$K_1 = P W_m \left[\frac{3 (1+\nu)}{W d^3 d_n (1 - 1.25 \frac{d}{W})}\right]^{\frac{1}{2}} \qquad (A.2.10)$$

It can be seen that the elastic compliance is linearly related to all crack lengths in equation A2 and vanishes when a = 0. But it can be seen from compliance calibrations that this is not true. Therefore the load point deflection of the D.T. specimen can be expressed accurately in the following way.

$$y = P (Ba + c) \qquad (A.2.11)$$

where B is the slope and c is the intercept of the compliance crack length calibration. Earlier analysis (from equation A2) shows that this slope is

$$B = \frac{3 W_m^2}{W d^3 G} \qquad (A.2.12)$$

Differentiating equation A.11 with respect to time (t) gives

$$\frac{dy}{dt} = (Ba + c) \frac{dP}{dt} + BPV \qquad (A.2.13)$$

where $V = \frac{da}{dt}$ (crack velocity).

For a fixed displacement (relaxation method) $\frac{dy}{dt} = 0$.

$$V = \frac{-(Ba + c)}{BP} \cdot \frac{dP}{dt} \qquad (A.2.14)$$

and $P(Ba + c) = P_i(Ba_i + c) = P_f(Ba_f + c)$ where a_i, P_i are initial values

and a_f, P_f are final values of crack length and load.

Therefore $$V = \frac{-P_i}{P^2}\left(a_i + \frac{c}{B}\right)\frac{dP}{dt} = \frac{-P_f}{P^2}\left(a_f + \frac{c}{B}\right)\frac{dP}{dt} \qquad (A.2.15)$$

For large a_i and a_f ($c << B$) the velocity equation reduces to

$$V = \frac{-a_i P_i}{P^2}\left(\frac{dP}{dt}\right) = \frac{-a_f P_f}{P^2}\left(\frac{dP}{dt}\right) \qquad (A.2.16)$$

Thus the crack velocity can be obtained directly from the rate of load relaxation at fixed displacement and initial or final crack length.

At constant displacement rate (Incremental method) it has been found that crack propagation occurs at constant load, when 'plateau' behaviour is observed. Then $\frac{dP}{dt} = 0$. The equation A.13 reduces to

$$\frac{dy}{dt} = \dot{y} = BPV$$

$$\text{and } V = \frac{\dot{y}}{BP} \qquad (A.2.17)$$

The generalised crack propagation equation at any temperature is given by (Section 2.2.2)

$$V = \alpha K_1^{\,n} \exp\left(\frac{-Q}{RT}\right) \qquad (A.2.18)$$

where α, n are constants and Q is the apparent activation energy for the slow crack growth mechanism. R is Gas constant and T is the absolute temperature.

Combining eqn. A9, $K = A.P$ and A.18; at constant temperature

$$\dot{y} \propto K_1^{\,n+1}$$

For two displacement rates $\dot{y}_1$, $\dot{y}_2$ and corresponding plateau loads P_1, P_2

$$\frac{\dot{y}_1}{\dot{y}_2} = \left[\frac{K_1'}{K_1''}\right]^{n+1} = \left[\frac{P_1}{P_2}\right]^{n+1} \qquad (A.2.19)$$

$$n = \log\left(\frac{\dot{y}_1}{\dot{y}_2}\right) \Big/ \log\left(\frac{P_1}{P_2}\right) - 1 \qquad \text{(A.2.20)}$$

Hence the load increment gives directly a value for the slope n of the K_1 - V diagram.

For a change in temperature from T_1 to T_2 and constant $\dot{y}$ equations

$$Q = \frac{R\ T_1\ T_2}{(T_2 - T_1)}\ (n+1)\ \text{In}\left(\frac{P_1}{P_2}\right) \qquad \text{(A.2.21)}$$

The activation energy can be obtained directly from the load increment method when n has been determined from equation A20.

$$n = \log\left(\frac{\dot{y}_1}{\dot{y}_2}\right) \Big/ \log\left(\frac{P_1}{P_2}\right) - 1 \qquad \text{(A.2.20)}$$

Hence the load increment gives directly a value for the slope n of the K_1 - V diagram.

For a change in temperature from T_1 to T_2 and constant $\dot{y}$ equations

$$Q = \frac{R\ T_1\ T_2}{(T_2 - T_1)}\ (n+1)\ \text{In}\left(\frac{P_1}{P_2}\right) \qquad \text{(A.2.21)}$$

The activation energy can be obtained directly from the load increment method when n has been determined from equation A20.

CHAPTER FIVE

HIGH TEMPERATURE CREEP

In this chapter bend and compressive creep data for the nominally single phase Sialon ceramics is analysed and possible high temperature creep mechanisms are discussed in relation to microstructural observations.

5.1. Analysis of Creep Data

5.1.1. Bend Tests

Fig. 5.1 shows a set of 4-point bend creep curves for various temperatures and stresses for Si-Al-O-N ceramics B and C with comparison plots for commerical Si_3N_4 and SiC [172] ceramics. The creep curves demonstrate the marked differences in average creep rate for a given temperature and stress, for the two ceramics (B and C) prepared with different additives. The creep resistance of B is inferior to a high grade Si_3N_4 (HS 130) and C shows a very low creep rate approaching to that of SiC after a long transient period. These observed creep strains under the same test conditions are similar to those listed in Table 3.1b (Lucas standard creep data). The Mn-containing ceramic exhibited a relatively low plastic strain and failure occurred showing a short tertiary creep region. In contrast, ceramic C exhibited very large strains ($\sim$ 4%) without creep failure. Creep failure occurred only at high stress levels and a tertiary creep region was not observed.

5.1.1. (a) Stress Dependence of Creep Rate

Stress exponents (n) for ceramic B (Fig. 5.2) at different temperatures, determined from incremental stress-change experiments, exhibit non-integral ($n \sim 1.5$-1.6) values typical of commercial Si_3N_4

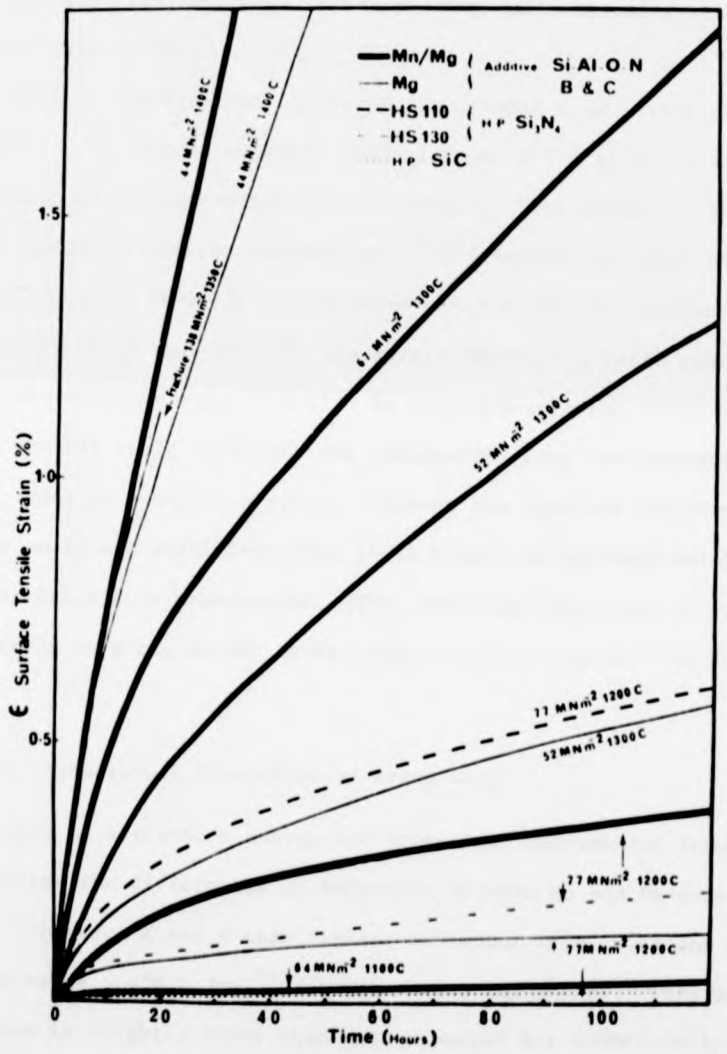

Fig. 5.1: Four-point bend creep curves for Si-Al-O-Ns B and C at different temperatures and stresses compared with creep curves at ∿ 1200°C for commercial Si_3N_4 ceramics and a hot-pressed SiC ceramic.

ceramics. These values are independent of sense of the changing stress (increasing or decreasing steps). Open and closed circles at 1300°C are for two separate specimens for decreasing and increasing stress increments respectively.

A contrary behaviour was observed for ceramic C in stress change experiments. The stress exponent changes from $n < 1$ to $n > 1$ depending on the sense of the incremental stress change. This effect is shown in Fig. 5.3 for two separate specimens at 1300°C (arrows indicate the sense of stress change). However the measured creep rates on a re-loaded specimen (the specimen which was used for the stress decreasing test) exhibited a linear stress dependence ($n \simeq 1$). In stress-decreasing tests a creep recovery process could influence the subsequent creep rate measurement and this leads to a higher n value. However the observed recovery rates were very small and sufficient time ($\sim$ 30 hours) was allowed before the subsequent creep rate measurement. This anomalous behaviour of ceramic C is explicable as a non-steady state creep behaviour and will be discussed later.

5.1.1. (b) Temperature Dependence of Creep Rate

Analysis of activation energy for creep via. incremental temperature tests confirms the differences in behaviour between Mn and Mg-containing ceramics. Ceramics A and B show similar behaviour (Fig. 5.4) and have an average value $\sim$ 488 k $Jmol^{-1}$ for the activation energy. This activation energy value is slightly lower than that reported for commercially available Si_3N_4 ($\sim$ 600 k $Jmol^{-1}$).

The temperature-variation tests on ceramic C (Fig. 5.5) show a similar transient behaviour as in the stress change test. The curves have an increasing negative slope with increasing temperature and time. The

Fig. 5.2: Stress-exponents (n) for creep of Si-Al-O-N B at various temperatures. Open and closed circles at 1300°C are for two separate specimens for decreasing and increasing stress increments respectively. Closed square symbols are from temperature-change experiments.

Fig. 5.3: Stress-exponent plots for Si-Al-O-N C.

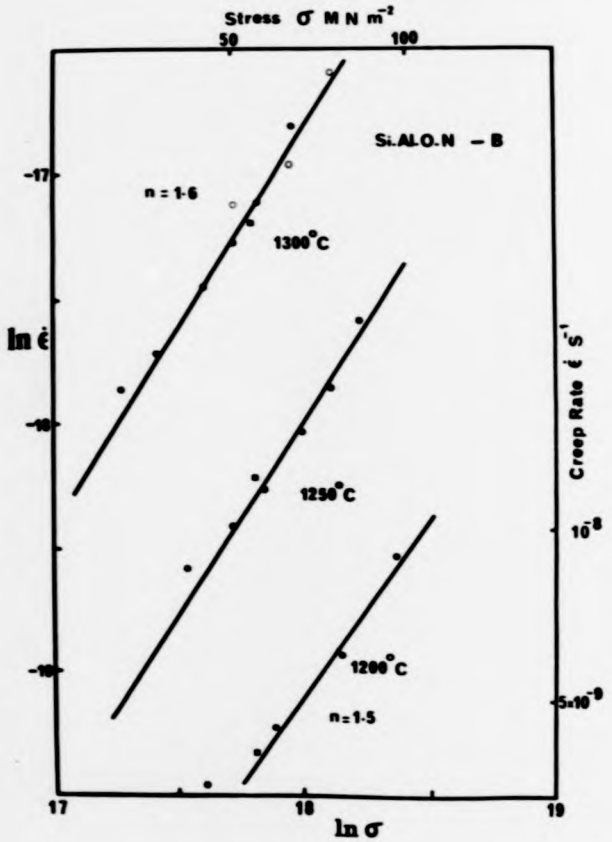
Stress σ MN m⁻²
50
100
Si.Al.O.N – B
n = 1·6
1300°C
1250°C
1200°C
n=1·5
ln ε̇
-17
-18
-19
Creep Rate ε̇ S⁻¹
10⁻⁸
5×10⁻⁹
17
18
19
ln σ

Fig. 5.2

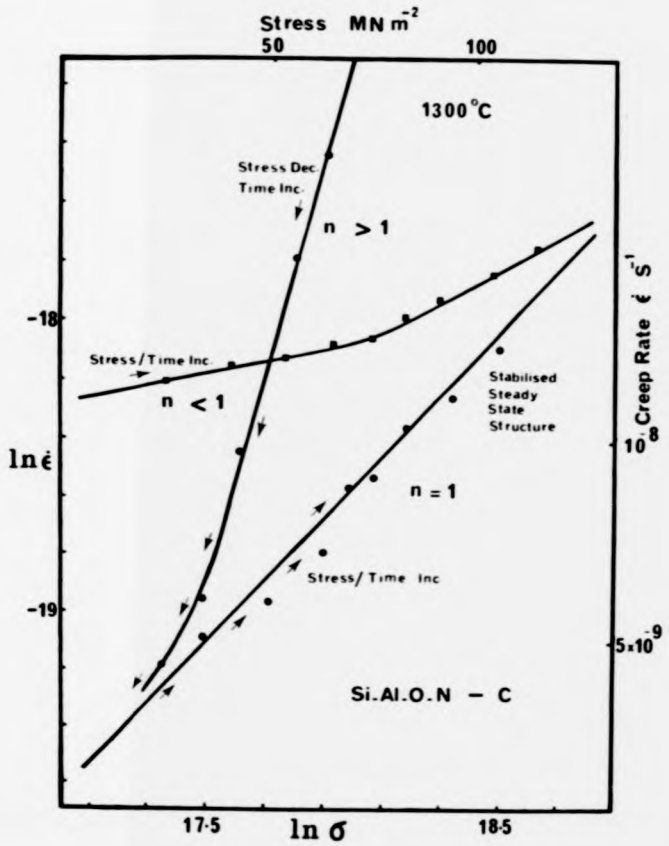
Stress MN m⁻²
50
100
1300°C
Stress Dec.
Time Inc.
n > 1
Stress / Time Inc.
n < 1
Stabilised
Steady
State
Structure
n = 1
Stress / Time Inc
Si.Al.O.N – C
ln ε̇
-18
-19
Creep Rate ε̇ S⁻¹
10⁻⁸
5×10⁻⁹
17·5
18·5
ln σ

Fig. 5.3

Fig. 5.4: Activation energy plots for Si-Al-O-Ns A and B.

Fig. 5.5: Activation energy plots for Si-Al-O-N C in air and vacuum.

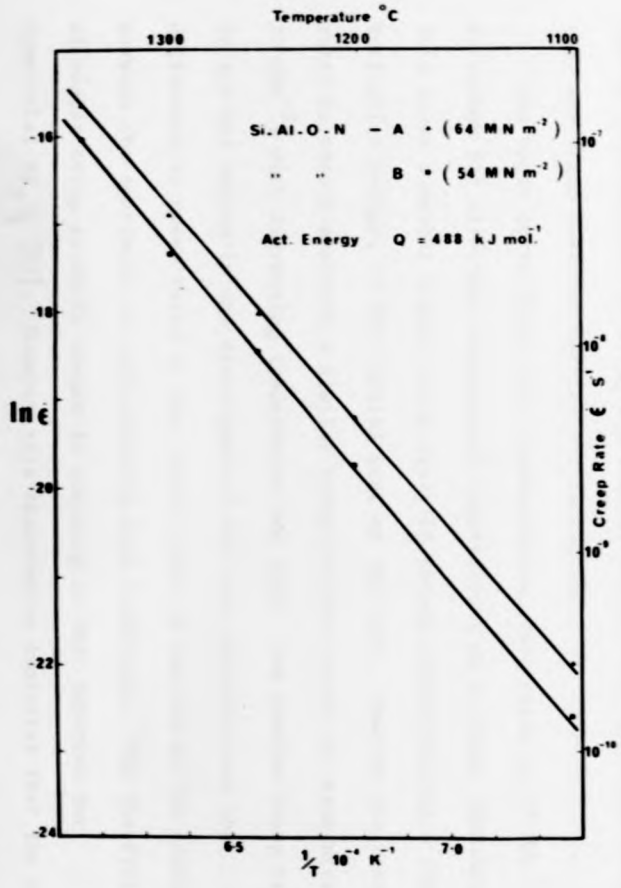
Temperature °C
1300
1200
1100
Si.Al.O.N — A • (64 MN m⁻²)
" " B • (54 MN m⁻²)
Act. Energy Q = 488 kJ mol⁻¹
ln ε̇
Creep Rate ε̇ S⁻¹
1/T 10⁻⁴ K⁻¹
6·5
7·0

Fig. 5.4

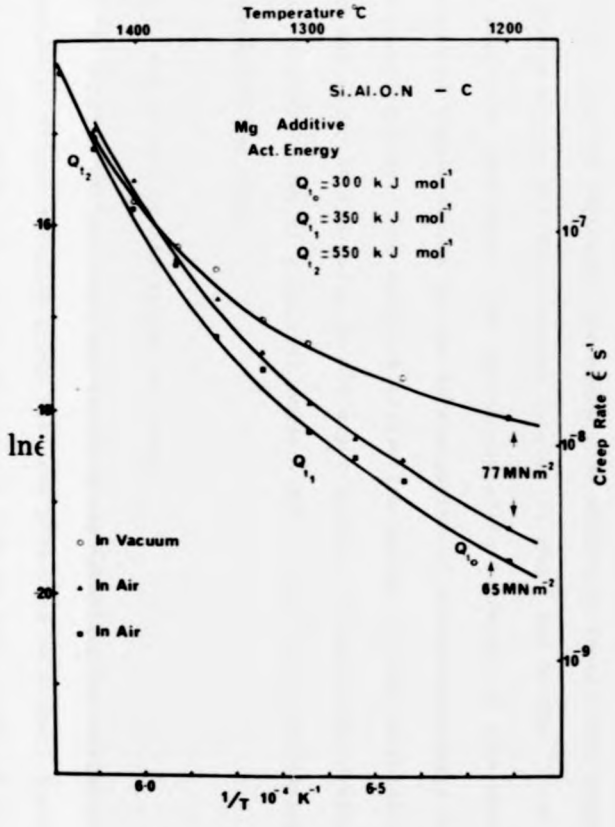
Temperature °C
1400
1300
1200
Si.Al.O.N — C
Mg Additive
Act. Energy
Q = 300 kJ mol⁻¹
Q = 350 kJ mol⁻¹
Q = 550 kJ mol⁻¹
77 MN m⁻²
65 MN m⁻²
○ In Vacuum
• In Air
• In Air
ln ε̇
Creep Rate ε̇ S⁻¹
1/T 10⁻⁴ K⁻¹
6·0
6·5

Fig. 5.5

lower two curves represent the creep rate variation in air with temperature increment at two different stress levels (77 MNm^{-2} and 65 MNm^{-2}) for two different specimens. The non-steady state behaviour of this material introduced complications in the determination of activation energy for the creep process. The apparent activation energy (Q) was calculated from the slope of the curve at different points. Q approaches a value $\sim$ 600 k $Jmol^{-1}$ from it s initial value $\sim$ 300 k $Jmol^{-1}$ with increasing temperature and time.

5.1.1. (c) Effect of Atmosphere on Creep

To examine whether this non-steady state behaviour is related to an atmospheric effect a vacuum creep test was performed on a small 4-point bend specimen (3 mm x 3 mm x 25 mm, span L = 20 mm and a = 10 mm) in the Instron vacuum furnace ($\sim 10^{-5}$ torr). A constant load was applied by means of the load cycling device in the Instron machine. The strain was measured using a LVDT which was mounted on the Instron cross-head. Due to inconvenience in using the Instron machine for long creep runs only one creep test was carried out in vacuum.

The upper curve (Fig. 5.5) represents the creep rates at 77 MNm^{-2} in vacuum for different incremental temperatures on a single specimen. This shows somewhat higher creep rates in vacuum characterising a lower activation energy, in the initial part of the test. However the creep rates in vacuum approach a similar value to that in air (at same stress 77 MNm^{-2}) with increasing temperature and time. The similar creep rates in air and vacuum in the final part of the test indicate that the difference in creep rates in the initial part is not due to the scatter between the specimens or difference in test techniques. The observation of higher creep rates in vacuum is contrary to that reported for commercial Si_3N_4 [87]. However this observation indicates that the non-

steady state behaviour of ceramic C is sensitive to the test environment.

5.1.1. (d) Effect of Transient Creep Behaviour on Creep Parameters

The extensive transient creep behaviour of ceramic C is clearly evident from fig. 5.6 in which the creep rate under a constant stress (44 MNm^{-2}) and temperature (1400°C) is plotted against time. During this transient period a stress or temperature increment test will not show the correct creep response and will lead to lower n or Q values. Stress increment tests performed at the end of this creep test resulted in $n \sim 0.9$ (Fig. 5.7 upper curve). A similar test on another specimen at 1350°C (allowed 72 hours for the transient period) resulted in $n \sim 0.8$ (Fig. 5.7 lower curve). This experiment clearly demonstrates the effect of transient behaviour on creep parameters (n and Q) and explains the observed behaviour of ceramic C. Although these observations indicate that this behaviour is not due to the test method (the limitations of the bend test have been discussed at the beginning of Chapter 4) the stress and temperature variation tests were repeated in uniaxial compression to avoid any complications. More recently a similar observation of a decrease in creep rate with time, under compressive creep conditions has been observed on different Si_3N_4 alloys [173].

5.1.2. Compressive Creep Data

Fig. 5.8 shows the stress ($\sim$ 50-250 MNm^{-2}) exponent plots for ceramics A and B. For comparison, compressive creep data for commercial Si_3N_4 (HS 130) [174] has also been included. Both ceramics (A and B) exhibit less stress-sensitivity than that of HS 130, but show slightly higher creep rates at low stress levels. The stress exponent value ($\sim$ 1.5) is similar to that obtained from bend tests, but the creep rate for a given

Fig. 5.6: Decrease in creep rate with time at a constant temperature and stress (Si-Al-O-N C).

Fig. 5.7: Stress-exponent (n) plots for Si-Al-O-N C after long test-times. Open circles are from temperature variation tests.

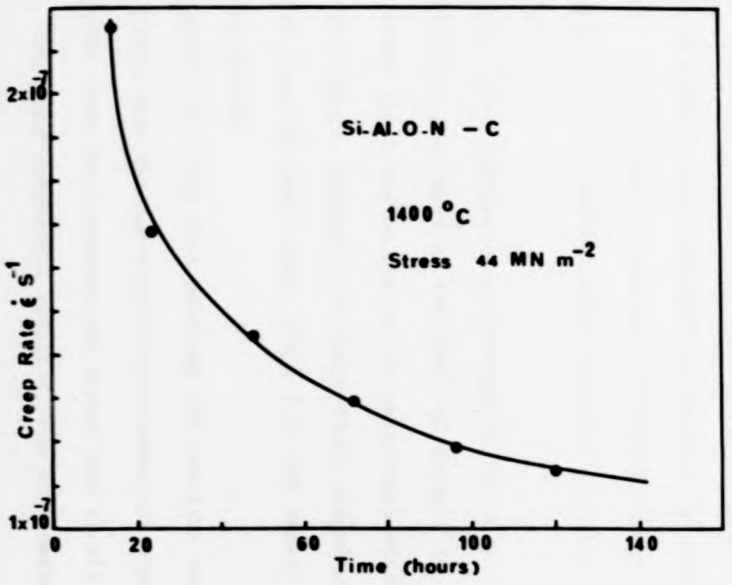
Si-Al-O-N – C
1400 °C
Stress 44 MN m^{-2}
Creep Rate $\dot{\epsilon}$ s^{-1}
2x10^{-7}
1x10^{-7}
0
20
60
100
140
Time (hours)

Fig. 5.6

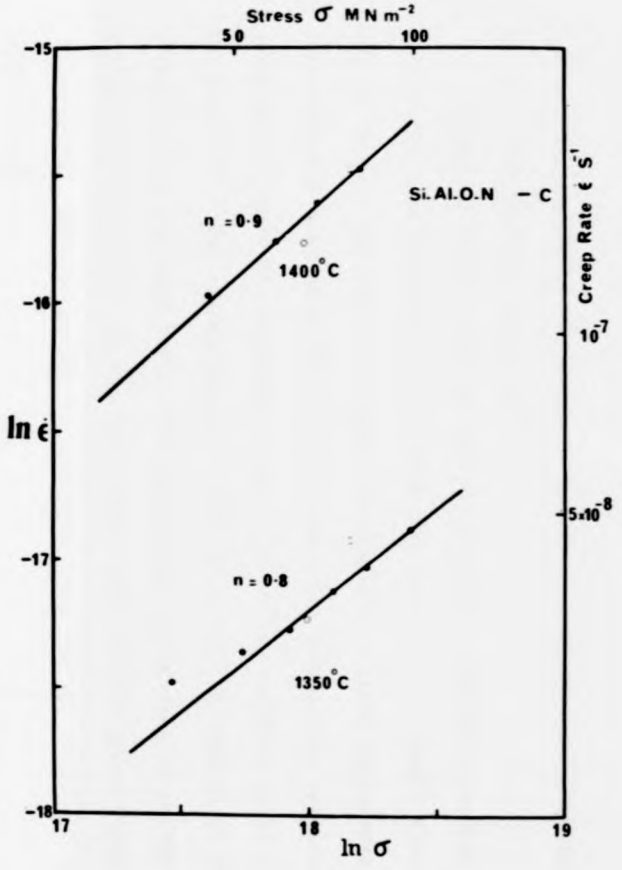
Stress σ MN m^{-2}
50
100
Si-Al-O-N – C
n = 0·9
1400°C
n = 0·8
1350°C
ln $\dot{\epsilon}$
Creep Rate $\dot{\epsilon}$ s^{-1}
10^{-7}
5x10^{-8}
−15
−16
−17
−18
17
18
19
ln σ

Fig. 5.7

stress and temperature is nearly a factor of 2 slower which is similar to that reported for Si_3N_4 [175].

Ceramic C (lower curve of fig. 5.9) shows a similar variation with stress and time to that obtained from the bend test at 1300°C (the dotted line). The upper straight line (closed circles) represents a stress-change test at 1350°C in which the creep rates were obtained allowing 72 hours for transient creep (similar to the bend tests shown in fig. 5.7). The stress exponent value ($n \sim 0.8$) is similar to that obtained from the bend test. The compressive creep rate of ceramic C is approximately equal to the bend creep rates under a given stress and temperature. This behaviour is different from that of ceramic B and Si_3N_4 [175].

Fig. 5.10 shows the effect of temperature on creep rates for sialon A, B and C. Ceramics A and B show similar temperature dependence, but A has slightly higher creep strength as observed in stress dependence experiments. A and B have an average activation energy of $\sim$ 482 k $Jmol^{-1}$ which is similar to the earlier value obtained from the bend tests ($\sim$ 488 k $Jmol^{-1}$).

The lower curve represents an average of two sets of data obtained from two different specimens at 160 MNm^{-2} of ceramic C. The small ce scatter in creep rates may be due to the structural differences between individual specimens. However, the temperature dependence is similar to that obtained from the bend tests (Fig. 5.5) and shows a similar variation 16). in activation energy. c

The compressive creep data confirms the previous bend-creep results and demonstrates that the non-steady state behaviour observed in ceramic C does not result from the inhomogeneous stress and strain within bend specimens. The creep parameters obtained from both methods are listed in Table 5.1.

Fig. 5.8: Stress-exponent plots for Si-Al-O-Ns A and B (compressive creep).

Fig. 5.9: Stress-exponent plots for Si-Al-O-N C (compressive creep).

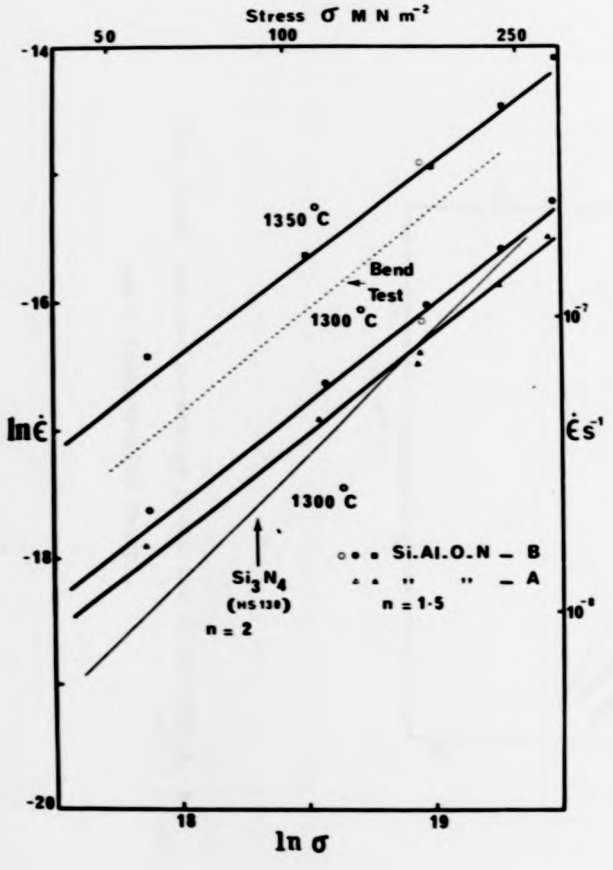

Fig. 5.8

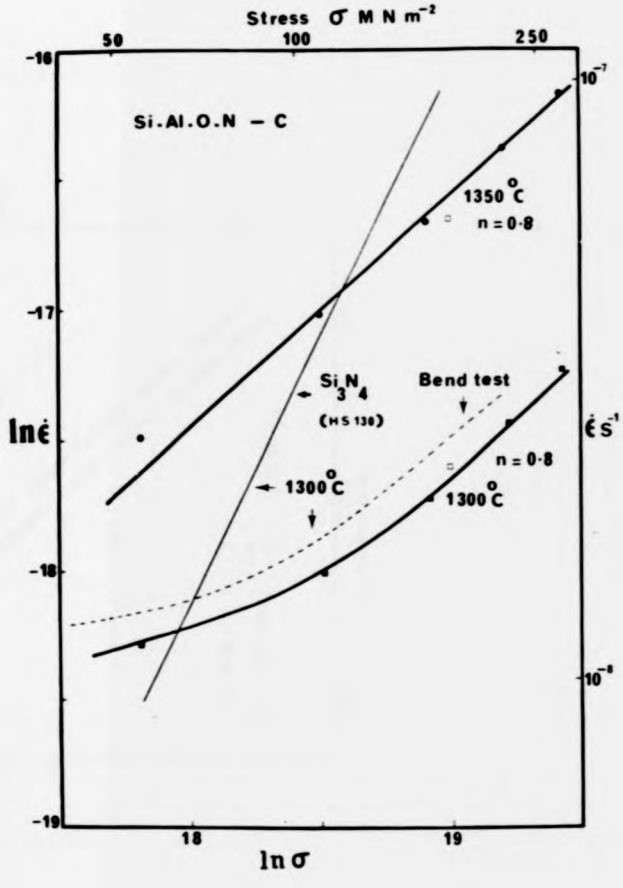

Fig. 5.9

ic .16). nce

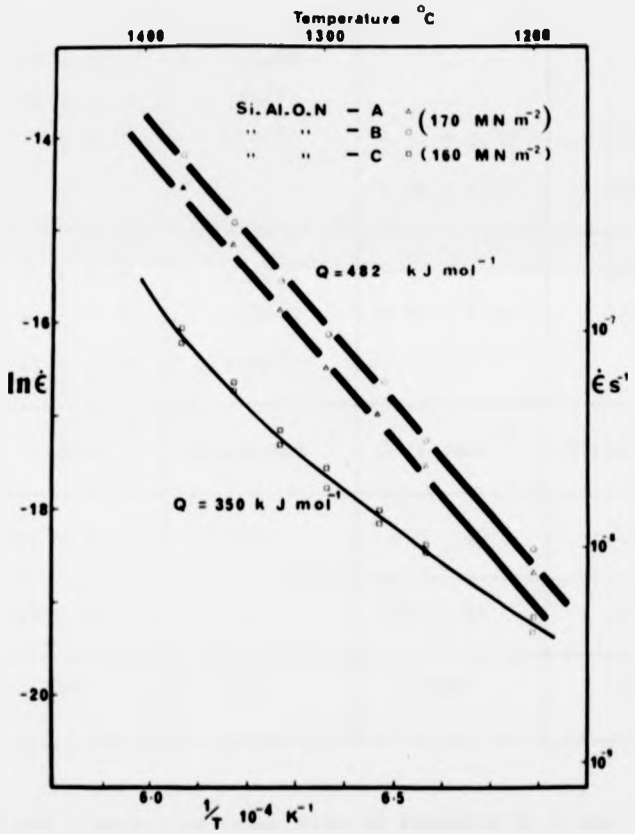

Fig. 5.10: Activation-energy plots for Si-Al-O-Ns A, B and C (compressive creep).

Si-Al-O-N ceramic	Bend Tests		Compressive Tests	
	n	Temperature	n	Temperature
A	-	-	1.52 ± .15	1300°C
B	1.46 ± 0.19	1200°C	-	-
	1.52 ± 0.12	1250°C	-	-
	1.56 ± 0.11	1300°C	1.51 ± 0.08	1300°C
	-	-	1.56 ± 0.07	1350°C
C	1.04 ± 0.06	1300°C	-	1300°C
	0.82 ± 0.11	1350°C	0.82 ± 0.06	1350°C
	0.86 ± 0.09	1400°C	-	-
	Q k $Jmol^{-1}$	Stress MNm^{-2}	Q k $Jmol^{-1}$	Stress MNm^{-2}
A	483 ± 11	64	479 ± 17	170
B	492 ± 18	54	485 ± 14	170
C	∿ 350	77	∿ 350	160

Table 5.1: Bend and Compressive Creep Data of Ceramics A, B and C.

(Owing to the transient behaviour of these ceramics, the measured creep rate for the initial stress level is slightly higher than that anticipated from the subsequent experimental points and therefore these data points were not used in calculating the slope using least square method [176]).

5.2. Microstructural Analysis of the Deformed Specimens

Ceramics A and B which have non-integral ($n > 1$) stress exponents are observed to undergo extensive cavitation, initiated at grain triple-junctions throughout the range of creep strain. These are imaged in electron-transparent sections (thin slices were cut from the pure bending section parallel to the stress axis) as isolated cavities which frequently have prism-plane facets formed probably via. surface diffusion (Fig. 5.11). As these cavities only appeared in the deformed specimens, it is unlikely that they were created during the ion-beam thinning. Furthermore, the observation of cavities in thicker regions of the specimen (Fig. 5.12) confirms that they were not created during the ion-beam thinning (a JEM 200 Electron Microscope, 200 kV was used to observe thicker regions). It was also observed that the cavities begin to form at a very early stage (within the primary creep region) in the creep test. Fig. 5.13 shows the cavitation of a specimen which was crept for 12 hours at 1300°C (about 0.4% strain). At larger creep strains the cavities occupy whole grain facets, occasionally interconnecting to form large internal cracks. Other than cavities the microstructure was characterized by similar features that were observed before creep. The Mn-rich particles were still present as fine particles with similar distribution.

In contrast the microstructures of ceramic C before and after creep deformation were indistinguishable (Figs. 5.14 & 5.15). There was no evidence for cavitation even after large creep strains. This marked difference in the deformation behaviour between the two types of ceramics was clearly visible in the macroscopic appearance of crept specimens (Fig. 5.16). The extensive surface cracking observed in bend creep specimens of ceramic A and B is a direct result of cavitation. Creep fracture surfaces exhibited a roughened area adjacent to the tensile side of the bend

Fig. 5.11: T.E.M. showing cavitation in Si-Al-O-N A (deformed at 1400°C).

Fig. 5.12: 200 kV T.E.M. showing cavities in thicker regions of Si-Al-O-N B.

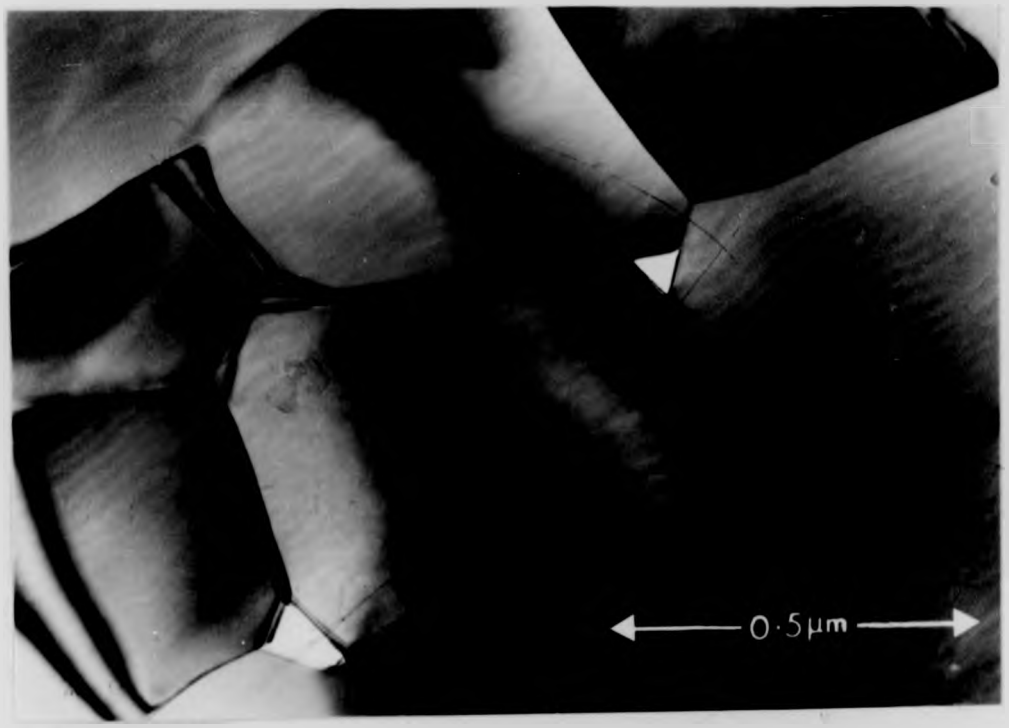

Fig.5·11

Fig.5·12

Fig. 5.13: Cavitation of Si-Al-O-N B within the primary creep region (12 hours, ∿ 0.4% strain).

Fig. 5.14: T.E.M. showing non-cavitating behaviour of Si-Al-O-N C after ∿ 4% strain.

Fig.5·13

Fig.5·14

Fig. 5.15: The absence of cavitation in Si-Al-O-N C even under a relatively large stress ($\sim$ 138 MNm^{-2}).

Fig. 5.16: Bend-creep specimens of Si-Al-O-Ns B and C.

Fig.5·15

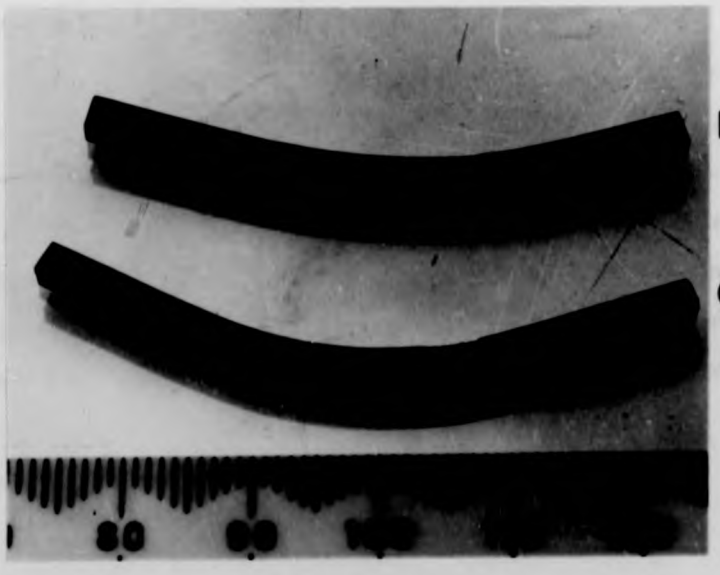

Fig.5·16

specimens and fracture mode was intergranular. These fracture surfaces were similar to the high-temperature K_{1c}-fracture surfaces which will be discussed in chapter six. The compressive specimens contained a small crack parallel to the stress axis. Ceramic C showed no visible surface cracks even after large creep strains ($\sim$ 4%). The creep failure of this material occurred only at high stress levels due to a single crack and the fracture surface was smooth and flat, unlike ceramics A and B.

In both types of ceramic no detectable grain growth or grain elongation along the stress axis was observed in the microstructure of the deformed materials. Dislocations were observed very occasionally in the microstructure and there was no visible change in their density after deformation. Furthermore, dislocation motion is unlikely to occur at the test temperatures in these predominantly covalent β-Si_3N_4 type ceramics [88,89] and hence the contribution of dislocation motion to the creep strain can be neglected.

5.3. Mechanisms for Creep

The creep parameters, particularly stress exponent values, for both types of ceramic indicate a marked difference in creep behaviour. This difference has further been amplified by the microstructural observations. The cavity growth and hence decrease in the effective area supporting the applied load could be responsible for the observed non-Newtonian behaviour ($n > 1$) of the Mn-containing ceramics. Therefore the creep mechanisms in these ceramics (A and B) is likely to be that of grain boundary sliding in which the shape-accommodation is mainly via. cavitation (Fig. 5.17a). The sliding of grain boundaries due to an

Fig. 5.17: Schematic drawings showing creep mechanisms in
(a) Si-Al-O-Ns A and B and
(b) Si-Al-O-N C.

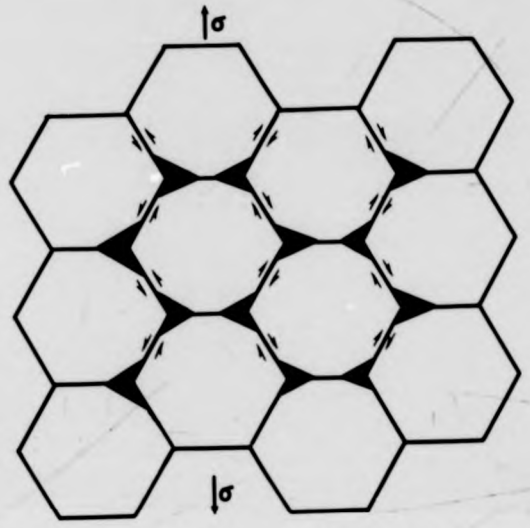

Grain-Boundary Sliding Accommodated By Cavitation

a

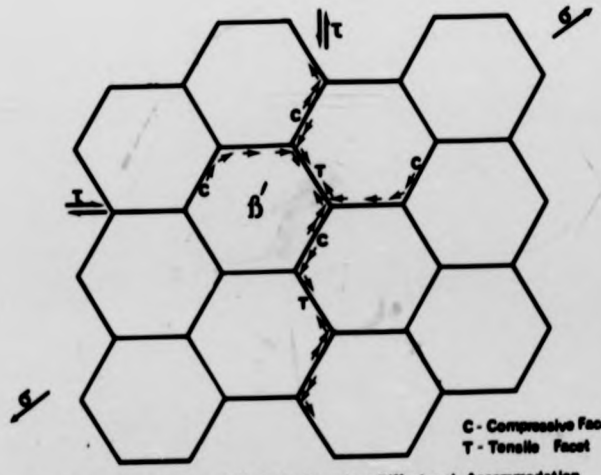

Grain-Boundary Sliding With Grain-Boundary Diffusional Accommodation

b

Fig.5·17

applied stress develops stress concentrations at irregularities in the grain boundaries such as triple junctions. These stresses can be relieved either by diffusional processes or cavity formation. Triple junction glass in the Mn containing ceramic provides ideal sites for cavity nucleation at the test temperatures. The possibility of cavity nucleation due to the Mn-rich particles observed in the grain boundaries is not favoured by the experimental observations on heat-treated deformed specimens (this will be discussed in chapter seven). However, as mentioned previously in section 2.1.6, the creep parameters (n and Q) measured under the condition of varying internal stress caused by cavitation are unlikely to provide a meaningful indication of the rate controlling mechanism.

In ceramic C the approach of stress exponent value to unity and the absence of cavitation indicate that a diffusional process could be the dominant stress-relieving mechanism in which diffusion can occur either along grain boundaries (Coble creep) or through grains (Nabarro-Herring creep). However, the activation energy for lattice diffusion in these predominantly-covalent ceramics should be comparatively high and therefore it is unlikely that the lattice diffusion is the dominant mechanism in these ceramics at the test temperatures. The evidence for a grain boundary diffusional mechanism operating in ceramic C is provided by the observed non-steady state behaviour, which will be discussed in the next section. Therefore the rate controlling creep mechanism operating in ceramic C is most likely to be grain boundary sliding accommodated by grain boundary diffusion [36,38]. In this model (Fig. 5.17b) diffusional flow of matter from compressive facets to tensile facets along the grain boundaries (Coble creep) provides the

accommodation for grain boundary sliding. However it is not possible to identify the rate controlling species via. the Coble creep equation because of the absence of data for grain boundary diffusion in Si-Al-O-N ceramics. For Coble creep the steady state creep rate $\dot{\varepsilon}$ is given by [36]

$$\dot{\varepsilon} = \frac{14\pi\sigma\Omega\delta D_b}{kTd^3}$$

The symbols have the same meaning as before (see section 2.1.1). Although in this model the deformation is described in the tensile mode it should be equally valid in the compressive mode. It was also observed in ceramic C, that the creep rate in compression and in bending are nearly equal under the same test conditions and therefore to calculate the grain boundary diffusion coefficient for the Si-Al-O-N system, compressive creep data as well as bend creep data can be used. However, due to the non-steady state creep behaviour of this material the calculated diffusion coefficients may show somewhat higher values. This could be avoided in using approximate steady-state creep values obtained in the final part of a activation energy plot, which is approximately linear. The estimated values for δD_b at 1375°C from compressive and bend data are listed below.

$$\delta D_b \approx 6 \times 10^{-26}\ m^3\ s^{-1} \quad \text{(From compressive data)}$$

$$\delta D_b \approx 10 \times 10^{-26}\ m^3\ s^{-1} \quad \text{(From bend data)}$$

The atomic volume Ω was taken as $1.06 \times 10^{-29}\ m^3$, which was estimated from the unit cell volume. As there was no measurable grain growth observed during creep tests the initial mean grain size 1.25 μ was used for d. Assuming the effective grain boundary width δ is similar to that obtained in lattice imaging (7 Å), the grain boundary diffusion coefficient can be obtained. Thus the average D_b from both test methods;

$$D_b \simeq 1 \times 10^{-16} \, m^2 \, s^{-1}$$

This grain boundary diffusion coefficient together with the activation energy can be used to obtain the diffusion equation. However, as discussed in the next section the progressive change in boundary structure with the de-segregation of impurities from grain boundaries could result in a 'stabilised' structure to give a 'limiting' value for the activation energy which probably approaches that for diffusion of Si etc. (or some compound 'molecular' species) within a 'pure' grain boundary. This could be achieved via. heat treatments and will be discussed in chapter seven together with the determination of diffusion coefficient.

5.4. Non-Steady State Creep

It has been shown that the metallic impurities (Mg, Ca, Mn etc.) diffuse into the surface oxide film during oxidation of these ceramics [177] (A similar observation was made on the surface oxide layer of the crept specimens). From Auger electron spectroscopy it was concluded (section 3.2.2b) that these impurities (Ca, Mg etc.) are segregated to the boundary within a few atomic spacings of each crystal. Therefore during the creep tests in air progressive escape of segregated impurities into the surface oxide film will change the boundary impurity level and structure which may reduce the grain boundary diffusion rate. It is believed that this progressive decrease in boundary impurity level could increase the density of co-valent Si-N type atomic bonds across the grain boundaries to give higher grain boundary cohesion. The activation energies for grain boundary diffusion of β' components are simultaneously increased resulting in the time-dependent reduction in creep rate and 'artificial' values for n and Q. Therefore, the changing

gradient with temperature in the activation energy plot is not caused by a change in rate controlling diffusion from grain-boundary to lattice. A single creep mechanism has been confirmed by obtaining a single slope in the activation energy plot for a whole range of test temperatures (1200 - 1425°C) on heat-treated specimens (this study will be discussed in chapter seven).

The evidence of higher creep rates and a lower activation energy in vacuum (Fig. 5.5) favours the above explanation for the non-steady state behaviour. The slow variation in apparent activation energy in vacuum and the gradual approach of the creep rates to that in air is possibly due to a slow oxidation (a thin oxide film was observed on the crept specimen) in vacuum (hence a slow outward diffusion of impurities) or a solid solution of impurities within β′ crystals (or both). However, in view of the time scale for the change in creep rate, the dominant mechanism must involve oxidation, otherwise diffusion rates within β′ crystals must be unrealistically slow (diffusion distances are less than grain sizes of ∿ 1 μm).

The sensitivity to environment also does not support the possibility of the changing creep rate resulting from grain growth. To explain the extreme values of creep rates ($\dot{\varepsilon}$) observed under constant stress-temperature conditions (Fig. 5.6), the mean grain size would need to change by at least 10% if Coble creep is assumed ($\dot{\varepsilon} \propto \frac{1}{d^3}$). However, no measurable change in mean grain size was observed in deformed specimens.

In the Mn-containing ceramics, a similar de-segregation and hence a progressive reduction in impurity concentration at the grain boundaries could lead to a gradual improvement in creep resistance. However, this effect was not apparent in the Mn-containing ceramics as in ceramic C, possibly due to the dominance of cavitation, which in turn increases the creep rate. Hence the observation of an approximately steady-state

creep in the Mn-containing ceramics may be due to a fortuitous combination of the competing processes of cavitation and desegregation.

5.5. Discussion

The major difference in creep behaviour between the two types of ceramic results from the presence or absence of intergranular cavitation. Cavitation would allow deformation to continue at a faster rate than a diffusion-controlled process and this, in addition to an increased effective stress, would account for the higher creep rate observed in cavitating ceramics (A and B) compared to the non-cavitating ceramic (C) under given creep conditions. In these cavitating ceramics a diffusional process could also partially contribute to the creep strain and the accommodation process in grain boundary sliding could be accomplished by partially via. cavitation and partially via. diffusion.

The observation of different creep behaviour of ceramics A (or B) and C in compression further amplifies the difference between the two deformation mechanisms operating in these ceramics. It has been shown that in a compression test the tensile stresses developed are small compared to the applied compressive stress and the formation of grain boundary cavities depends on tensile stress developed across the boundary [95]. This would result in less cavitation in compression and hence a lower creep rate. This behaviour was evident in ceramics A and B which are susceptible to cavitation. Ceramic C exhibited nearly the same creep rates in both testing modes and this is consistent with the expected behaviour related to diffusional deformation.

This difference in the creep behaviour between the two ceramics is directly related to their observed microstructure. Cavitation is believed to be caused by the occurrence of microscopic (< 1000 Å) regions of triple-junction silicate glass phase which is a residue of the densification process (Chapter 3). Apart from triple-junctions,

there was no resolvable difference between β′ grain boundaries in the two ceramics within the lattice-image resolution set by the β′ prism plane spacing and the instrumental capability. Cavities may nucleate within the triple-junction phase at low stresses if the silicate is above it s glass transition temperature during the creep test. The Mg-containing ceramic (C) contains no detectable triple junction glass and hence the cohesive energy of the grain boundary is sufficient to prevent cavity nucleation up to the maximum stress and temperature studied. From Auger electron spectroscopy it was concluded that grain boundaries contain segregated impurities (Mg or Mn, the 'accidental' impurity Ca, together with oxygen). The progressive escape of these impurities from grain boundaries during creep tests results in the time-dependent reduction in creep rate.

It is believed that the presence of triple-junction glass in the Mn-containing ceramic is the result of a very low solubility of Mn in β′ crystals. In the case of Mg, there is some evidence for a small solubility of Mg in β′ crystals [178]. The solid solution of Mg may reduce the residual silicate glass via. simultaneous solid solution of charge compensating oxygen. The inability to demonstrate non-cavitating behaviour even in high purity Si_3N_4 ceramics containing Mg additives (This contains a residual grain boundary glassy phase) demonstrates the importance of Al-substituted ceramics in controlling the residual silicate phase [31]. It has been observed that the solubility of Mg in β′ increases slightly with Al substitution level [178].

Finally, an intentional oxidation could be effective in extracting metallic ions from grain boundaries and therefore creep data obtained from a pre-heat-treated (in an oxidising environment) specimen could

be used to calculate the diffusion coefficient of a rate-controlling species of β′ crystal within a relatively impurity-free grain boundary. This approach and a calculation of diffusion coefficients will be discussed in chapter seven.

CHAPTER SIX

HIGH TEMPERATURE FRACTURE

This chapter presents an analysis of high temperature fracture data and discusses high temperature slow crack growth mechanisms for the two Si-Al-O-N ceramics in their 'as hot-pressed' condition.

6.1. Analysis of Fracture Data

6.1.1. K_I-V Measurements

The crack velocity (V)-stress intensity (K_I) data at different temperatures (1100°C-1400°C) is presented for ceramics B and C in Fig. 6.1. There is an excellent fit to straight line logarithmic plots for a given material and temperature and good continuity for a wide range of crack velocities (10^{-10} - 10^{-2} ms^{-1}) using the different techniques discussed previously (section 4.2.2.).

As in the creep behaviour, ceramics B and C exhibit markedly different characteristics. The stress intensity exponent (n) for ceramic B has a single value (n = 6.9 ± 0.2 at 1400°C) above ∿ 1300°C throughout the range of K_I but below this temperature it exhibits a 2-stage behaviour, rising to n ∿ 40 near to K_{Ic} (∿ 5 $MPam^{\frac{1}{2}}$) with a reversal in temperature dependence. This is similar to the K_I-V characteristics for commercial silicon nitride ceramics [19]. In ceramic C the crack growth rate is characterised by a single slope (n = 13.5 ± 0.4 at 1400°C) for the entire crack velocity range studied. This material shows a relatively low sensitivity to temperature changes, unlike ceramic B. Ceramic C exhibits a remarkable behaviour of zero crack velocity below a critical K_I for a given temperature ($K_I \leq 0.25\ K_{Ic}$ at 1400°C; Fig. 6.1). Several 'constant-load' experiments were performed below this K_I level and instead of crack-propagation a

Fig. 6.1: K_I-V diagram for Si-Al-O-Ns B and C. The dotted lines represent the K_I limit below which sub-critical crack growth is suppressed.

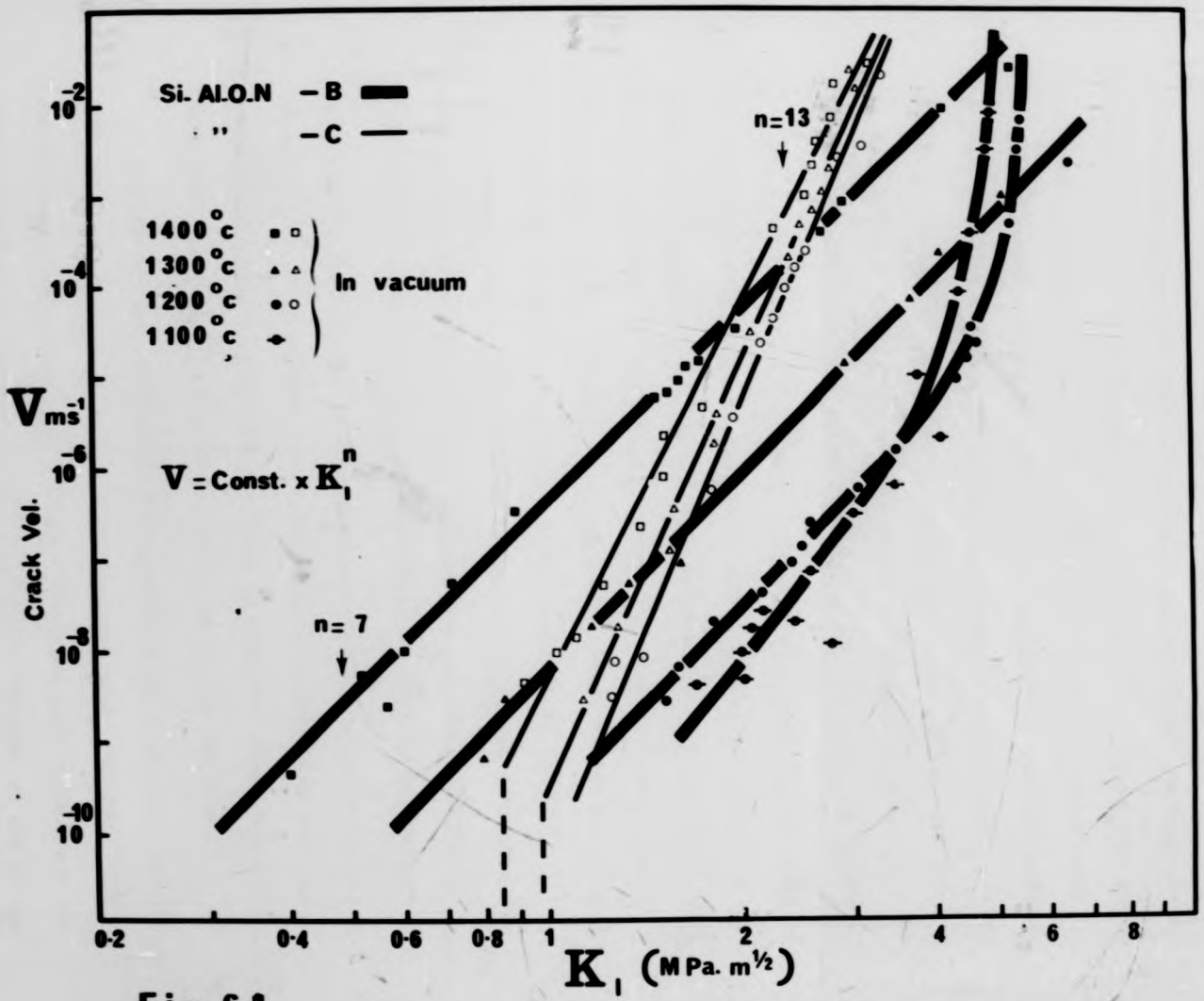
Si. Al.O.N — B
" — C
1400°c
1300°c
1200°c
1100°c
In vacuum
V = Const. x K1n
n=13
n= 7
Crack Vel.
Vms-1
10-2
10-4
10-6
10-8
10-10
0·2
0·4
0·6
0·8
1
2
4
6
8
K1 (MPa. m½)

Fig. 6·1

localised zone of anomalous contrast was observed on the surface of the specimen around the notch-tip (Fig. 6.2). It is important to note that when a sharp crack was initiated (above the critical K_1, before re-stressing below this level) a similar crack-stabilising effect occurred, but at a slightly lower critical K_1 and the plastic zone was not clearly resolved. This zone was present only after testing below the critical level and is believed to be a topographic contrast produced by grain rotation due to a localised diffusional creep deformation which (at low K_1 levels) is effective in relaxing stresses to suppress sub-critical crack growth. This type of behaviour was not observed in ceramic B even at very low stress intensities ($K_1 \leq 0.05\ K_{1c}$ at 1400°C).

The measured activation energy Q for the slow crack growth process (see Appendix A.4.2) was calculated for both ceramics using data in the lower region of the K_1-V diagram in the temperature interval 1200-1400°C. The average values of activation energies for ceramics B and C are $\sim 800\ kJmol^{-1}$ and $\sim 500\ kJmol^{-1}$ respectively. These values are higher than that obtained for creep deformation, particularly for the 'cavitating' ceramic. The reported values for Si_3N_4 (HS 130) also show similar differences in activation energies for the two processes ($Q_{creep} \sim 600\ kJmol^{-1}$ and $Q_{crack\ growth} \sim 900\ kJmol^{-1}$). This is probably an 'artificial' increase due to increased internal stress-intensity caused by cavitation. Furthermore, the rate-controlling mechanism for slow crack growth may not be directly related to that for creep, hence the activation energies for the two processes may not be the same.

In Fig. 6.3 the 1400°C data for ceramics B and C are also re-plotted for comparison together with published data for Si_3N_4 (HS 130) [129] and for hot-pressed SiC [115]. However in making such comparisons one should note that the maximum K_1 for a particular ceramic is set by the value of K_{1c} (this is high for ceramic B and HS 130 than for ceramic C and SiC). It is also observed that there was a small reduction in

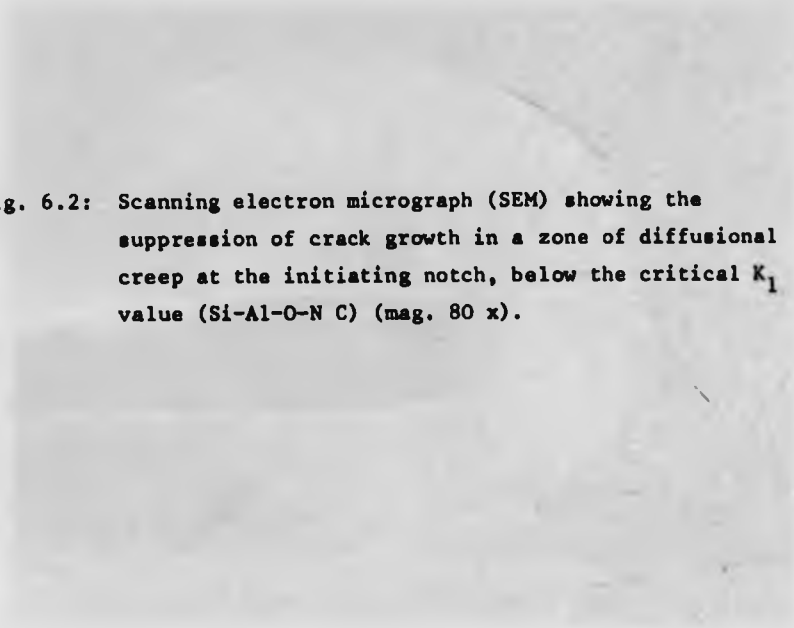

Fig. 6.2: Scanning electron micrograph (SEM) showing the suppression of crack growth in a zone of diffusional creep at the initiating notch, below the critical K_1 value (Si-Al-O-N C) (mag. 80 x).

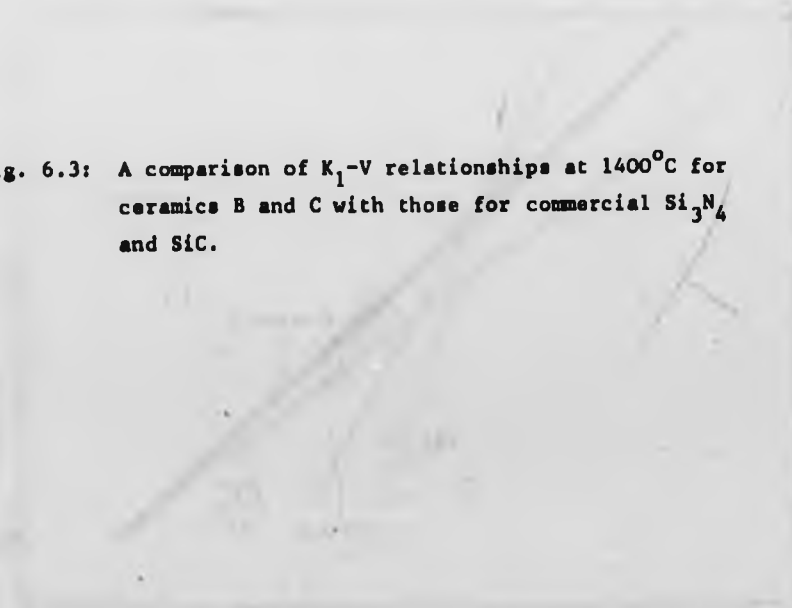

Fig. 6.3: A comparison of K_1-V relationships at 1400°C for ceramics B and C with those for commercial Si_3N_4 and SiC.

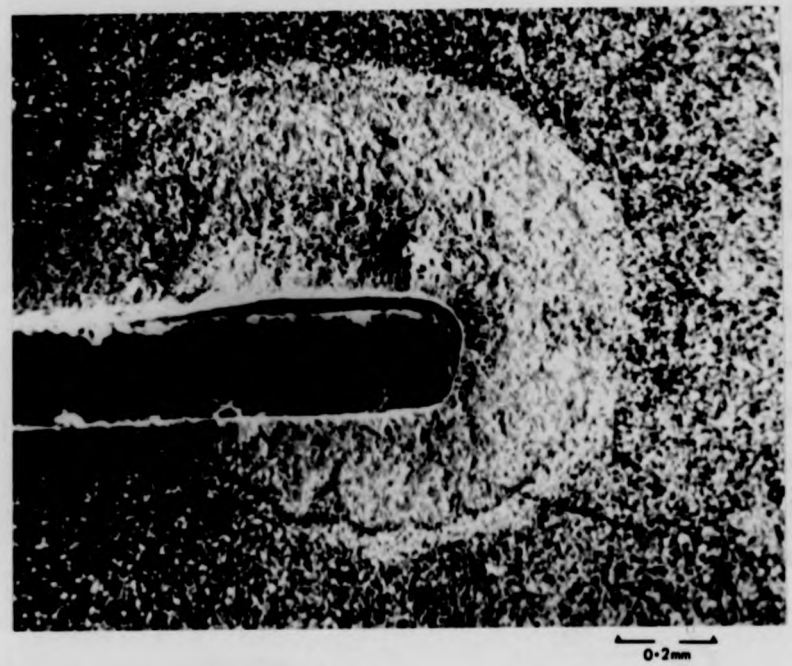
0·2mm

Fig.6·2

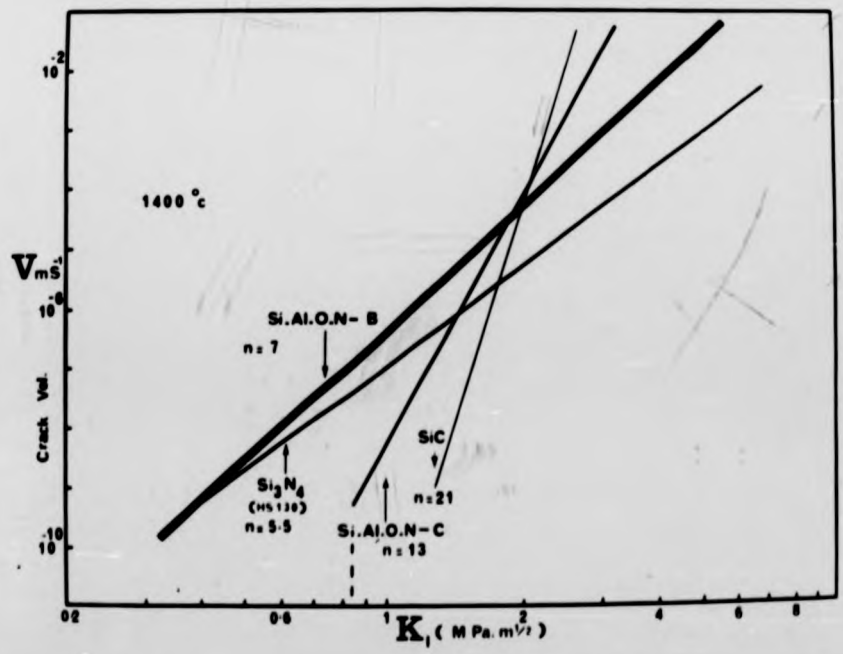
1400 °c
Vms⁻¹
Crack Vel.
Si.Al.O.N- B
n: 7
Si3N4
(HS130)
n: 5·5
Si.Al.O.N-C
n: 13
SiC
n: 21
K1 (M Pa. m1/2)

Fig. 6·3

gradient of the K_1-V plot with increased specimen thickness (2 mm to 3 mm) which is prominent only for the cavitating ceramic, increasing V by more than an order of magnitude in the lower velocity region (Fig. 6.4). This effect is partly due to the error in the calculation of K_1 using equation 4.3 assuming $\frac{d}{\omega} << 1$, where d is the specimen thickness and ω the specimen width (see equations A.9 and A.10 in Appendix A.4.2). However this error is very small and is the same for the thicker specimens of both types of ceramic. As the thickness effect is pronounced only in the cavitating ceramic, it is likely that the effect is related to the increase in internal stress-intensity caused by cavitation. However it is not clear why the cavity density increases ahead of the crack front in thicker specimens under the same external stress condition.

Finally, it is worth mentioning that the K_1-V data have been recorded under high-vacuum conditions over short times compared with the creep tests and hence the effect of a time-dependent grain boundary structural change which gave rise to the non-steady state creep behaviour (section 5.4) is negligible and not apparent in the K_1-V relation.

6.1.2. K_{1c}-Temperature Tests

The variation of critical stress intensity factor (K_{1c}), in the temperature range 20°C - 1500°C for ceramics A, B and C is shown in Fig. 6.5 in which each point is an average of two to five tests. The K_{1c}-temperature variation has previously been studied for ceramic A [32] and was repeated in the present programme with the other two ceramics B and C. The behaviour of ceramic B is almost identical to that observed for ceramic A [32] and a similar zone of sub-critical

Fig. 6.4: The effect of specimen thickness on the K_I-V relation.

Fig. 6.5: Variation in the critical stress-intensity factor (K_{Ic}) with temperature for Si-Al-O-Na A, B, C, D and E.

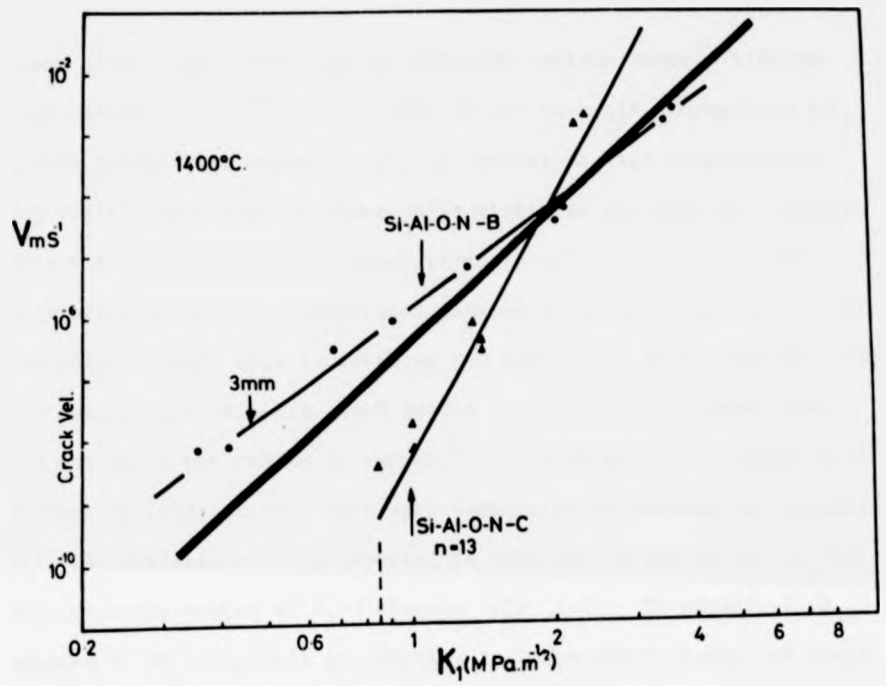
1400°C
Si-Al-O-N-B
3mm
Si-Al-O-N-C
n=13
Crack Vel.
$V_m s^{-1}$
K_I(M Pa.$m^{-1/2}$)

Fig.6·4

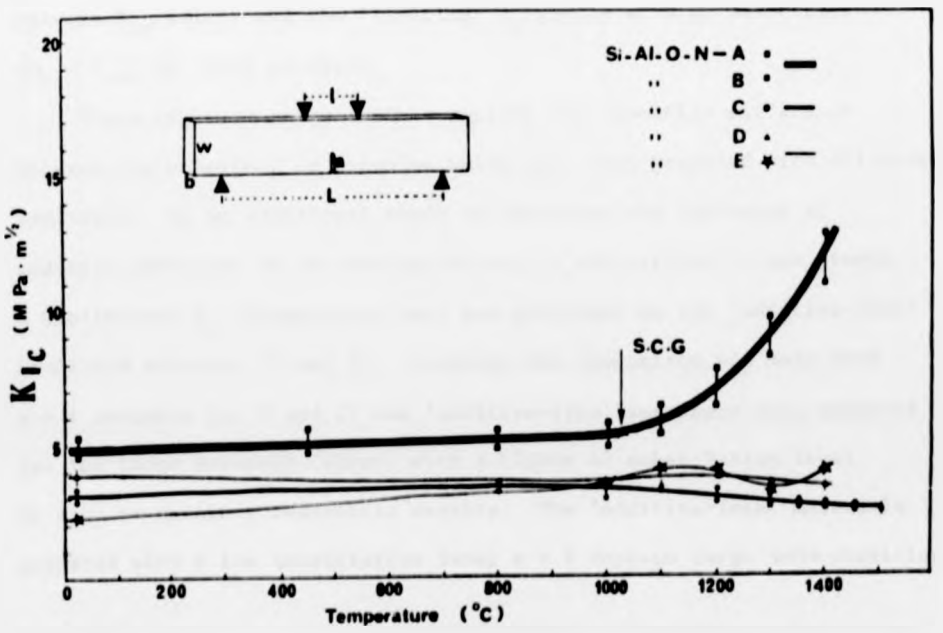
Si-Al-O-N-A
B
C
D
E
S.C.G
K_{IC} (MPa·$m^{1/2}$)
Temperature (°C)

Fig.6·5

crack growth was visible on the fracture surface above a critical temperature ($\sim 1100^{o}C$). This zone is due to crack propagation at stress intensities below K_{1c} during loading at high temperatures and visible as a zone of lower reflectivity on the fracture surface. This effect, which is also characteristic of Si_3N_4 ceramics [114], is visible on the K_{1c}-temperature diagram as an increase in K_{1c} when the initial crack size is taken as the sawn notch depth together with the zone of sub-critical crack growth. It was also observed that the extent of the region of sub-critical crack growth increases with decreasing strain rate. This high temperature behaviour is consistent with the observation of a reversal in temperature dependence in the high velocity region of K_1-V diagram (Fig. 6.1). In ceramic C, K_{1c} appears to be relatively insensitive to temperature change and there was no evidence for a zone of sub-critical crack growth even after a very low strain rate fracture test at $1500^{o}C$. The comparison between K_{1c}-temperature and K_1-V temperature diagrams show a reasonable agreement between K_{1c} values and the 'limiting' K_1 values at high velocities ($K_1 \rightarrow K_{1c}$) for both ceramics.

These fracture tests further amplify the essential difference between the behaviour of ceramics which have been prepared with different additives. As an additional study to determine the influence of additive chemistry on the susceptibility to sub-critical crack growth, a preliminary K_{1c}-temperature test was performed on two 'additive-free' Si-Al-O-N ceramics (D and E). Although the comparison was made with $x = 1$ ceramics (A, B and C) the 'additive-free' specimens were prepared (at the Lucas Research Centre) with a higher Al substitution level ($x = 2$) to obtain a reasonable density. The 'additive-free' materials prepared with a low substitution level $x = 1$ contain large pore densities

which could mask the effect of the temperature variation. It is believed that the densification in $x \simeq 2$ ceramics is assisted by the silicate liquid formed at $\sim 1600^{\circ}C$ from the reaction between SiO_2 and AlN or Al_2O_3. These two ceramics D and E, in which no triple-junction glass was observed, showed a similar behaviour in the K_{1c}-temperature test to that of ceramic C and no evidence for a slow crack growth zone was observed (Fig. 6.5). This comparison re-emphasises the importance of additive chemistry in relation to high-temperature mechanical properties.

At low temperatures ($< 1100^{\circ}C$) ceramics A and B have a nearly constant value for K_{1c} (~ 4.8 $MPam^{\frac{1}{2}}$) which is similar to that reported for commercial Si_3N_4 [19]. The mean K_{1c} value for ceramic C (~ 3 $MPam^{\frac{1}{2}}$) is less than that of ceramics A and B. The lower mean value of K_{1c} for ceramic C may result from it s more equiaxed grain morphology, providing a less tortuous intergranular crack path. As discussed previously, the Mn-containing ceramic is believed to retain a larger volume fraction of liquid silicate phase during the final stages of densification and this favours an increase in the c/a ratio of grain dimension in the hexagonal prism morphology [178]. The elongated nature of grains may lead to a higher grain pull-out during crack propagation and this could increase the effective K_{1c}. An alternative explanation is the crack-'blunting' effect of the relatively weak grain boundaries normal to the direction of fast crack propagation in the Mn-containing ceramic. A difficulty with such explanation is the observation of substantial transgranular fracture (as discussed below) in both ceramics at low temperatures where the difference in K_{1c} is still apparent.

6.2. Microstructural Analysis of Fracture Surfaces

6.2.1. K_{1c}-Fracture Surfaces

Fig. 6.6a is a low magnification scanning micrograph of a high-temperature (1400°C) fracture surface (K_{1c}-fracture surface) of specimen B. The slow crack growth zone (A) was distinguishable from the fast fracture zone (B) due to the topographic contrast of it's undulating surface. This surface topography is similar to that previously observed on specimen A [32]. The extremely rough slow-fracture zone indicates a gross deviation of the crack path from the mean fracture plane during propagation. The creep fracture surfaces of ceramic B also showed a similar appearance adjacent to the tensile side of the bend specimen. The extent of the slow crack growth zone (A) varied with the test temperature and was not visible below 1100°C. As mentioned previously, the slow crack region has been included in calculating K_{1c} at high temperatures ($\geq$ 1100°C). In contrast, the fracture surface of ceramic C (Fig. 6.6b) was macroscopically flat and similar to the low temperature fracture surface of either ceramic. Low-temperature fracture of these ceramics was predominantly transgranular (Fig. 6.7) which was characterised by large flat regions containing many β′ grains. The proportion of intergranular fracture increases with temperature and above 1200°C the fracture surface of ceramic B (or A) was completely intergranular (Fig. 6.8 at 1400°C) in both slow and fast zones.

6.2.2. K_I-V Fracture Surfaces

For ceramic B the amount of fracture surface undulation was observed to vary with temperature and velocity. The fracture surfaces above 1300°C were extremely rough for all crack velocities

Fig. 6.6: (a) SEM showing the differences in fracture surface topography between the region of slow crack growth (zone A) and a region of fast fracture (zone B) of Si-Al-O-N B (1400^{o}C) (mag. 30 x).

(b) The absence of a slow crack growth zone in Si-Al-O-N C (1400^{o}C) (mag. 30 x).

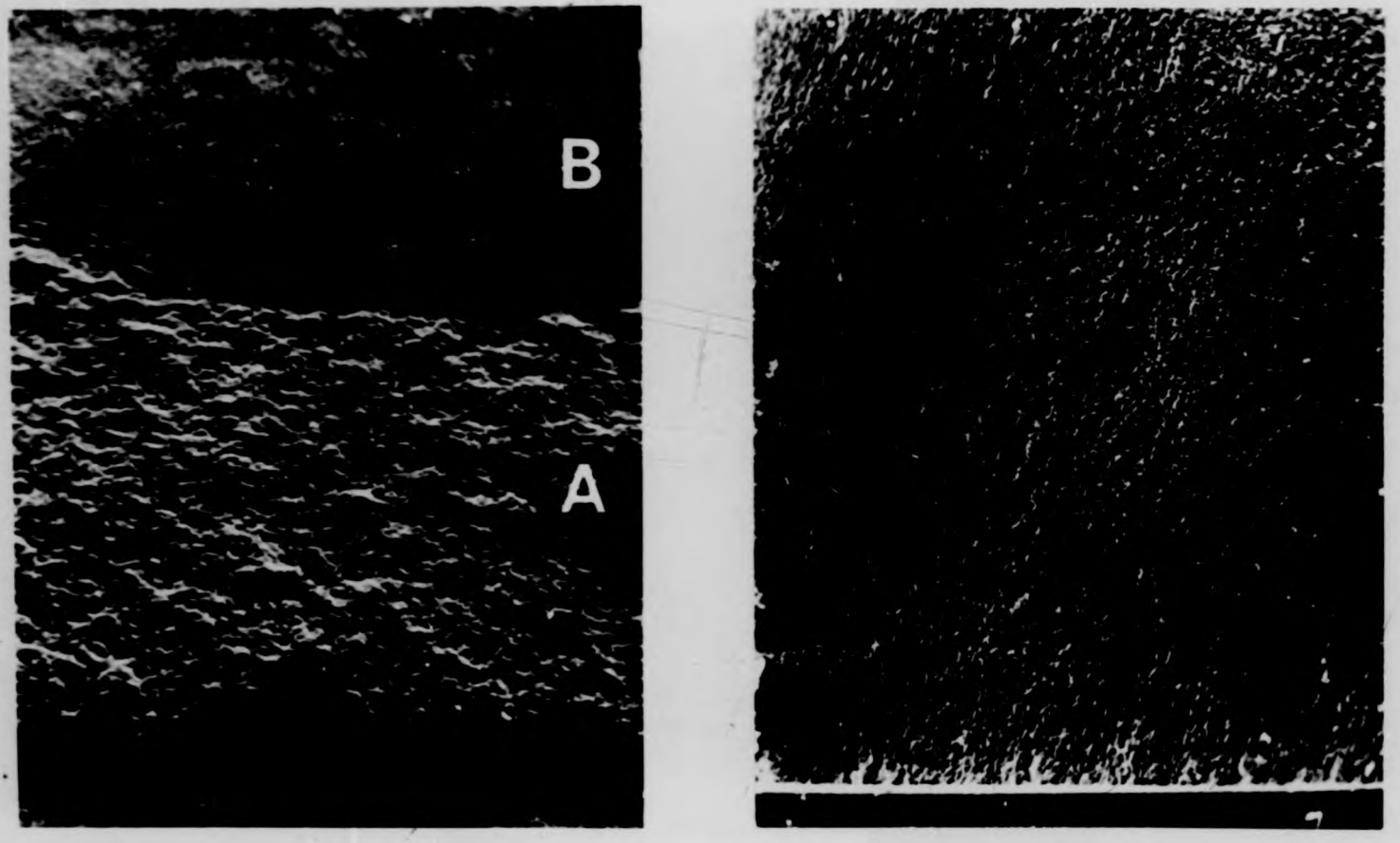

Fig. 6·6

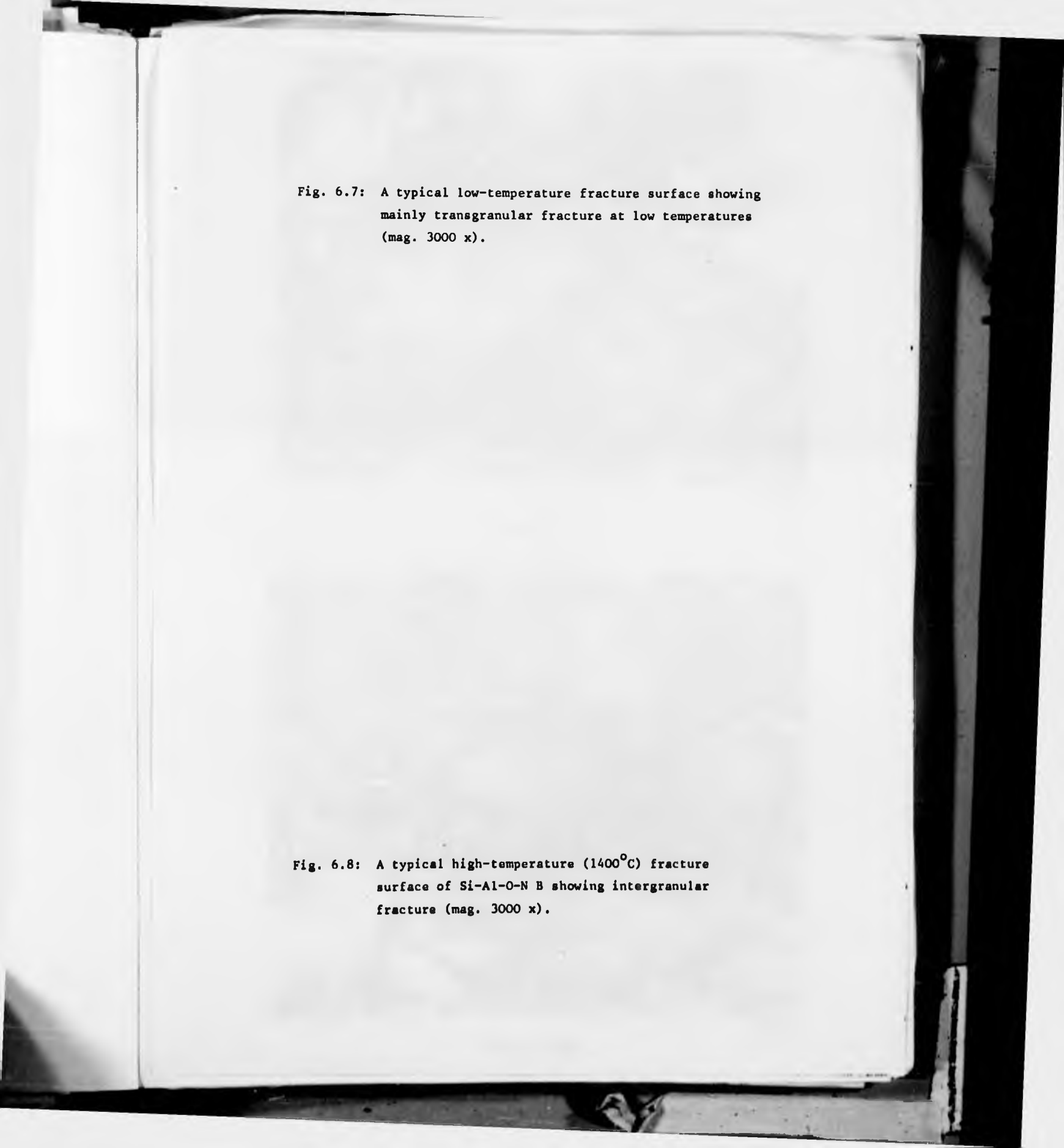

Fig. 6.7: A typical low-temperature fracture surface showing mainly transgranular fracture at low temperatures (mag. 3000 x).

Fig. 6.8: A typical high-temperature (1400^{o}C) fracture surface of Si-Al-O-N B showing intergranular fracture (mag. 3000 x).

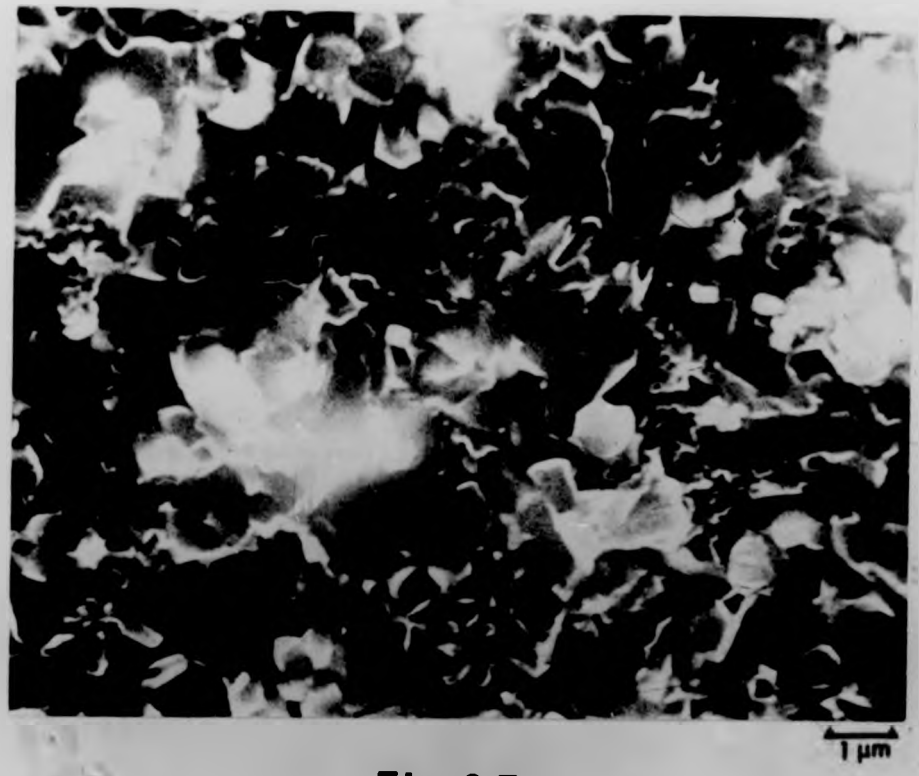

Fig. 6·7

Fig. 6·8

(10^{-10} - 10^{-2} ms^{-1}) and the appearance was similar to the slow crack growth region (A) in Fig. 6.6a. However, at low temperatures this extremely rough appearance was restricted only to the low velocity region (< 10^{-4} ms^{-1}) and in the higher velocity region the fracture surface was relatively smooth and similar to the fast crack growth region B in Fig. 6.6a. The change in gradient of the K_I-V plots at low temperatures appears to be associated with the topographical variation in fracture path. This is further evident from the comparison of double torsion fracture surfaces from specimens fractured at 1200°C with velocities $\sim 10^{-8}$ ms^{-1} and $\sim 10^{-3}$ ms^{-1} respectively (Fig. 6.9).

In ceramic C the fracture surfaces were relatively smooth for all crack velocities and temperatures in Fig. 6.1. Unlike ceramic B (or A), a small fraction of transgranular fracture was retained at high temperatures (1400°C) and showed a relatively small amount of grain pull-out during crack propagation (Fig. 6.10). There was no detectable topographical change in fracture path with increased velocity and this is consistent with the observation of a single slope in the K_I-V plots for this ceramic.

6.3. Mechanisms For Slow Crack Growth

The low stress exponent ($n \sim 7$) in the K_I-V relation and rough surface topography of the fracture surfaces of ceramic B are characteristic of a mechanism for slow crack growth via. inter-linkage of intergranular cavities, initiated by grain boundary sliding (Fig. 6.11a). This is supported by the observation of creep cavitation in ceramics A and B and the appearance of multiple cracks in bend specimens.

In ceramic C sub-critical crack growth is restricted to a narrow region of K_I which is characterised by the higher n value

Fig. 6.9: A double-torsion fracture surface of Si-Al-O-N B showing slow and fast fracture regions (1200°C).

Fig. 6.10: A high-temperature (1400°C) fracture surface of Si-Al-O-N C (mag. 3000 x).

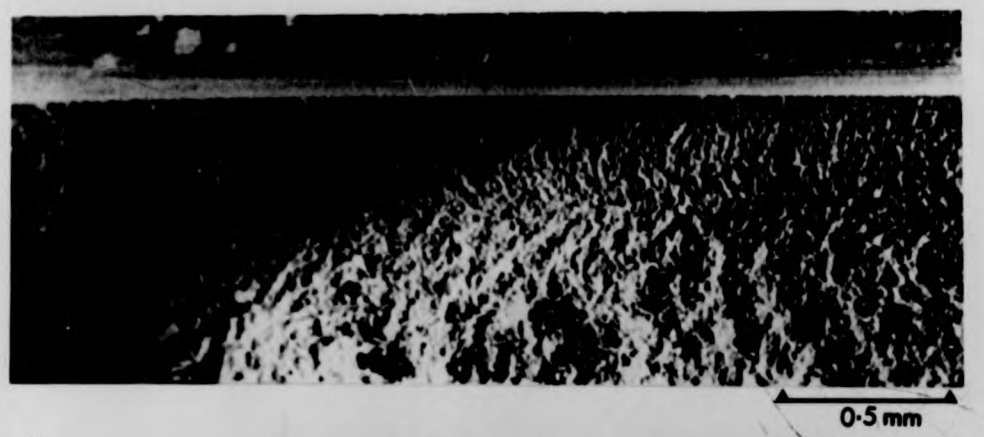

Fig.6·9

Fig.6·10

($n \sim 13$) and there is also a 'threshold' value of K_I below which cracks are 'blunted' via. diffusional creep. The fracture surface topography indicates that slow crack growth is due to the propagation of a single crack (Fig. 6.11b). The different behaviour in crack propagation of the two types of ceramic (A or B and C) is consistent with their creep behaviour. Slow crack growth mechanisms inferred from the K_I-V data and the microstructural observations of fracture surfaces of these Si-Al-O-N ceramics will be discussed below with a brief introductory review of cavity nucleation and growth mechanisms.

6.3.1. Cavity Nucleation and Growth Mechanisms

6.3.1. (a) Nucleation

The nucleation and subsequent growth mechanisms for cavities in metallic materials under creep conditions has been studied extensively by many workers and has been reviewed by Perry [179]. Greenwood et al [180] proposed that at high temperatures and low stresses cavities could nucleate and grow due to vacancy condensation on grain boundaries which experience a normal tensile stress. It was pointed out subsequently by Ballufi et al [181] and Machlin [182] that homogeneous nucleation by vacancies required a high vacancy supersaturation which could be considerably greater than that which normally occurs in metals under creep conditions. This is simply due to the fact that the applied tensile stress across the grain boundary, alone can not provide a sufficient potential gradient for cavity nucleation by vacancy condensation. Chen and Machlin [183] showed that any discontinuity on a grain boundary (e.g. ledges, triple junctions, second phase particles etc.) could act as a stress concentrator during grain boundary sliding. This stress concentration

Fig. 6.11: Schematic drawings of slow crack growth;
(a) via. interlinkage of intergranular cavities,
(b) due to a single crack,
(c) by coupled surface and grain boundary diffusion.

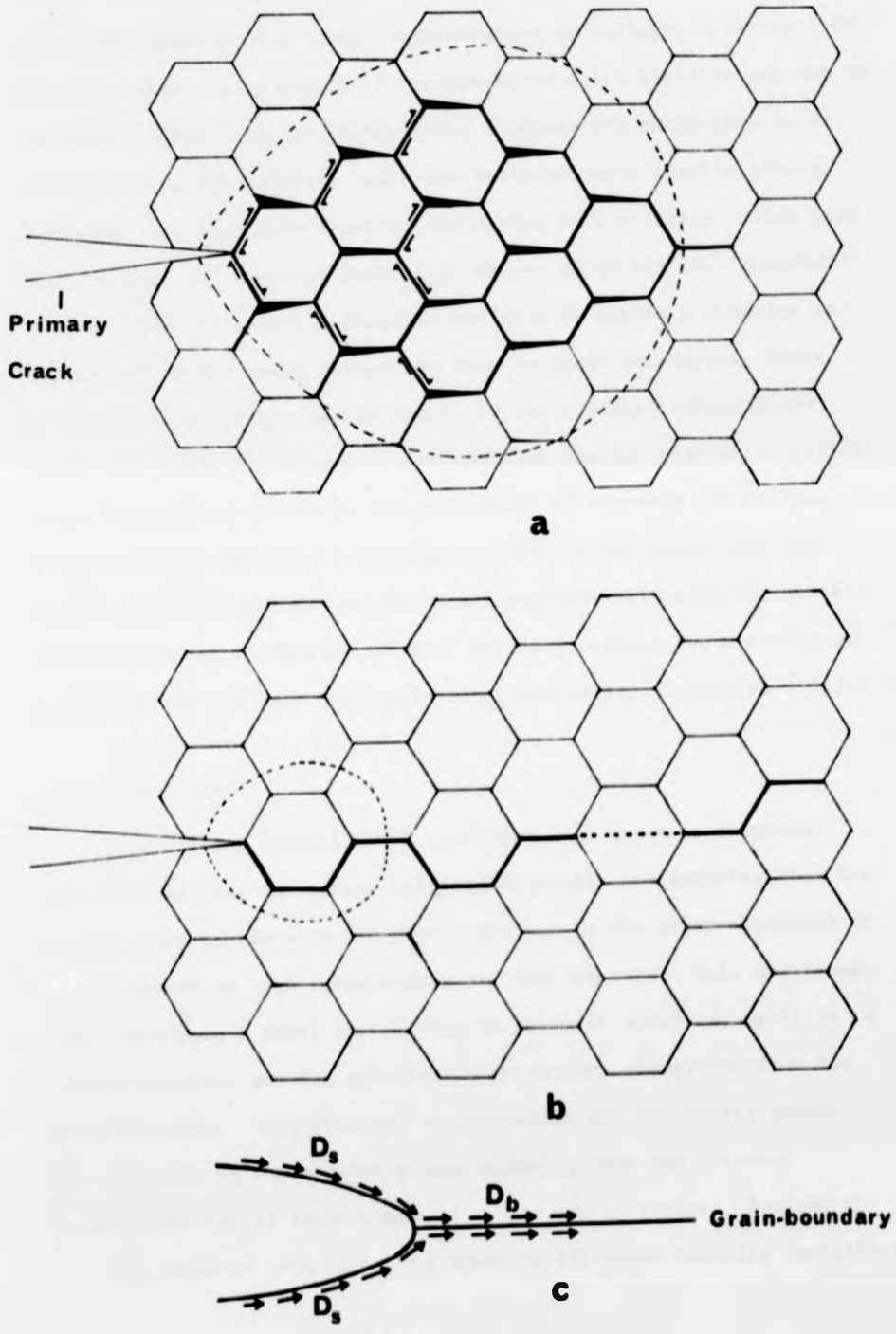

Fig. 6·11

could cause local rupture of atomic bonds [184] or increase the potential gradient for vacancy condensation to nucleate a cavity [185]. However, there is a 'threshold' stress below which cavities can not be nucleated [186]. Raj and Ashby [185] analysed the nucleation of a cavity in a grain boundary under the influence of a tensile stress assuming that vacancies cluster together to form a cavity. They used the concepts of classical nucleation theory to obtain the 'threshold' stress $\left(\frac{2\gamma_s}{r_c}\right)$ for cavity nucleation and also to obtain a relation for the steady state cavity nucleation rate in grain boundaries, where γ_s is the free surface energy and r_c is the critical radius below which the cavity is unstable. For cavities smaller than this critical size, the applied stress is not sufficient to overcome the surface tension forces and hence sintering occurs. It was shown that the steady state nucleation rate increases exponentially with the tensile stress and they further showed that triple junctions and second phase particles are the most favourable sites for cavity nucleation [185,187].

6.3.1. (b) Growth

Many workers [180,181,188] concluded from their experimental observations that the stress assisted diffusion of vacancies from the nearby grain boundary to the cavity surface is the major mechanism of cavity growth at high temperatures and low stresses. Hull and Rimmer [189] developed a model considering an array of spherical cavities in a grain boundary growing spherically by vacancy absorption from the adjacent grain. They obtained an expression for the cavity growth rate in terms of the applied stress assuming that the distance between cavities is large compared to the cavity radius. Speight et al [190] modified this theory by imposing different boundary conditions.

However Weertman [191] pointed out that Speight et al also used an improper boundary condition for their derivation and he made a further correction to the Hull-Rimmer equation showing that the average stress across the grain boundary must be equal to the applied stress. The modified equations [190,191] predict higher cavity growth rates than that of the Hull-Rimmer equation. However, in all these cases growth of a spherical cavity was considered rather than the growth of an elongated cavity which seems to be more realistic in view of experimental observations [192,193].

Raj and Ashby [185] analysed the growth kinetics of non-spherical cavities at different grain junctions and combined the nucleation and growth rates to obtain the time to fracture relations. A shape factor which depends on the nucleation site of cavities on the grain junctions and the surface tension forces of the interfaces, has been included in this analysis [185].

The above theories have been proposed to explain boundary cavitation in metallic materials which were presumed not to contain a grain boundary phase. However most of the structural ceramics (e.g. Hot-pressed Si_3N_4) contain a thin amorphous phase between the grain boundaries which acts as a viscous fluid at high temperatures.

6.3.1. (c) Materials with a Liquid Boundary Phase

The presence of this fluid layer at grain boundaries makes grain boundary sliding much easier than it would occur in a 'pure' grain boundary. If the grains do not deform plastically by dislocation motion or the diffusional processes are not fast enough to accommodate grain boundary sliding, wedge shaped cavities would form at the boundary junctions as proposed by Cottrell [186]. Kossowsky [87]

explained cavitation and failure mechanisms of hot-pressed Si_3N_4 using a similar model.

In an attempt to understand the deformation and fracture behaviour of polycrystalline materials with a liquid boundary phase Lange [194] and Raj and Dang [195] used an analysis based on theories of liquid adhesives. They suggested that the intergranular fracture of a polycrystal with a liquid boundary phase is analogous to fracture in an adhesive layer. Lange [194] and Raj [196] also showed that a 'threshold' stress is necessary to form a bubble in the liquid phase and is given by

$$\sigma_{th} = \frac{4\,\gamma_g}{h_o}$$

where γ_g is the surface energy of the glass phase and h_o is the thickness of the glass layer. Here it has been assumed [194] that the diameter of the bubble is equal to the thickness of the glass layer. However, more recently Raj [196] has shown that their previous adhesive layer model does not describe the failure mechanism in hot-pressed Si_3N_4. It has also been proposed that cavity nucleation and growth in the glass pockets at triple-junctions due to large tensile hydrostatic stress produced by grain boundary sliding is the rate controlling failure mechanism in this ceramic.

A model, based on grain boundary sliding has been proposed by Evans [116] in an attempt to describe the K_1-V relation for a Si_3N_4 ceramic containing intergranular residual glass. According to this model the crack growth rate at high K_1 levels ($K_1 \rightarrow K_{1c}$) is given by [116]

$$V = \frac{dk}{\delta_c} \left\{ \left(\frac{2\pi}{d}\right)^{\frac{1}{2}} f(\theta) \right\}^n K_1^n \qquad (6.1)$$

where δ_c is a critical sliding displacement, k is the proportionality constant and N(≈1) is the stress exponent in the sliding equation, d the grain size and $f(\theta)$ is an angular dependence of the shear stress near the crack tip. The rapid increase in K_{1c} in Si_3N_4 above a critical temperature was explained in terms of a crack 'blunting' effect via an increase in δ_c due to a decrease in the viscosity of the intergranular phase. However, the above equation does not provide a quantitative prediction of crack growth. In practice the K_I-exponent is much larger than unity ($n \sim 7$).

6.3.2. Cavity Nucleation and Crack Growth in Si-Al-O-N Ceramics

Microstructural study of ceramics A, B and C revealed no evidence for the presence of cavities in 'as hot-pressed' materials. The observation of cavitation in ceramic A and B under creep conditions indicates that they have nucleated and grown during creep deformation. This has been discussed in section 5.3 and it was concluded that cavities nucleate in triple-junction glass due to grain boundary sliding during creep. Grain boundary sliding could produce large tensile hydrostatic stresses in the triple junction glass [196] which is a viscous fluid at high temperatures and this stress could exceed the 'threshold' stress $\left(\frac{4\gamma_g}{h_o}\right)$ for cavity nucleation even under a low applied stress. The surface energy of the residual glass at triple junctions could be relatively small compared to that of a solid. Therefore, the 'threshold' stress for cavity nucleation in ceramics A and B is likely to be lower than that for ceramic C which does not contain triple junction glass. The faceted β'-liquid interface could also provide a surface of relatively low energy in these ceramics and cavity nucleation in these interfaces is highly probable. This is evident from the observed slow crack growth at low K_I levels and

creep cavitation at low stress levels. In the higher-velocity region grain boundary sliding seems to be sufficiently rapid to cause crack 'blunting' and this may increase the effective K_I level at the tip of the primary crack. The amount of grain boundary sliding increases with increasing temperature and gives rise to an increase in K_{Ic}-level with temperature and also to the reversal in temperature dependence at higher velocity region of K_I-V diagram (Fig. 6.1). These observations suggest that slow crack growth in ceramics A and B is due to inter-linkage of intergranular cavities initiated by grain boundary sliding as in hot-pressed Si_3N_4 [116]. Ceramic C contains no detectable triple junction glass and the relatively high surface energy results in a higher 'threshold' stress for cavity nucleation. This is supported by the observation of non-cavitating behaviour in creep deformation even at high stress levels and the suppression of slow crack growth up to a relatively high K_I level. At very high K_I levels cavities may nucleate and grow in grain boundaries by diffusional mechanisms. However, the nucleation and diffusion-controlled growth of cavities will be restricted to a more 'localised' stress field at the primary crack tip. This is evident from the less tortuous fracture path of ceramic C. It is also important to note that the brittle ceramics always contain inherent flaws (in the case of a crack propagation test a pre-initiated crack) which could grow by diffusional mechanisms and therefore the cavity nucleation stage may not be essential for crack propagation.

However, most of these models discussed previously (section 6.3.1) are based on cavity growth rather than crack propagation. In these models the 'time-to-failure' was obtained by calculating the time for inter-linkage of the grain boundary cavities. Hence it is difficult to compare the present data directly with most of these models because they do not predict the K_I-V relation. However, Stevens and Dutton [131]

and Dutton [197] have developed a model for high temperature crack propagation by diffusional processes and this model is based on a calculation of the total chemical potential of atoms at the crack tip and predicts that vacancies will be either attracted or repelled from a crack tip according to the magnitude of the applied stress (i.e. below a critical stress crack growth would not occur). In this model, propagation of a Griffith-type crack has been considered and hence the chemical potential of the atoms at the crack tip due to the strain field at the crack tip depends on the square of the applied stress. This has led to a $(\text{stress})^2$ dependence for crack growth by grain-boundary diffusion. This low K_I-exponent would not account for the crack growth behaviour of ceramic C. However a recent model for diffusive crack growth by Chuang [198] seems to have several features that describe the K_I-V data for ceramic C (for high crack velocities this model predicts $V \alpha K_I^{12}$ relation and also a 'threshold' K_I-value for rapid crack growth) and therefore the crack propagation data for ceramic C was compared with that predicted by this model.

6.3.3. Plain-strain Elastic Model of Chuang

This model [198] considers a semi-infinite grain-boundary crack growing in an infinite bi-crystal due to coupled surface and grain-boundary diffusion. The atoms removed by surface diffusion from the crack surface flow into the grain boundary ahead of the crack tip due to the gradient of chemical potential which arises from the varying curvature along the crack front (Fig. 6.11c). These atoms are further diffused away from the crack tip along the grain boundary due to grain boundary diffusion and a steady state flow of matter is maintained. Boundary transport is controlled by the tensile stress distribution along the interface ahead of the crack tip. This stress distribution is determined by the applied stress and misfit residual

stress induced by those atoms diffused from the crack surface. The crack front moves forward by this process without changing it s shape. It has been assumed [198] that the grain boundary ahead of the moving crack is perfect 'matter' sink and free surfaces and interfaces provide a higher diffusivity path for matter to migrate as compared to any path inside the grain.

According to this model, stress intensity (K_1) and crack velocity (V) are related by [198]

$$K_1 = A\, V^{1/12} + B\, V^{-1/12} \tag{6.2}$$

where $$A = 1.06 \sqrt{1 - \frac{\gamma_b}{2\gamma_s}} \left[\frac{(kT)^{1/12}\, \gamma_s^{2/3}}{D_s^{1/3}\, \Omega^{7/36}}\right]\left[\frac{E D_b \delta}{(1 - \nu^2)}\right]^{\frac{1}{4}}$$

and $$B = 1.42 \sqrt{1 - \frac{\gamma_b}{2\gamma_s}} \left[\frac{(D_s \gamma_s)^{1/3}\, \Omega^{7/36}}{(D_b \delta)^{\frac{1}{4}}\, (kT)^{1/12}}\right]\left[\frac{E}{(1 - \nu^2)}\right]^{3/4}$$

The 'threshold' K_1 value (K_{Cr}) and corresponding velocity (V_{Cr}) are given by [198]

$$K_{Cr} = 2(AB)^{\frac{1}{2}} = 2.45 \sqrt{\frac{E(\gamma_s - \gamma_{b/2})}{(1 - \nu^2)}} \tag{6.3}$$

and $$V_{Cr} = \left(\frac{B}{A}\right)^6 \tag{6.4}$$

where E = Young's modulus

ν = Poisson's ratio

$D_b\delta$ = Grain boundary diffusion coefficient x boundary width

D_s = Surface diffusion coefficient

Ω = Atomic volume

k = Boltzman constant

and T = Absolute temperature

Unfortunately for ceramic C some of these material parameters (γ_s, γ_b and D_s) are not available. However, using the values of known parameters, lower and upper limiting values of the unknown parameters were estimated by matching the calculated K_I-V data at lower K_I and upper K_I regions of the experimental curve as shown in fig. 6.12 (at 1400°C).

For ceramic C (at 1400°C)

$$D_b\delta \simeq 6 \times 10^{-25}\ m^3 s^{-1} \text{ (from creep data)}$$

$$E = 300\ G\ Nm^{-2}$$

$$\nu = 0.27$$

and $$\Omega \simeq 1.06 \times 10^{-29}\ m^3$$

The resulting values for γ_s and D_s (Fig. 6.12) are listed below (It is assumed that $\frac{\gamma_b}{\gamma_s} \simeq \frac{1}{2}$; this is the approximate ratio for many metallic materials).

Curve 1 : $\gamma_s \simeq 0.75\ Jm^{-2}$

$D_s \simeq 1 \times 10^{-17}\ m^2 s^{-1}$

Curve 2 : $\gamma_s \simeq 1.0\ Jm^{-2}$

$D_s \simeq 6 \times 10^{-18}\ m^2 s^{-1}$

Curve 3 : $\gamma_s = 0.75\ Jm^{-2}$

$D_s \simeq 2.5 \times 10^{-18}\ m^2 s^{-1}$

Curve 4 : $\gamma_s = 2.5\ Jm^{-2}$

$D_s \simeq 2.5 \times 10^{-17}\ m^2 s^{-1}$

Curve 3 shows the best fit to the experimental curve.

The K_I-V relation for curve 3 is

$$K_I = 4 \times 10^6\ V^{1/12} + 4.51 \times 10^4\ V^{-1/12} \qquad (6.5)$$

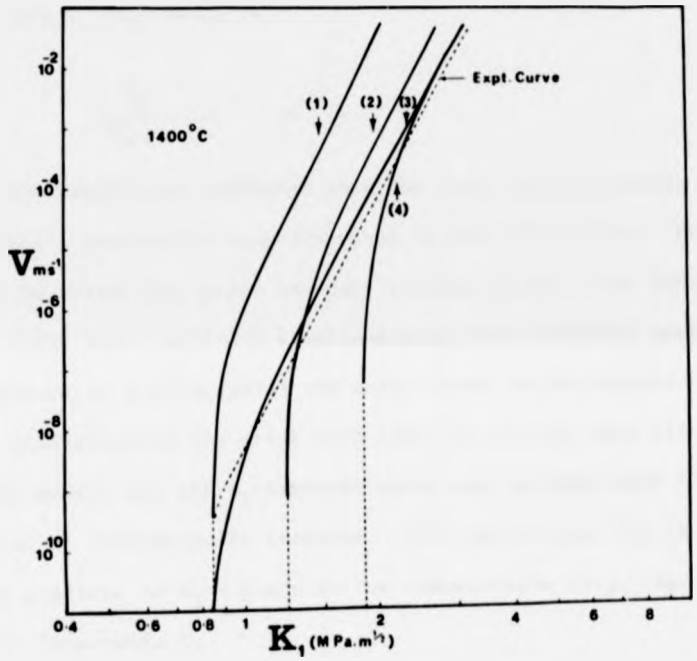

Fig. 6.12: A comparison of the K_I-V data for Si-Al-O-N C (at 1400°C) with that predicted by the diffusive crack growth model.

The values listed above seem to be reasonable compared to the published data for many metals and a few ceramics. E.g. Al_2O_3 (at 1850°C) $\gamma_s = 0.9\ Jm^{-2}$ [53] and in many metals the $\frac{\delta D_b}{D_s}$ ratio is about $10^{-6} - 10^{-9}$ m. In ceramic C this ratio is

$$\frac{\delta D_b}{D_s} \sim 10^{-7} - 10^{-8}\ m.$$

This comparison indicates that the crack growth process in ceramic C is possibly similar to that described by the above model. However it should be noted that grain boundary sliding which is not included in the above model also could act simultaneously with diffusive mechanisms. Furthermore, in a polycrystal the crack front could interact with other grain boundaries in the crack path (This is not the case with the bi-crystal model) and the K_I-exponent value may increase with the increased fraction of transgranular fracture. This may account for the increase in the gradient of K_I-V plots at low temperatures (e.g. Fig. 6.1 at 1200°C) in ceramic C.

The impurity segregation level affects the diffusion coefficients and also the $(2\gamma_s - \gamma_b)$ value which determine the 'threshold' K_I level (K_{Cr}) and the corresponding critical velocity. The ceramics containing relatively 'pure' grain boundaries (heat-treated ceramics B and C) have shown this effect and a further discussion related to this is reserved for chapter seven.

CHAPTER SEVEN

EVOLUTION OF IMPROVED Si-Al-O-N CERAMICS VIA. HEAT-TREATMENT

7.1 Introduction

The long-term non-steady-state creep behaviour and the variation in measured activation energy of ceramic C has been explained in terms of a progressive change in grain boundary structure via. the escape of segregated impurities into a surface oxide film (SiO_2). It has also been suggested that a similar effect may occur in the Mn-containing ceramic but the effect is not apparent due to the dominant influence of cavitation. These observations indicate that heat-treatment in an oxidising environment may result in improved Si-Al-O-N ceramics. This has motivated the exploration of high temperature creep and fracture properties of heat-treated specimens of both types of ceramic.

7.2. Heat-treatments

Ceramics B and C were heat-treated for $\sim$ 940 hours at $\sim$ 1430^{o}C in an air atmosphere either in the form of bend creep test bars, 3 mm x 3 mm cross-section or as 2 mm thick double-torsion test specimens. In determining heat-treatment times the extent of the non-steady-state creep period of ceramic C (> 150 hours) was used as a guide. The temperature was a compromise between the change occurring in reasonable time and specimen dissociation. The oxide layer was removed three times (after $\sim$ 200 hours intervals) during the heat-treatment to enhance impurity extraction from grain boundaries and triple junctions. After removing the final oxide layer, which was very thin compared to the original oxide layer, the specimens were polished using SiC papers

(600 grit) to maintain the same surface condition. It is also important to note that in double-torsion specimens the guide groove and the notch at one end of the groove was machined after heat-treatment.

As mentioned previously, de-segregation of grain-boundary impurities via. solution within β′ crystals could occur over a relatively short time since diffusion distances are << 1 μm (the β′ grain size). This mechanism is independent of a surface silica layer and should be observed in vacuum heat-treated or 'bulk' specimens. To study the relative response to this effect, the creep behaviour of specimens (3 mm x 3 mm cross-section bend specimens) cut from the centre of 'bulk' pressings (thickness > 10 mm) which were subjected to an identical heat-treatment (∿ 940 hours at ∿ 1430°C) was compared with that of the smaller specimens which had been heat-treated in an oxidising environment.

7.3. High Temperature Creep

7.3.1. Measurement of Creep Parameters

Creep tests were performed in four-point bending and results are summarized in Figs. 7.1 and 7.2. For comparison the creep data for 'as-received' ceramics are also included. In ceramic C (heat-treated) the non-steady-state behaviour is absent and stress dependence (Fig. 7.1) is linear ($n = 0.98 \pm 0.06$). Similar behaviour has been observed in 'as-received' specimens of ceramic C after long test times. The 'bulk' heat-treated ceramic C exhibited an intermediate creep behaviour ($n = 0.85 \pm 0.04$) with a small amount of transient creep. A similar behaviour is evident from the activation-energy plots of ceramic C (Fig. 7.2b). The activation energy approaches a limiting value of 818 ± 22 k J mol^{-1}, with heat-treatment.

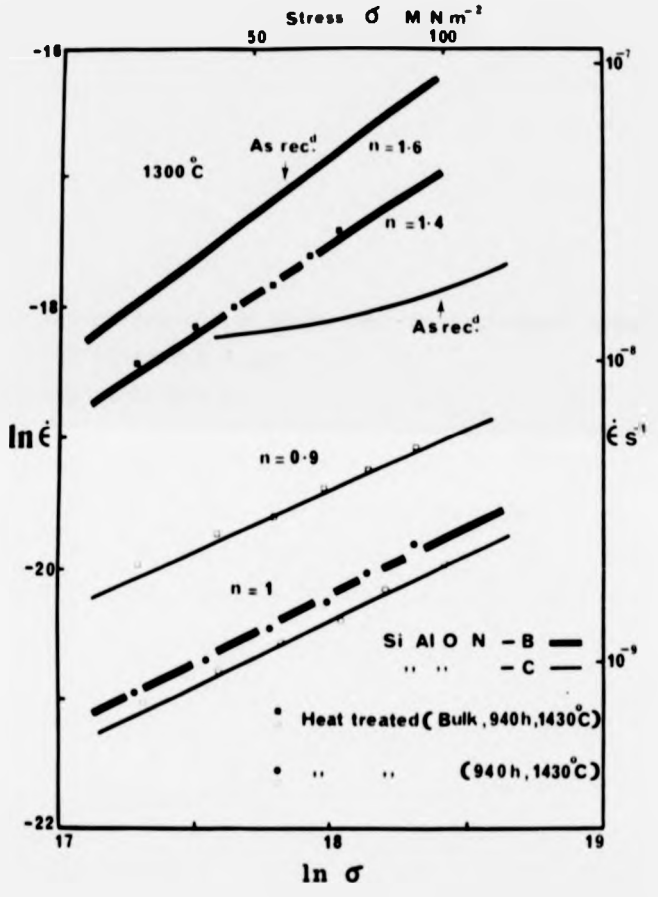

Fig. 7.1: Stress-exponent plots for 'heat-treated' Si-Al-O-Ns B and C.

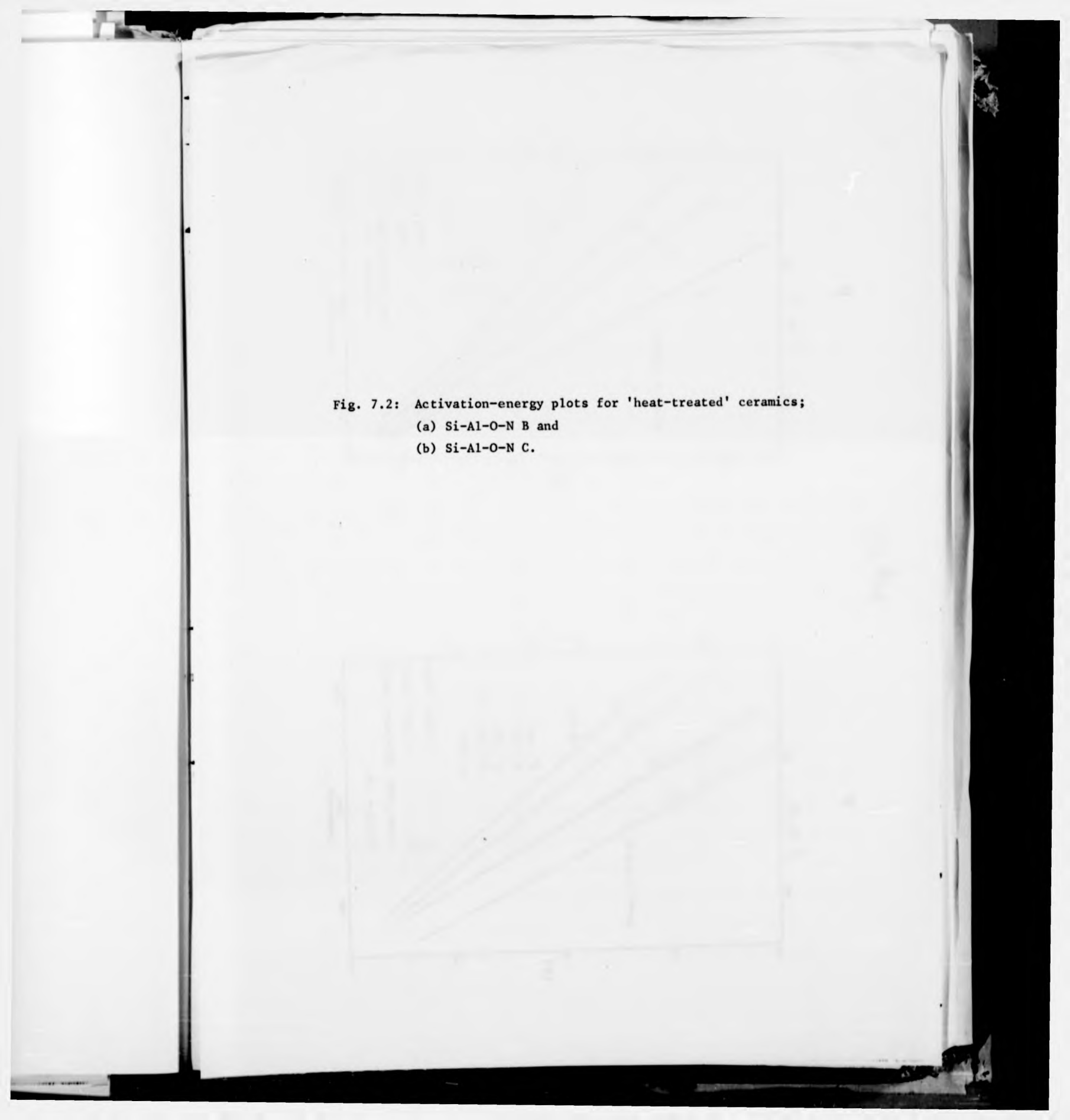

Fig. 7.2: Activation-energy plots for 'heat-treated' ceramics;
(a) Si-Al-O-N B and
(b) Si-Al-O-N C.

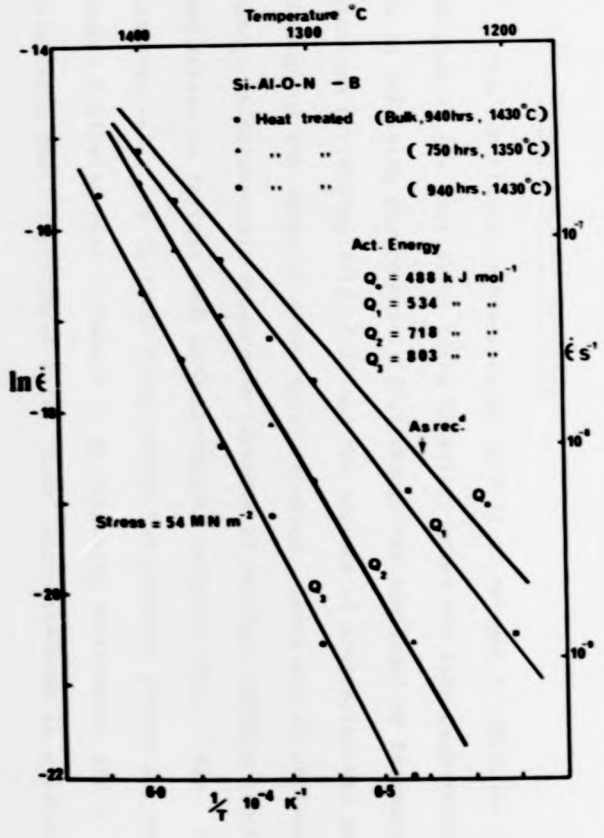
Temperature °C
1400
1300
1200
Si-Al-O-N – B
Heat treated (Bulk, 940hrs, 1430°C)
(750 hrs, 1350°C)
(940 hrs, 1430°C)
Act. Energy
Q_o = 488 k J mol^{-1}
Q_1 = 534 " "
Q_2 = 718 " "
Q_3 = 883 " "
As rec.d
Stress = 54 MN m^{-2}
Q_o
Q_1
Q_2
Q_3
ln $\dot{\epsilon}$
$\dot{\epsilon}$ S^{-1}
10^{-7}
10^{-8}
10^{-9}
-14
-18
-20
-22
6·0
6·5
$\frac{1}{T}$ 10^{-4} K^{-1}

a

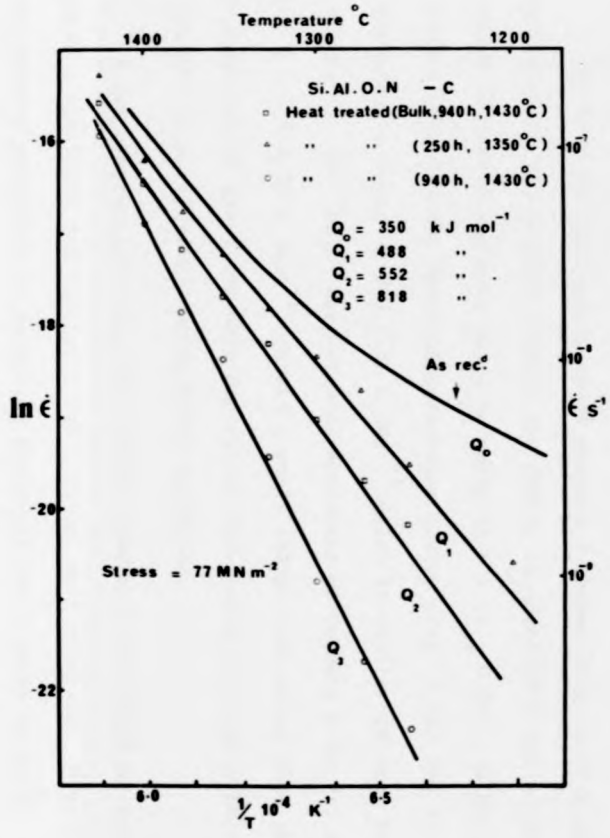
Temperature °C
1400
1300
1200
Si. Al. O. N – C
Heat treated (Bulk, 940 h, 1430°C)
(250 h, 1350°C)
(940 h, 1430°C)
Q_o = 350 k J mol^{-1}
Q_1 = 488 "
Q_2 = 552 "
Q_3 = 818 "
As rec.d
Stress = 77 MN m^{-2}
Q_o
Q_1
Q_2
Q_3
ln $\dot{\epsilon}$
$\dot{\epsilon}$ S^{-1}
10^{-7}
10^{-8}
10^{-9}
-16
-18
-20
-22
6·0
6·5
$\frac{1}{T}$ 10^{-4} K^{-1}

b

Fig. 7·2

The heat-treated specimens of ceramic B showed (Fig. 7.1) a dramatic reduction in creep rates (nearly two orders of magnitude) and a remarkable change in stress exponent value to unity ($n = 1.02 \pm 0.04$). Similar changes occur in the measured activation energy (Fig. 7.2a) and it approaches a value of 803 ± 21 k $Jmol^{-1}$ which is similar to that for ceramic C. The 'bulk' heat-treated specimens of Ceramic B ($n = 1.38 \pm 0.05$ and $Q = 534 \pm 10$ k $Jmol^{-1}$) showed a small change indicating that the de-segregation of grain boundary impurities via. solid solution within β' crystals is a relatively unimportant mechanism.

A few compression-creep experiments have been performed on heat treated specimens and similar n and Q values were obtained. However, the reduced precision in measuring extremely small creep rates of heat-treated samples in compression introduces a considerable experimental scatter. In both deformation modes the creep curves exhibited a negligible 'primary' creep after specimen heat-treatment probably due to the absence of a visco-elastic component on reduction in grain-boundary segregation.

7.3.2. Microstructural Analysis

The new stress exponent value ($n = 1$) of ceramic B indicates the absence of the cavitation creep behaviour after the long heat-treatment in an oxidising environment. This change was confirmed by transmission electron microscopy (Fig. 7.3) and the absence of cavitation was evident throughout the range of creep strain studied. There was an obvious change in macroscopic appearance (absence of multiple surface cracking) and strain to failure from un-heat-treated ceramics (Fig. 7.4a). The dramatic reduction in total creep strain (at constant stress for similar times) following heat-treatment in an oxidising environment and a relatively small improvement after 'bulk' heat-treatment is evident from

Fig. 7.3: T.E.M. showing non-cavitating behaviour of Si-Al-O-N B after heat-treatment (at 1400°C).

Fig. 7.4: A comparison between bend-creep specimens of 'as-received' and heat-treated Si-Al-O-N B.

Fig. 7·3

a

b

Fig. 7·4

fig. 7.4b. The appearance of surface cracking in the 'bulk' heat-treated specimen is an indication of a persistence of internal cavitation and this is consistent with the observed stress exponent value ($n \sim 1.4$).

The change in triple junction structure after the heat-treatment in an oxidising environment is responsible for the change in creep behaviour of ceramic B (Figs. 7.5a, 7.5b and 7.5c). There is no detectable triple junction glass in both the 'as heat-treated' and subsequently deformed state throughout the specimen width (3 mm).

A mechanism for elimination of triple junction glass involves the outward diffusion of impurity metallic ions (Mn, Mg and the accidental impurity Ca) into the surface oxide layer (SiO_2). The driving force for this outward diffusion is the metallic ion concentration difference between the oxide film and triple junction glass. The removal of metallic ions from the grain boundary glassy phase makes the remaining elements (O, Si etc.) more susceptible to crystallisation as β'. The presence of Al in both β' crystals and the silicate phase is an important factor in controlling the crystal solubility for oxygen. Hence O, Si etc. do not crystallise as a separate oxygen rich phase such as the oxynitride Si_2N_2O.

The observation of Mn-rich particles with a similar distribution and density, even in this non-cavitating state, confirms that cavity formation in the un-heat-treated ceramics is not associated with these particles.

Other than the change in triple junction structure, long heat-treatment has produced more random and curved boundary surfaces and also a measurable grain growth (the average grain size after the $\sim$ 1000 hour heat-treatment is 1.38 μm). Ceramic C also shows a similar grain

Fig. 7.5: T.E.M. showing the change in microstructure after 'heat-treatment' of Si-Al-O-N B.
(a) Before 'heat-treatment',
(b) and (c) After heat-treatment.

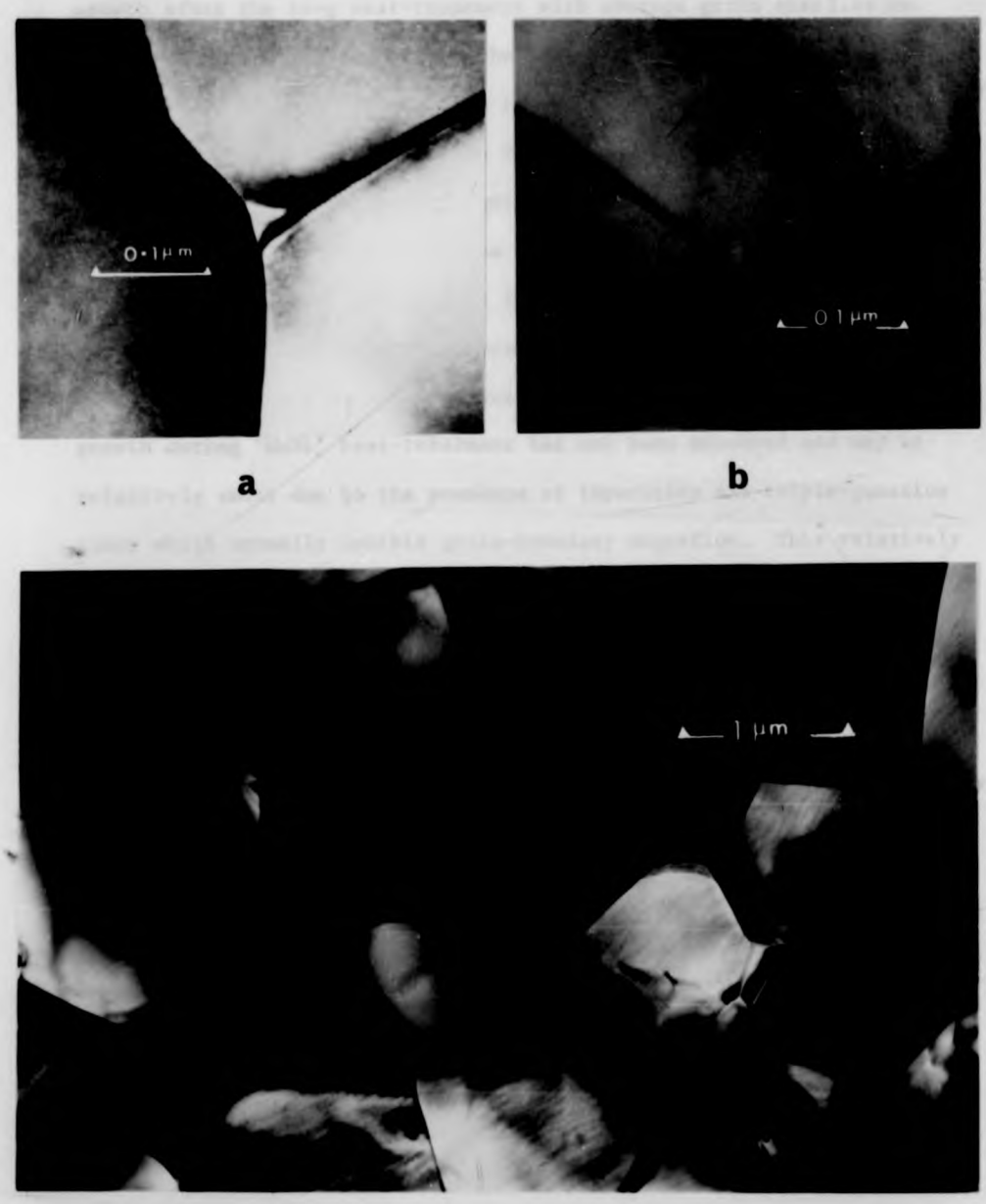

a b

c

Fig. 7·5

growth after the long heat-treatment with average grain size 1.44 μm. A comparison of grain size distribution between 'as-received' and heat-treated ceramics is shown in Figs. 7.6 and 7.7. This grain growth (∿ 15%) is partially responsible for the reduction in creep rates. For example, in ceramic B this contribution is about 15% (Coble creep is assumed) of the total reduction in creep rate (Fig. 7.1) the remainder being due to the change in triple junction and grain boundary structure. On this basis the improvement in the 'bulk' heat treated specimens, particularly in ceramics B, is very small. However, grain growth during 'bulk' heat-treatment has not been measured and may be relatively small due to the presence of impurities and triple-junction glass which normally inhibit grain-boundary migration. This relatively low reduction in creep rate together with the appearance of surface cracking and the stress exponent value n = 1.4 indicate that the secondary de-segregation mechanism is not applicable to the Mn-containing ceramic. In the case of ceramic C the contribution of this secondary mechanism may be responsible for part of the change in boundary structure. However, it is important to note that even the initial level of segregation in ceramic C (as-received) is relatively low compared to ceramic B and a small de-segregation of impurities may produce a more marked change in grain boundary structure. Furthermore, the possibility of long-range outward diffusion of grain boundary impurities into the oxide layer during the 'bulk' heat-treatment should not be excluded. A simple estimate, using an appropriate diffusion equation and diffusion coefficient for impurity ions of $\geq 10^{-12}$ m^2 s^{-1} shows that the impurity concentration could reduce to about half within a distance of 5 mm (the bulk specimen ½ width) within 1000 hours.

Fig. 7.6: Grain size distribution of Si-Al-O-N B before and after 'heat-treatment'.

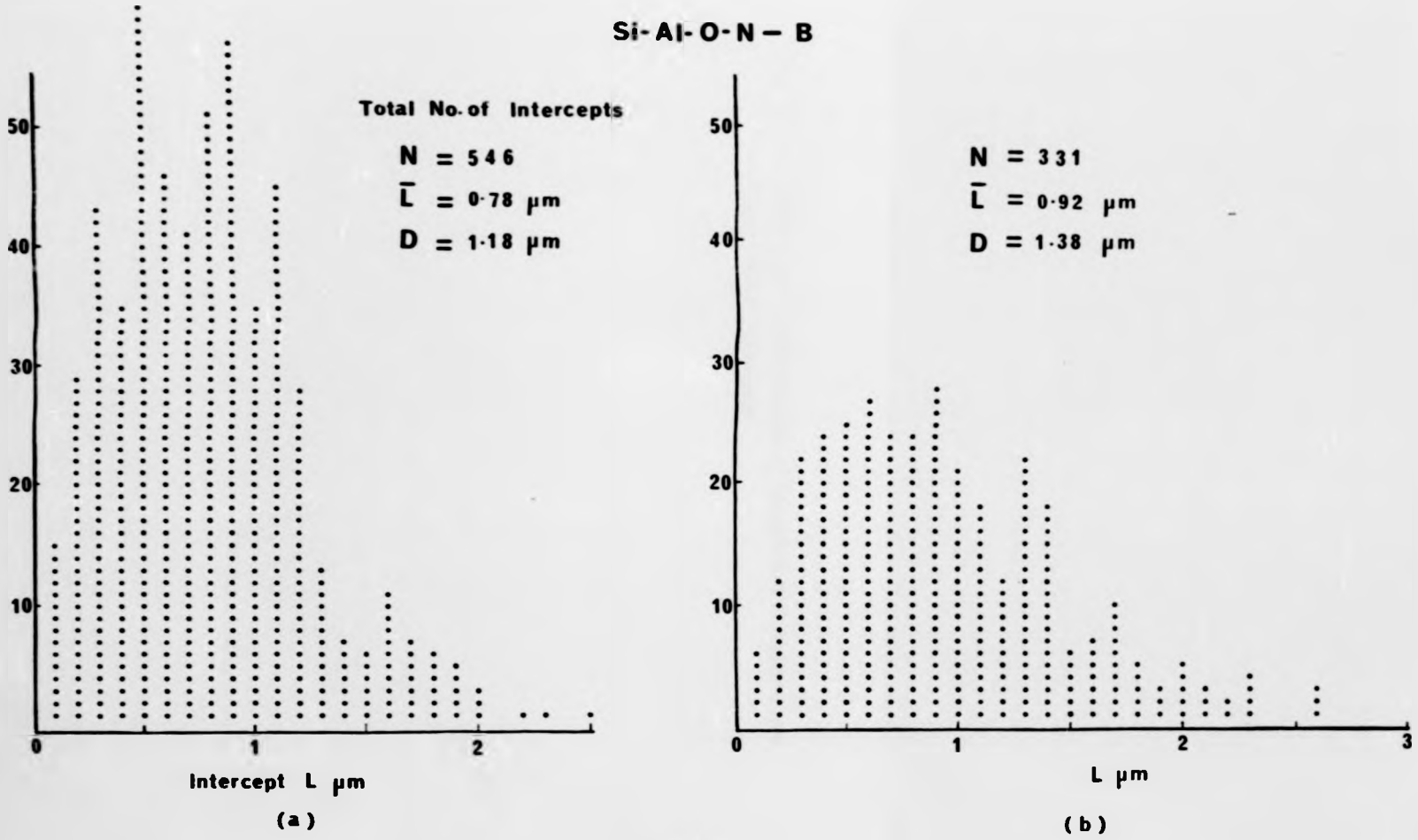
Si-Al-O-N – B
Total No. of Intercepts
N = 546
L̄ = 0·78 μm
D = 1·18 μm
N = 331
L̄ = 0·92 μm
D = 1·38 μm
Intercept L μm
L μm
(a)
(b)

Fig. 7·6

Fig. 7.7: Grain size distribution of Si-Al-O-N C before and after 'heat-treatment'.

Si-Al-O-N – C

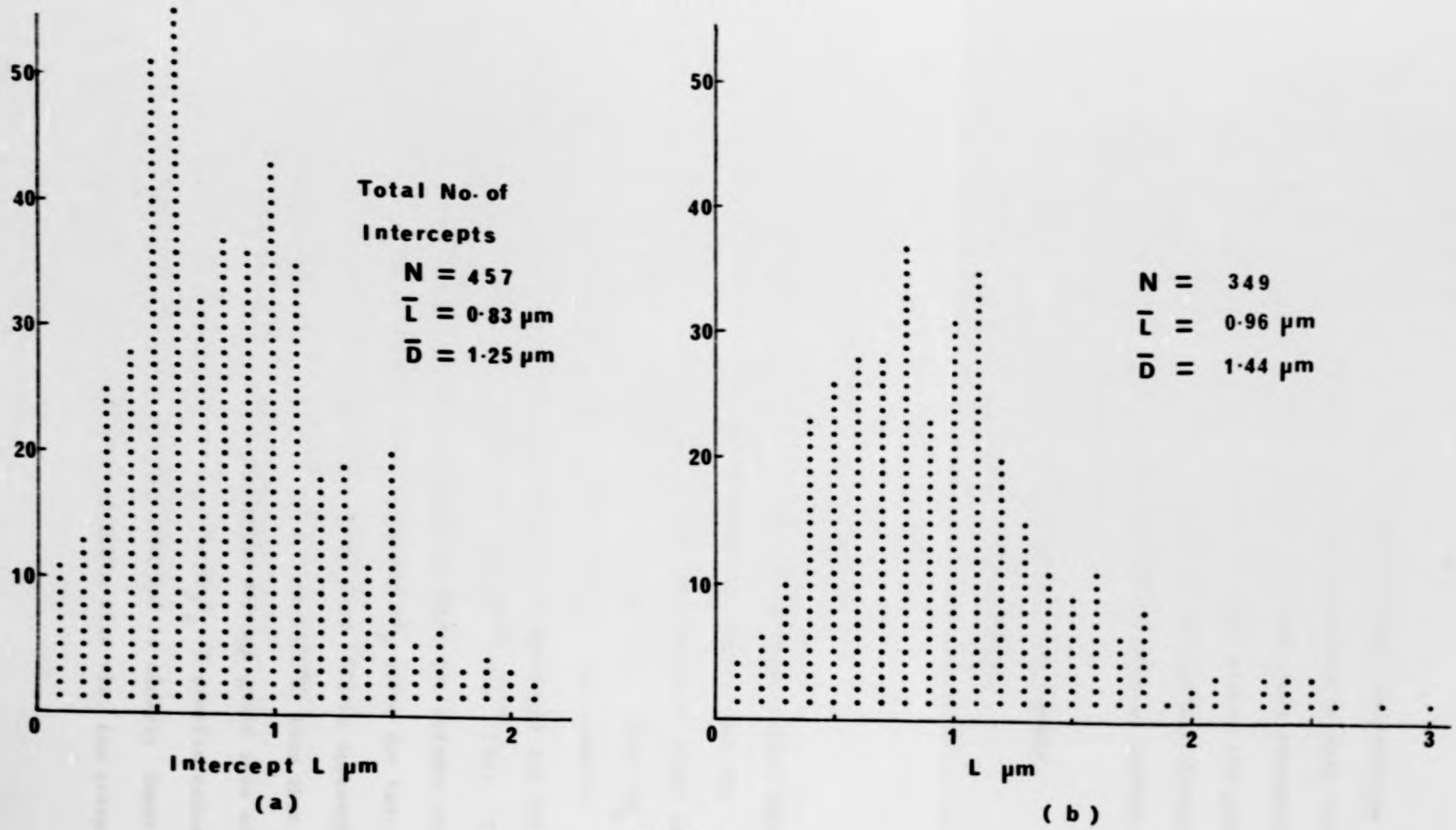

Fig. 7·7

7.3.3. Creep Mechanisms

The modified creep parameters and microstructural observations confirm that the creep mechanism is diffusion-controlled in both ceramics after heat-treatment. The removal of impurities from grain boundaries may increase the density of primary bonds (Si-N type) across the grain boundaries. Therefore diffusion of β′ crystal atomic species through this type of grain boundary would be more difficult, with an increased activation energy and hence lower creep rate.

Using new values for creep rate and grain size, δD_b values appropriate to this type of boundary have been estimated:

$\delta D_b = 3 \times 10^{-26}\ m^3\ s^{-1}$ (1375°C for ceramic C)

$\delta D_b = 6 \times 10^{-26}\ m^3\ s^{-1}$ (1375°C for ceramic B)

The previous δD_b value (section 5.3) for the un-heat-treated ceramic C at 1375°C is approximately one order of magnitude higher than the present value. (The value corresponding to the 'as-received' state is probably even higher than that calculated in section 5.3). These δD_b values are low compared with those for oxide ceramics. For example, δD_b at 1375°C for Al_2O_3 (Al boundary diffusivity, in MgO-doped and for some undoped materials, from creep data) is $\sim 4 \times 10^{-23}\ m^3 s^{-1}$ [44]. This difference is not surprising because the bonds in these two ceramic crystals have different degrees of covalency. The estimated δD_b value for hot-pressed Si_3N_4 (HS 130) based on compressive creep data [83] is approximately one order of magnitude higher ($\sim 2 \times 10^{-25}\ m^3\ s^{-1}$ at 1375°C) than that for the heat-treated β′ ceramics. An approximate average grain size of 1 μm has been used in the calculation of δD_b for Si_3N_4 (A precise value for average grain size has not been reported [83] but is clearly important because the value of δD_b is very sensitive to grain size via. the creep

equation $\dot{\varepsilon} = \dfrac{14\pi\sigma\Omega\delta D_b}{k\ T\ d^3}$.

Assuming that the measured activation energy for creep deformation is that for grain boundary diffusion, an equation for grain boundary diffusion can be obtained. For ceramic C, δD_b is given by

$$\delta D_b = 2.4 \exp - \frac{818\ k\ Jmol^{-1}}{RT} \quad m^3\ s^{-1}$$

and for ceramic B

$$\delta D_b = 1.5 \exp - \frac{803\ k\ Jmol^{-1}}{RT} \quad m^3\ s^{-1}$$

The pre-exponential term $\left(\delta D_{o_b}\right)$ is very high compared to that for the 'un-heat-treated' ceramic C ($\sim 1 \times 10^{-6}\ m^3\ s^{-1}$) and also to that for many other ceramics. For Al_2O_3 ($Q \simeq 420\ k\ Jmol^{-1}$) δD_{o_b} is $\sim 8 \times 10^{-10}\ m^3\ s^{-1}$ [44] and the estimated value for hot-pressed Si_3N_4 is $\sim 5 \times 10^{-3}\ m^3\ s^{-1}$ ($Q \simeq 705\ k\ Jmol^{-1}$ [83]). However, the δD_{o_b} value (the intercept of the log δD_b vs $\frac{1}{T}$ graph) is very sensitive to the value of the activation energy (Q) and normally high values are associated with high activation energies (a small error in Q will also result in a very large error in δD_{o_b}).

The grain boundary width, δ may decrease with de-segregation of impurity atoms from grain boundaries during heat-treatment. However, this effect is negligible compared to the very large increase in δD_{o_b}. This implies a change in D_{o_b} from $\sim 10^3\ m^2\ s^{-1}$ to $\sim 10^9\ m^2\ s^{-1}$ (assumed $\delta \sim 7$ Å). Although this increase is unusually high, the sense of the change appears to be correct. As a parallel process one could consider the transition from a grain boundary diffusion to a lattice diffusion. Normally, this transition is accompanied by an increase in activation energy and D_o value. For example, in Al_2O_3

$D_{o_b} \sim 8 \times 10^{-2}$ m^2 s^{-1} ($\delta \sim 100$ Å [44]) and $D_{o_\ell} \sim 14$ m^2 s^{-1} (D_{o_ℓ} is the D_o value for lattice diffusion and $Q \sim 580$ k Jmol^{-1}).

The D_o value for lattice diffusion (D_{o_ℓ}) is given by [199]

$$D_{o_\ell} \sim \frac{1}{6} \lambda^2 \nu e^{S/R}$$

where λ is the jump distance, ν the vibrational frequency of atoms, S the entropy term and R the gas constant. The pre-exponential part is normally $\sim 10^{-6}$ m^2 s^{-1}. The entropy term S may be related to the activation energy Q by [199]

$$S \propto \beta \frac{Q}{T_m}$$

where T_m is the absolute melting temperature and β is a parameter that depends on the temperature coefficient of elastic constants and is normally a small positive number [199] (for metals $\beta \sim 0.2 - 0.5$). This expression shows that the entropy term (and hence D_o) increases with activation energy. The vibrational frequency, ν of interfacial atoms could also increase due to the increase in local elastic properties of grain boundaries after heat-treatment. However, the increase in ν could be relatively small compared to the very large increase in D_{o_b}. Similarly, the change in λ after heat-treatment is expected to be small. Therefore, if a similar relationship is assumed for D_{o_b} the higher D_{o_b} value is mainly due to the entropy contribution and the observed increase in D_{o_b} with heat-treatment is due to the change in the grain boundary structure. It is believed that in heat-treated ceramics the density of primary bonds across the grain-boundary is relatively high and the higher activation energy is associated with their elastic distortion during atom transport which increases the entropy contribution.

7.4. Slow Crack Growth

7.4.1. K_I-V Data

K_I-V data for heat-treated ceramics B and C is shown in Fig. 7.8 For comparison, data at 1400°C for 'as-received' ceramics (A and B)is also included. The increase in gradient ($n \sim 17$) and introduction of a crack stabilising effect for ceramic B is consistent with the absence of creep cavitation. As in ceramic C this suppression of slow crack growth below a critical level (K_I = 2.1 $MPam^{\frac{1}{2}}$) is accompanied by visible evidence for crack blunting via. diffusional creep (Fig. 7.9). Ceramic C shows an increase in gradient ($n \sim 40$) and a shift in threshold value of K_I for crack stability. Slow crack growth is restricted to a very narrow range of K_I values. The measured activation energies for slow crack growth for ceramics B and C are $\sim$ 1000 k $Jmol^{-1}$ and $\sim$ 950 k $Jmol^{-1}$ respectively. These values are higher than obtained for creep deformation.

There is little change in the level of fracture toughness (K_{Ic}) which shows a reasonable agreement with that determined independently using SENB tests (Fig. 7.10).

In Fig. 7.11 a comparison is made between 'as-received' and heat-treated Si-Al-O-N ceramics together with the published data for commercial Si_3N_4 [129] and SiC [115] ceramics. Both heat-treated ceramics exhibit higher resistance to subcritical crack growth than that of Si_3N_4.

7.4.2. Mechanisms for Slow Crack Growth

7.4.2. (a) Diffusive Crack Growth

The main feature of the K_I-V relation in heat-treated ceramics is the increase in slope and 'threshold' K_I level. There is a marked change in fracture surface topography in heat-treated ceramic B. The fracture surfaces are macroscopically flat, deviating only a few grain diameters

Fig. 7.8: The K_I-V diagram for heat-treated ceramics.

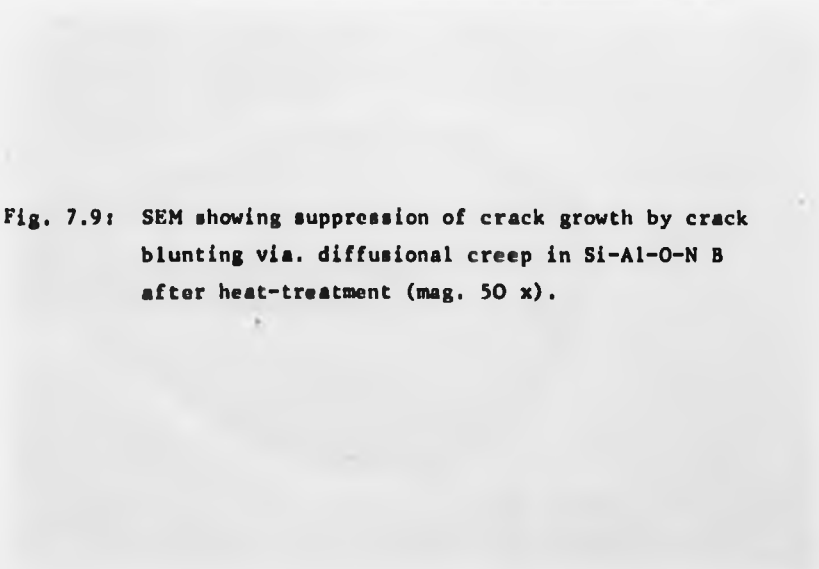

Fig. 7.9: SEM showing suppression of crack growth by crack blunting via. diffusional creep in Si-Al-O-N B after heat-treatment (mag. 50 x).

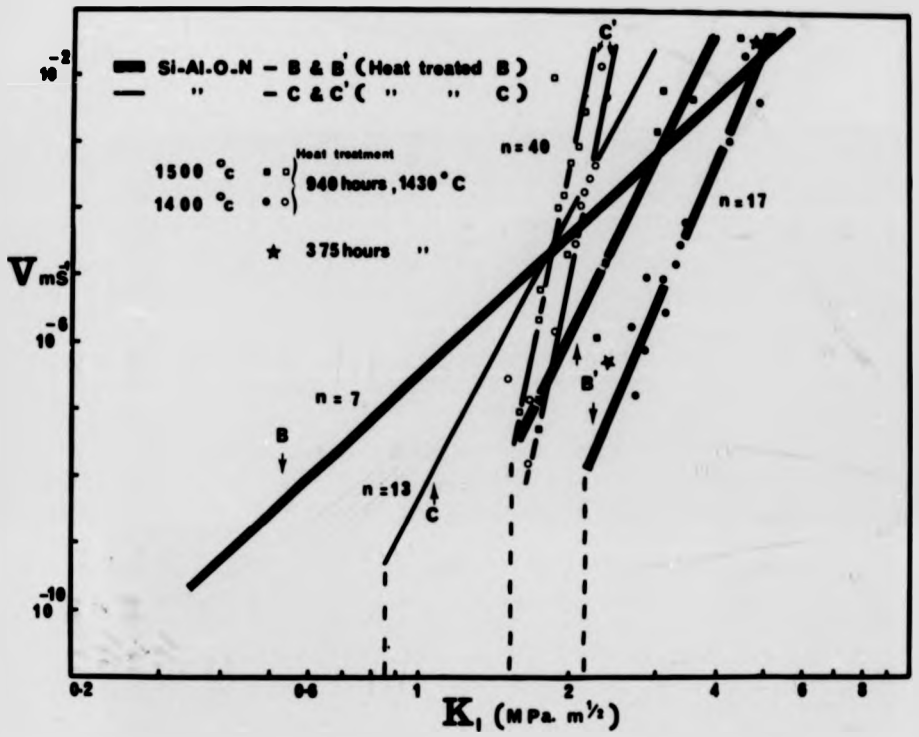
Si-Al-O-N – B & B' (Heat treated B)
" – C & C' (" " C)
Heat treatment
1500 °C
1400 °C
940 hours, 1430 °C
375 hours
n = 40
n = 17
n = 7
n = 13
B
B'
C
C'
V m/s
K_I (MPa. m^1/2)

Fig. 7·8


0·2 mm

Fig. 7·9

Fig. 7.10: The variation in K_{1c} with temperature after heat-treatment in Si-Al-O-Ns B and C.

Fig. 7.11: A comparison of K_I-V relationships for heat-treated and 'as-received' ceramics together with commercial Si_3N_4 and SiC.

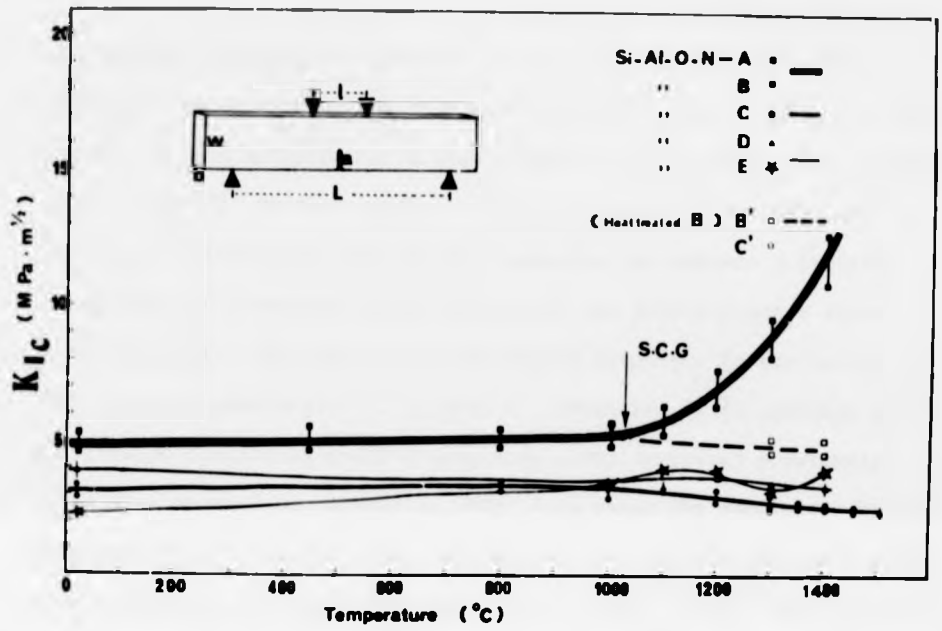

Fig. 7·10

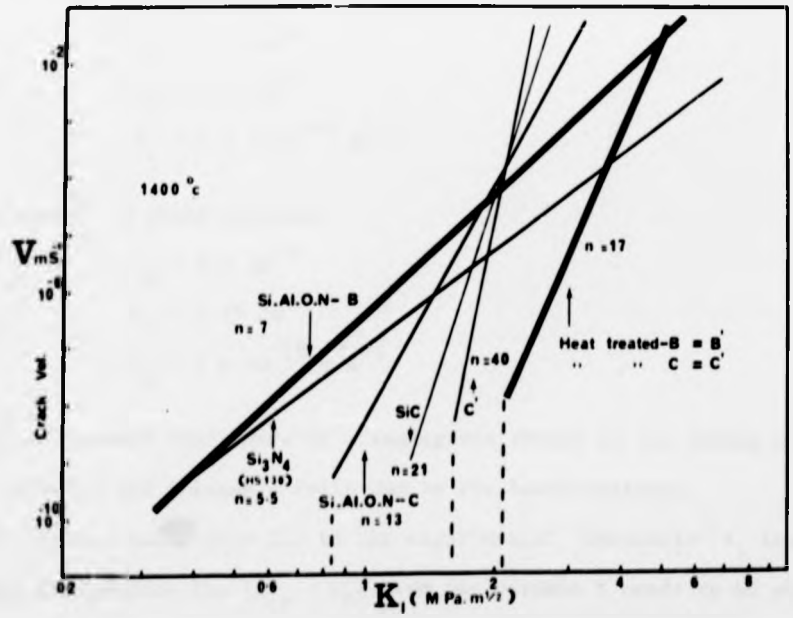

Fig. 7·11

from the mean fracture plane with no visible difference between slow and fast regions, unlike the 'as-received' state (Fig. 7.12). The other feature is the retention of a high proportion of transgranular fracture (even at 1500°C) in fast fracture surfaces (Fig. 7.13). These microstructural observations and the K_I-V relation for ceramic B indicate the absence of a viscous cavity nucleation and growth process after heat-treatment. This new slow crack growth behaviour is similar to that observed previously for ceramic C. Therefore it is possible that a diffusion-controlled crack propagation [198] described previously could also operate in ceramic B. Fig. 7.14 shows the comparison between experimental K_I-V data and that obtained from the diffusive crack growth model using new δD_b values at 1400°C ($\sim 1.3 \times 10^{-25}$ $m^3 s^{-1}$ and $\sim 8 \times 10^{-26}$ $m^3 s^{-1}$ for ceramics B and C respectively). The unknown parameters D_s and γ_s were estimated by matching the calculated and experimental curves as previously described (section 6.3.3):

For ceramic B (heat-treated)

$$\gamma_s = 3.2 \text{ Jm}^{-2}$$
$$\gamma_b = 1.6 \text{ Jm}^{-2}$$
$$D_s = 2.5 \times 10^{-18} \text{ m}^2\text{s}^{-1}$$

and for ceramic C (heat-treated)

$$\gamma_s = 1.5 \text{ Jm}^{-2}$$
$$\gamma_b = 0.75 \text{ Jm}^{-2}$$
$$D_s = 1 \times 10^{-18} \text{ m}^2\text{s}^{-1}$$

It is assumed that there is a negligible change in the values of Young's modulus and Poisson's ratio due to the heat-treatment.

To obtain a reasonable fit to the experimental 'threshold' K_I level for crack propagation the $(2\gamma_s - \gamma_b)$ term for ceramic B needs to be about

Fig. 7.12: A comparison of high-temperature (1400°C) fracture surfaces for Si-Al-O-N B before and after heat-treatment (mag. 20 x).

Fig. 7.13: Typical high-temperature fracture surface after heat-treatment showing an increase in the amount of transgranular fracture for Si-Al-O-N B.

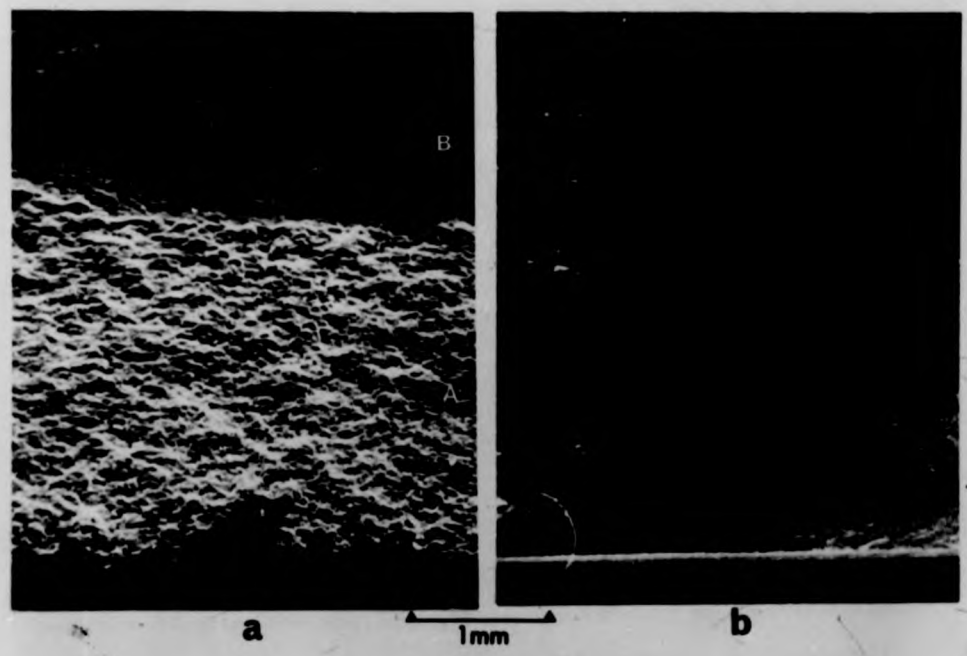

Fig. 7·12

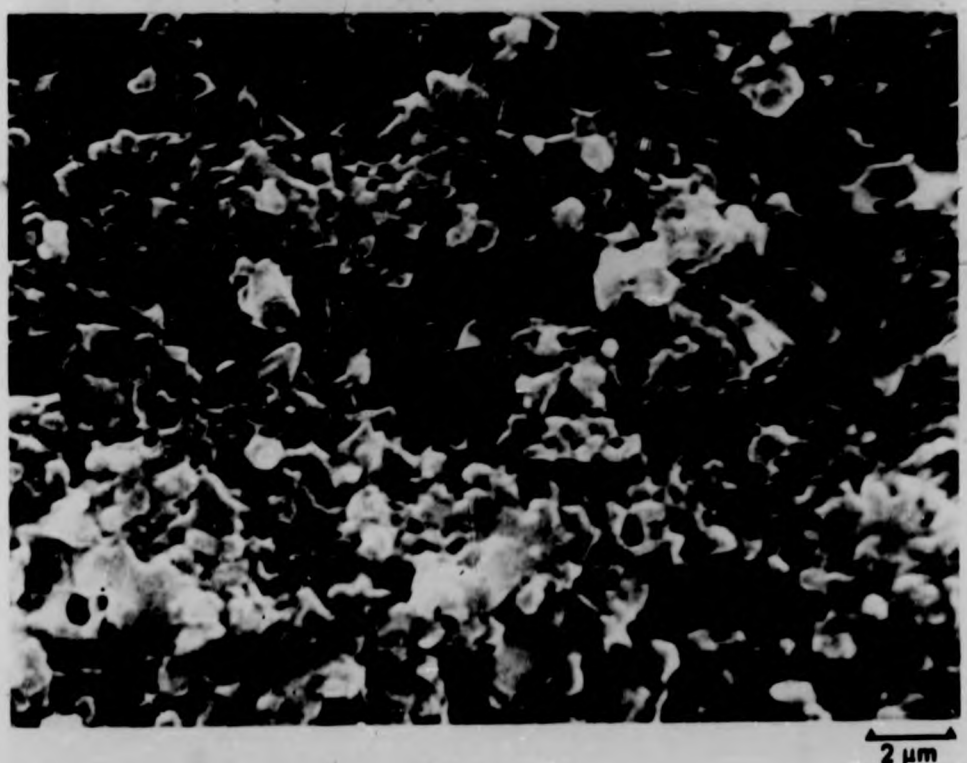

Fig. 7·13

twice of that for ceramic C. Also the estimated $(2\gamma_s - \gamma_b)$ value for ceramic C after the heat-treatment is nearly twice that for the 'as-hot-pressed' state. Hence if diffusive crack growth [198] is the dominant mechanism operating in these ceramics the variation of γ_s and γ_b with reduced impurity level should show a divergence. The $\frac{\delta D_b}{D_s}$ ratio ($\sim 10^{-7}$ m) for ceramic B appears to be reasonable, compared with that for the other materials.

The K_I-V relation for ceramic B based on the diffusive crack growth model, shows a moderate agreement (Fig. 7.14) throughout the velocity range. If the exact experimental points on the K_I-V diagram (Fig. 7.8) are considered the agreement with this model is more favourable. It is important to note that the experimental data points may not necessarily represent a straight line logarithmic K_I-V relation, but a curve with a large radius of curvature. In ceramic C the gradient of the K_I-V relation is considerably higher ($\sim$ 40) and therefore the predicted curve is deviated away from the experimental curve (Fig. 7.14) whatever reasonable values are used for the unknown variables (γ_s, γ_b and D_s). Even if the same argument is used as for ceramic B the diffusive crack growth model may be valid only for a small range of velocities.

Furthermore, the difference in activation energies for crack growth and that for diffusional creep adds an additional difficulty in rationalising the diffusive crack growth process in these ceramics. However, the activation energy value obtained from the K_I-V relation is not very accurate. These disagreements in theory and experimental data may be due to the operation of a different mechanism in these ceramics.

Before considering an alternative mechanism it is worth discussing two additional points related to Chuang's crack growth model [198]. Below the critical K_I level (K_{cr}), or for $V < V_{cr}$ (see section 6.3.3) the crack growth equation (equation 6.2) related to this model predicts a decrease in crack velocity with an increase in K_I and therefore this

Fig. 7.14: A comparison of K_I-V data for heat-treated ceramics with that predicted by the diffusive crack growth model.

Fig. 7.15: A comparison of K_I-V data for heat-treated ceramics and 'as-received' ceramic C with that predicted by thermally-activated bond breaking.

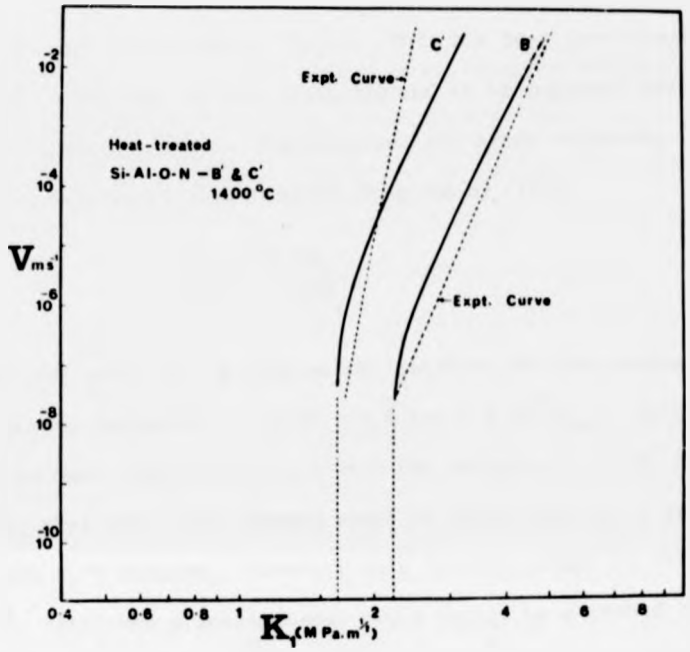

Fig. 7·14

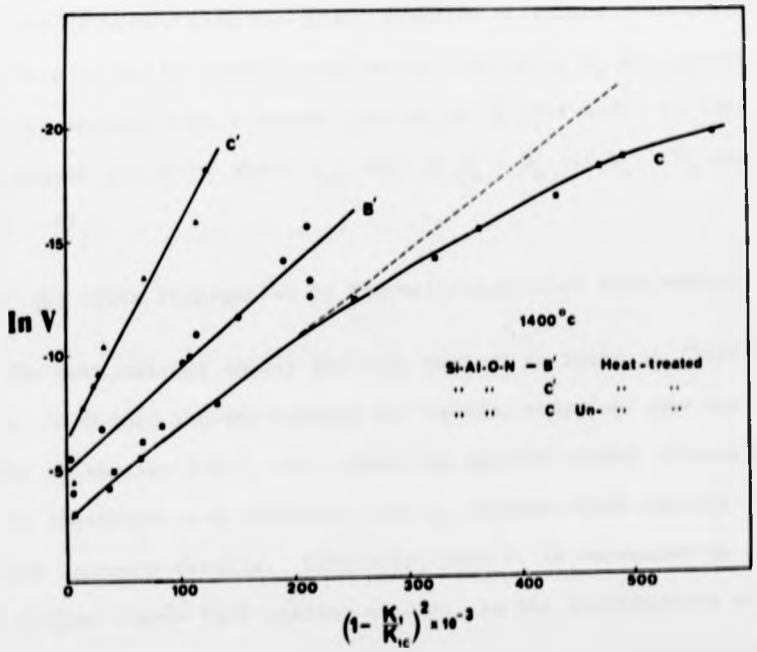

Fig. 7·15

model breaks down below the K_{cr} level. This has been interpreted [198] as an excess 'blunting' of the crack tip and it is supposed that it presents an unstable crack-tip shape. Furthermore, the crack thickness (ω) predicted by this crack growth model is given by [198]

$$\omega \simeq \left(\frac{V_{cr}}{V}\right)^{1/3} \frac{\delta D_b}{2OD_s}$$

Hence for $\frac{\delta D_b}{D_s} \sim 10^{-7}$ m (The values obtained for the present materials) the thickness ω approaches a value ~ 5 Å for $V \simeq 10^3 V_{cr}$. In other words the crack becomes atomically sharp when the velocity is $\sim 10^3 V_{cr}$. It is possible that this crack growth model is valid only for a small velocity range of the K_I-V diagram. However, this velocity range is very sensitive to the $\frac{\delta D_b}{D_s}$ ratio and a small change could result in a marked change in the velocity range (e.g if $\frac{\delta D_b}{D_s} \sim 10^{-6}$ m, $V = 10^6 V_{cr}$ for $\omega = 5$ Å). In addition, the predicted D_s values for these ceramics are lower than the D_b values at 1400°C if a reasonable δ value (~ 10 Å) is assumed. The experimental D_s and D_b values for metallic materials show that normally surface diffusion is faster than the grain boundary diffusion. However, in some cases (e.g Cu and Ni [198]) experimental values of D_b are greater than D_s. Hence, it appears that a severe limitation of this model is that diffusional crack growth can occur above V_{cr} only if $D_s < D_b$ (if $D_s > D_b$ and $V > V_{cr}$ then $\omega < \delta$).

7.4.2. (b) Crack Propagation by Thermally-Activated Bond Rupture

The mathematical theory for this process is based on 'lattice-trapping' models [133,200] and the concept of 'lattice trapping' has been described briefly in section 2.2.2. (c). When the applied stress intensity factor (K_I) is increased to a critical value K_I unstable bond rupture occurs and fast fracture results. Similarly, when K_I is decreased to a critical value K_- spontaneous bond healing occurs. In the intermediate range of K_I, $K_- < K_I < K_+$, the crack is mechanically stable or 'lattice trapped' [200].

The 'lattice trapping' occurs as a consequence of the discrete nature of the atomic arrangement in solids. The Griffith theory predicts only one value of the stress intensity factor (K_{1g}) for crack stability and this lies between the above limits (K_- and K_+). When a crack is 'lattice trapped' thermal fluctuations can cause the crack to advance subcritically if $K_1 > K_{1g}$ or to recede if $K_1 < K_{1g}$, by overcoming the respective (forward or backward) activation barriers.

This phenomenon of 'lattice trapping' is a general characteristic for crack stability in crystals. However, this mechanism has been used [135,200] to explain the slow crack growth process in lead glass in vacuum. If this is applicable to a disordered solid like glass it could be equally applicable to the grain boundary region of a polycrystal. of

Recently Fuller et al [200] have derived a crack growth relation using the 'lattice trapping' concept. They have assumed the standard Arrhenius rate equation for velocity

$$V = V_c \left| \exp\left(\frac{-\Delta U_+}{kT}\right) - \exp\left(\frac{-\Delta U_-}{kT}\right) \right| \tag{7.1}$$

where V_c is a proportionality constant and it has been assumed [200] that V_c depends only weakly on the applied stress. ΔU_+ and ΔU_- are forward and backward activation energy barriers and kT has it s usual meaning. Neglecting the backward thermal fluctuations Eqn. 7.1 can be written as

$$V = V_c \exp - \frac{\Delta U_+}{kT} \tag{7.2}$$

The forward activation energy barrier is related to the 'lattice trapping' limits K_+ and K_- and is given by [200]

$$\Delta U_+ = U_b \left(\frac{K_+}{K_+ - K_-}\right)\left(1 - \frac{K_1}{K_+}\right)^2 \tag{7.3}$$

where U_b is the activation energy necessary to rupture the interatomic bonds. Assuming the equivalence between K_+ and fracture toughness K_{1c} Eqn. 7.2 can be written as

$$V = V_c \exp \left| - \frac{U_b}{kT} \left(\frac{1}{1 - \frac{K_-}{K_{1c}}} \right) \left| 1 - \frac{K_1}{K_{1c}} \right|^2 \right| \qquad (7.4)$$

For a given temperature and environment K_- should be independent of applied stress and therefore

$$V = V_c \exp - A \left| 1 - \left(\frac{K_1}{K_{1c}} \right) \right|^2 \qquad (7.5)$$

where $A = \text{const.} = \frac{U_b}{kT} \left| \frac{1}{1 - \frac{K_-}{K_{1c}}} \right|$ of

Since K_- is usually very small compared with K_{1c}, the factor $1/\left(1 - \frac{K_-}{K_{1c}}\right) \sim 1$. The gradient (A) of $\ln V$ vs $\left(1 - \frac{K_1}{K_{1c}}\right)^2$ gives an approximate activation energy (a slightly higher value because $K_- > 0$) for the bond breaking process.

The application of this theory to heat-treated ceramics B and C and also, for comparison, to un-heat-treated ceramic C is shown in Fig. 7.15. The experimental data for heat-treated ceramic C shows a reasonable straight line fit and the gradient gives an activation energy of $\sim$ 1300 k $Jmol^{-1}$ which is higher than that obtained from the K_1-V relation ($\sim$ 950 k $Jmol^{-1}$). However, the former value ($\sim$ 1300 k $Jmol^{-1}$) is over-estimated because the factor $1/\left(1 - \frac{K_-}{K_{1c}}\right)$ is slightly greater than unity. The data for heat-treated ceramic B shows considerable scatter in the straight line fit and gives an activation energy $\sim$ 600 k $Jmol^{-1}$ which is lower than that obtained from the K_1-V relation ($\sim$ 1000 k $Jmol^{-1}$). The

departure from the straight line fit for ceramic C (un-heat-treated) indicates that the crack propagation behaviour of ceramic C at 1400°C is not described by Eqn. 7.5 and hence a 'lattice trapping' model may not be applicable.

The V_c value, i.e. crack velocity corresponding to K_{1c} for the ceramics lies between 10^{-2} - 10^{-3} ms^{-1}. Since the Eqn. 7.5 contains a normalised stress intensity factor $\left(K_1/K_{1c}\right)$, the V_c values normally fall in a reasonable range.

In summary, the K_1-V data for heat-treated ceramic C favours crack propagation by a thermally-activated bond-breaking process rather than by the coupled surface and grain boundary diffusion process. However, the crack growth behaviour of un-heat-treated ceramic C favour the latter mechanism. Furthermore, in heat-treated ceramic C at low velocities the diffusive crack growth mechanism could be dominant and at high velocities the bond breaking process could be dominant. Heat-treated ceramic B shows a moderate agreement with both mechanisms.

Finally, it is important to note that the diffusive crack growth mechanism also involves a thermally-activated 'bond-breaking' process and therefore the activation energy for the two mechanisms may be of similar magnitude. As a result these two processes might be empirically inseparable. However, in diffusive crack growth the detached atoms are diffused further away to a sink, due to a chemical potential difference, which involves a migrational activation energy. In 'lattice-trapping' models the atoms remain attached to new surfaces of the crack after bond-breaking. Hence, in thermally-activated crack propagation, the crack tip is atomically sharp and is independent of crack velocity unlike diffusive crack growth. The examination of this difference in crack tip configuration (at low velocities closer to V_{cr}) could be used to

distinguish these two mechanisms. However, the examination of such a microscopic difference will undoubtedly present experimental problems.

of

AN OVERVIEW

(i) Deformation and Fracture

The remarkable change in creep behaviour after heat-treatment provides additional experimental evidence for creep mechanisms in 'as-hot-pressed' ceramics. The observation of a transition in stress-exponent from $n > 1$ to $n \simeq 1$ with the removal of cavitation confirms the suggestion that $n > 1$ is induced by cavitation and not due to mixed mechanisms (such as dislocation motion). The absence of cavitation with the removal of triple-junction glassy phase, confirms that the cavitation in the 'as-hot-pressed' state is due to the presence of triple junction glass. Although, the observation of of non-integral stress-exponent values ($n > 1$) in β-Si_3N_4 based ceramics has been explained as a consequence of cavitation within an intergranular glassy phase, until now no direct experimental proof has been presented. The creep behaviour of ceramic C after heat-treatment supports an explanation of the initial non-steady-state behaviour in terms of a de-segregation of grain boundary impurities. In view of the creep behaviour of 'bulk' heat-treated specimens the major de-segregation mechanism is that of extraction of metallic ions into an oxide layer, accompanied by a redistribution of other segregated elements within β' crystals.

Creep parameters and microstructural observations confirm that the rate controlling creep mechanism is diffusional. Lattice diffusion is unlikely to dominate at the test temperatures in these fine-grained covalently bonded ceramics. Furthermore, the observation of transient creep behaviour in 'as-hot-pressed' ceramics and the achievement of improved creep and fracture properties via heat-treatments provide strong evidence for a deformation process associated with grain boundaries. However, due to the lack of different grain size materials it was not possible to confirm the Coble creep mechanism via the determination of grain-siz

exponent. Furthermore, as no data are available for grain boundary diffusivity of Si-Al-O-N ceramics it is not possible to identify the rate controlling atomic species in creep deformation.

The crack growth behaviour of both ceramics before and after heat-treatment is consistent with the creep behaviour. Ceramic B shows a transition from a grain boundary sliding-assisted viscous cavity nucleation and growth to diffusive crack growth or to a thermally activated bond-breaking process with heat-treatment. This transition is characterised by an increase in K_I-exponent ($n \sim 7$ to $n \sim 17$) and the introduction of a threshold K_I level for slow crack growth. The transition is also consistent with the microstructural change of a removal of triple junction glass, with heat-treatment.

The crack growth characteristics of 'as-hot-pressed' ceramic C also favour the diffusive crack growth mechanism. However, for confirmation of the particular mechanism precise values of D_s, δD_b, γ_s and γ_b are required. An accurate experimental determination of these quantities is normally difficult and even a small error in absolute values of these parameters would result in a marked change in the predicted K_I-V relation. The sensitivity of the predicted K_I-V relation to the absolute value of these parameters is evident from fig. 6.12. The heat-treated ceramic C shows a departure from the diffusive crack growth behaviour and shows a favourable agreement with the thermally activated bond breaking process. Apart from the activation energy term there is no other suitable parameter available for experimental check in the equation related to the bond-breaking process.

Finally, the reproducibility of the crack propagation data obtained here gives confidence in the use of such K_I-V plots for failure prediction (section 2.2.2(b)) in β' ceramics.

(ii) Microstructure and Engineering Application

The major microstructural difference between the two types of ceramic is the presence of a glassy phase at β′-grain triple junctions in ceramics prepared with a Mn-addition. The Auger electron spectroscopy of intergranular fracture surfaces and Edax analysis of the larger triple junctions suggest that this glassy phase is a silicate of Ca, Mn, Al and Mg (Ca is an accidental impurity). It is believed that the solubility of Mn in β′ crystals is extremely low and hence Mn stabilises the silicate phase in triple-junctions after grain impingement and remains as a residual glassy phase on cooling. However, in the case of Mg there is some experimental evidence [178] for a small solubility of Mg in β′ crystals. This results in simultaneous solid solution of oxygen for charge compensation and hence reduces the silicate liquid progressively to give a single phase condition. The presence of a residual glassy phase and hence creep cavitation even in high purity Si_3N_4 ceramics with Mg additive, demonstrates the importance of Al in controlling the residual silicate phase. Therefore, it can be concluded that the most effective way to produce a non-cavitating ceramic is to hot-press a carefully balanced Si-Al-O-N with a small amount of Mg-additive.

Apart from triple-junctions there is no resolvable phase between β′ grain boundaries in the two ceramics, within the limits of lattice-image resolution set by the β′ prism plane spacing and the instrumental capability. However, Auger electron spectroscopy of ceramic C shows that segregated impurities, mainly Mg and impurity Ca together with oxygen are present within a few atomic spacings around the boundary of each crystal.

The microstructural observations confirm the elimination of triple-junction glass in the Mn-containing ceramic with heat-treatment. The diffusion of metallic ions into the surface oxide film, due to the

concentration gradient of metallic ions between the oxide film and the triple junction glass, makes the latter unstable. Hence, the other elements Si, O, Al, etc. crystallise as β′. The presence of Al in both β′ crystals and silicate phase is an important factor in this transformation which avoids crystallisation of remaining elements as a separate oxygen rich phase or the persistence of a glassy phase.

It is believed that the de-segregation of impurities from grain boundaries increases the density of primary bonds across grain boundaries. The improved creep and fracture properties, particularly the increase in resistance to subcritical crack growth, provide strong evidence for this. Apart from superior mechanical properties heat-treated ceramics show a high oxidation resistance, an increased difficulty of diamond machining and a reduced susceptibility to dissociation. However, two problems could arise in high temperature application of these ceramics:

(i) the difficulty in fabricating complex shapes by hot-pressing and

(ii) the expense and difficulty of long term heat-treatment.

A pre-heat-treatment is not necessary if MgO-additive hot-pressed Si-Al-O-N ceramic is used because of the non-cavitating behaviour of this ceramic. During high-temperature service in oxidising environments the properties of this ceramic may improve further due to de-segregation of impurities from grain boundaries. For alternative fabrication techniques, e.g. by pressureless sintering it is difficult to achieve near theoretical density without a relatively large amount of liquid sintering aid. Hence, these ceramics are essentially two phase materials [178]. The oxidation resistance of these sintered ceramics is relatively poor [177] and this may be the most severe limitation to their high temperature application which motivates the use of single phase hot-pressed β′ ceramics in extremes of stress and temperature.

Finally, some of the main achievements of this research will be summarised:

The possibility of modifying grain boundary transport and cohesive properties to approach that conferred by covalency in β′ crystals by removing impurity segregates has been demonstrated. This work also indicates the importance of ceramic 'alloying' in fabricating non-cavitating ceramics. Si-Al-O-N C is the first example of a β-Si_3N_4-based ceramic which exhibits non-cavitating diffusional creep behaviour. The observation of a transition in creep and fracture behaviour, particularly in ceramic B with heat-treatment, clarifies many uncertainties associated with deformation and fracture mechanisms throughout the range of ceramics based on β-Si_3N_4.

REFERENCES

1. J. E. Restall and C. R. Gostelow, Proc. Brit. Ceram. Soc. ed. D. J. Godfrey, 22 (1973) 89-115.
2. K. H. Jack, 17th Mellor Memorial Lecture, Trans.,and J. Brit. Ceramic. Soc. 72 (1973) 376.
3. S. Wild, P. Grievson and K. H. Jack, "Special Ceramics 5", ed. P. Popper, Brit. Ceram. Res. Ass., 5 (1972) 385-396.
4. J. W. Edington, D. J. Rowcliffe and J. L. Henshall, Powd. Met. Int. 7 (1975) pt 1, p.82, pt 2, p.136.
5. N. L. Parr and E. R. W. May, Proc. Brit. Ceram. Soc. 7 (1967) 81.
6. K. L. Brown, D. J. Godfrey, M. W. Lindley and E. R. W. May, "Special Ceramics 5", ed. P. Popper, Brit. Ceram. Res. Assoc. (1972) 345.
7. A. Ezis, "Ceramics for High Performance Applications" eds. J. J. Burke, A. E. Gorum and R. N. Katz, Brook Hill, Pub. Co., (1975) 207.
8. E. R. Herrman and E. A. Fisher, Amer. Ceram. Soc. Sympo. 4 (1972).
9. P. Popper, "Special Ceramics" (Proceedings of British Ceramic Research Association Symposium) London (Heywood) (1960) 209.
10. F. F. Lange and J. L. Iskoe, "Ceramics for High Performance Applications" eds. J. J. Burke, A. E. Gorum and R. N. Katz, Brook Hill Pub. Co. (1974) 223-239.
11. G. G. Deeley, J. M. Herbert and N. C. Moore, Powd. Met. 8 (1961) 145.
12. R. J. Lumby and R. F. Coe, Proc. Brit. Ceram. Soc. 15 (1970) 91.
13. S. Wild, P. Grievson, K. H. Jack and M. Latimer, "Special Ceramics 5" (1972) 377-382.
14. P. Drew, M. H. Lewis, J. Mat. Sci. 9 (1974) 261-269.
15. D. W. Richerson, Amer. Ceram. Soc. Bull. 52 (1973) 560.

16. R. Kossowsky, J. Mat. Sci. 8 (1973) 1603.

17. M. L. Torti, R. A. Alliegro, M. E. Washburn, D. W. Richerson and G. Q. Weaver, Proc. Brit. Ceram. Soc. 22 (1973) 129.

18. F. F. Lange, J. Amer. Ceram. Soc. 57 (1974) 84.

19. A. G. Evans, S. M. Wiederhorn, J. Mat. Sci. 9 (1974) 270-278.

20. F. Galasso, U. Kuntz and J. Croft William, J. Amer. Ceram. Soc. 55, No. 8 (1972) 431.

21. T. D. Gulden, J. Amer. Ceram. Soc. 51 (1968) 424.

22. G. E. Gazza, J. Amer. Ceram. Soc. 56 (1973) 662.

23. F. F. Lange, S. C. Singhal and R. C. Kuznicki, Westinghouse Elect. Corp. Tech. Rpt. 6, Contract No. N 00014-74-C-0284.

24. J. J. Brennan, United Tech. Res. Centre, Tech. Rpt. R75-912081-2, Contract No. 62269-75-C-0137, Sept. 1975.

25. Y. Oyama and O. Kamigaito, Jap. J. Appl. Phys. 10 (1971) 1637.

26. K. H. Jack and W. I. Wilson, Nature 238 (1972) 28.

27. K. H. Jack, J. Mat. Sci. 11 (1976) 1135-1158.

28. P. Drew, M. H. Lewis, J. Mat. Sci. 9 (1974) 1833-1838

29. R. J. Lumby, B. North and A. J. Taylor, "Special Ceramics 6", ed. P. Popper (Brit. Ceram. Res. Assoc.) (1974) 283-298.

30. K. H. Jack, eds. Hayne Palmour III, R. F. Davis and T. M. Hare, Mat. Sci. Res. Vol. II (1978) 561-578.

31. M. H. Lewis, B. D. Powell, P. Drew, R. J. Lumby, B. North, A. J. Taylor, J. Mat. Sci. 12 (1977) 61-74 .

32. M. H. Lewis and G. Smith in "Advances in Research on the Strength and Fracture of Materials", ed. Taplin, Pergamon (1977).

33. W. D. Kingery and E. D. Montrone, J. App. Phys. 36 (1965) 2412.

34. F. R. N. Nabarro, Report on the Conference on Strength of Solids (London, The Physical Society) 1948.

35. C. Herring, J. Appl. Phys. 21 (1950) 437.

36. R. L. Coble, J. Appl. Phys. 34 (1963) 1679.

37. I. M. Lifshitz, Soviet Phys. 17 (1963) 909.

38. R. Raj and M. F. Ashby, Metall. Trans. 2 (1971) 1113-1127.

39. M. F. Ashby and R. A. Verrall, Acta Metall. 21 (1973) 149-163.

40. W. R. Cannon, Phil. Mag. 25 (1972) 1489-1497.

41. D. Lee, Metall. Trans. 1 (1969) 309.

42. H. Naziri, R. Pearce, M. Henderson Brown and K. F. Hale, J. Microsc. 97 (1973) 229.

43. T. E. Chung and D. T. J. Davies, Acta. Metall. 27 (1979) 627-635.

44. R. M. Cannon and R. L. Coble, "Deformation of Ceramics Materials" eds. R. C. Bradt and R. E. Tressler (Pergamon Press) (1974) 61-93.

45. A. G. Evans and T. G. Longdon, Progress in Material Science (Pergamon Press) 21 (1976) 171-442.

46. J. Weertman, Trans. Metall. Soc. A.I.M.E. 227 (1963) 1475.

47. J. Weertman, J. Appl. Phys. 28 (1957) 362.

48. F. R. N. Nabarro, Phil. Mag. 16 (1967) 231.

49. M. F. Ashby, Acta. Met. 20 (1972) 887-896.

50. M. F. Ashby and H. J. Frost, Frontiers in Materials Science. Dekker, N. York (1976) 391-419.

51. T. G. Langdon and F. A. Mohamed, J. Mat. Sci. 11 (1976) 317-327.

52. J. D. Hodge, P. A. Lessing, R. S. Gordon, J. Mat. Sci. 12 (1977) 1598-1604.

53. W. D. Kingery, H. K. Bowen and D. R. Uhlmann in "Introduction to Ceramics", (second edition) (Wiley and Sons) (1975) 745.

54. T. Vasilos, J. B. Mitchell and R. M. Spriggs, J. Amer. Ceram. Soc. 47 [4] (1964) 203-204.

55. E. M. Passmore, R. H. Duff and T. Vasilos, ibid, 49 [11] (1966) 594-600.

56. H. Tagai and T. Zisner, ibid 51 [6] (1968) 303-310.

57. T. Zisner and H. Tagai, ibid, p. 310-314.

58. G. R. Terwilliger, H. K. Bowen and R. S. Gordon, ibid, 53 [5] (1970) 241-251.

59. R. R. Vandervoort and W. L. Barmore, ibid, 46 [4] (1963) 180-184.

60. A. H. Heuer, R. M. Cannon and N. J. Tighe, "Ultrfine-Grain Ceramics", eds. J. J. Burke, N. L. Reed and Volker Weiss, Syracuse University Press (1970) 339-365.

61. G. W. Hollenberg and R. S. Gordon, J. Amer. Ceram. Soc. 56 [3] (1973) 140-147.

62. R. S. Gordon and G. R. Terwilliger, J. Amer. Ceram. Soc. 55 [9] (1972) 450-455.

63. J. Crampon, B. Escaig, J. Mat. Sci. 13 (1978) 2619-2626.

64. P. L. Farnsworth and R. L. Coble, J. Amer. Ceram. Soc. 49 [5] (1966) 264-268.

65. A. Mocellin and W. D. Kingery, J. Amer. Ceram. Soc. 54 [7] (1971) 339-341.

66. P. A. Lessing, R. S. Gordon, J. Mat. Sci. 12 (1977) 2291-2302.

67. T. G. Langdon and J. A. Pask, Acta. Meta. 18 (1970) 505.

68. J. H. Hensler and G. V. Cullen, J. Amer. Ceram. Soc. 51 (1968) 557.

69. J. M. Birch and B. Wilshire, J. Mat. Sci. 9 (1974) 794.

70. J. B. Bilde-Sorenson, J. Amer. Ceram. Soc. 55 (1972) 606.

71. S. I. Warshaw and F. H. Norton, J. Amer. Ceram. Soc. 45 (1962) 479.

72. W. R. Cannon and O. D. Sherby, J. Amer. Ceram. Soc. 56 (1973) 157.

73. W. L. Barmore and R. R. Vandervoort, J. Amer. Ceram. Soc. 50 (1967) 316.

74. D. E. Stellrecht, M. S. Farkas and D. P. Moak, J. Amer. Ceram. Soc. 51 (1968) 455.

75. W. R. Cannon and O. D. Sherby, J. Amer. Ceram. Soc. 53 (1970) 346.

76. D. R. Cropper and T. G. Langdon, Phil. Mag. 18 (1968) 1181.

77. M. F. Ashby, Scripta Met. 3 (1969) 1837.

78. G. W. Greenwood, Scripta Met. 4 (1970) 171.

79. R. T. Tremper, R. A. Giddings, J. D. Hodge and R. S. Gordon, J. Amer. Ceram. Soc. 57 (1974) 421.

80. R. C. Folweiler, J. Appl. Phys. 32 (1961) 773.

81. A. Crosby, P. E. Evans, J. Mat. Sci. 8 (1973) 1573-1580.

82. T. L. Francis and R. L. Coble, J. Am. Ceram. Soc. 5 No. 2 (1968) 115-116.

83. M. S. Seltzer, Amer. Ceram. Soc. Bulletin, 56 [4] (1977) 418-423.

84. R. S. Gordon, J. Am. Ceram. Soc. 56 (1973) 147-152.

85. P. Marshall and R. B. Jones, Powd. Met. 12 (1968) 193.

86. R. M. Adams, Ph.D. Thesis, Univ. of Leeds (1972).

87. Ram Kossowsky, D. G. Miller, E. S. Diaz, J. of Mat. Science, 10 (1975) 983-997.

88. E. Butler, Phil. Mag. 24 (1971) 829-834.

89. A. G. Evans and R. W. Davidge, J. Mat. Sci. 5 (1970) 314-325.

90. A. G. Evans and J. V. Sharp. J. Mat. Sci. 6 (1971) 1292-1301.

91. R. Kossowsky, J. Amer. Ceram. Soc. 56 (1973) 531-535.

92. Salah Ud Din, P. S. Nicholson, J. Mat. Sci. 10 (1975) 1375-1380.

93. J. M. Birch, B. Wilshire, J. Mat. Sci. 13 (1978) 2627-2636.

94. J. M. Birch, B. Wilshire and D. J. Godfrey, Proc. Brit. Ceram. Soc. 26 (1978) 141.

95. J. M. Birch, B. Wilshire, D. J. R. Owen and D. Shantaram, J. Mat. Sci. 11 (1976) 1817.

96. J. A. Mangles, "Ceramics for High Performance Applications" eds. J. J. Burke, A. E. Gorum, R. Nathankutz (1974) 195-206.

97. Salah Ud Din and P. S. Nicholson, J. Amer. Ceram. Soc. 58 No. 11-12 (1975) 500-502.

98. A. A. Griffith, Phil. Trans. Roy. Soc. London 221A (1920) 163.

99. A. G. Evans and R. W. Davidge, Phil. Mag. 20 , No. 164 (1969) 373-388.

100. R. W. Davidge and G. Tappin, "Proceedings of the British Ceramic Society", 15 (1970) 47.

101. W. Weibull, J. App. Mech. 18 (1951) 293-297.

102. P. Stanley, A. D. Sivill and H. Fessler, "Fracture Mechanics of Ceramics" eds. R. C. Bradt, D. P. H. Hasselman and F. F. Lange, 3 (1978) 51.

103. R. W. Davidge, J. R. McLaren and G. Tappin, J. Mat. Sci. 8 (1973) 1699-1705.

104. B. R. Lawn and J. R. Wilshaw in "Fracture of Brittle Solids", (Cambridge Univ. Press 1975).

105. E. Orowan, Rep. Prog. Phys. 12 (1949) 185.

106. G. R. Irwin, Jou. Welding 31 (1952) 450.

107. J. F. Knott, in "Fundamentals of Fracture Mechanics" Butterworths, London 1973.

108. R. W. Nicholls, F. M. Burdekin, A. Coway, D. Elliot and T. Ingan, Proc. Symposium on Fracture Toughness Concepts for Weldable Structural Steel, Culceth, England 1969.

109. J. R. Rice, J. Appl. Mech. Tran. ASME (1968) 379.

110. P. L. Gutshall and G. E. Gross, Eng. Fract. Mech. 1 (1969) 467.

111. A. G. Evans and R. W. Davidge, J. Nuclear Mat. 33 (1969) 249.

112. L. A. Simpson, J. Am. Ceram. Soc. 56 (1973) 610.

113. A. G. Evans and G. Tappin, Proc. of Brit. Ceram. Soc. 20 (1972) 275.

114. J. L. Henshall, D. J. Rowcliffe and J. W. Edington, "Special Ceramics 6", ed. P. Popper, Brit. Ceram. Res. Ass. (1975) 185.

115. A. G. Evans and F. F. Lange, J. Of Mat. Sci. 10 (1975) 1659-1664.

116. A. G. Evans, "Ceramics for High-Performance Applications", eds: John J. Burke, Alvin E. Gorun, R. N. Katz (1974) 373-397.

117. P. C. Paris and G. C. Sih, ASTM Special Tech. Publ. No. 381 (1965).

118. H. H. Johnson and P. C. Paris, Eng. Fract. Mech. 1 (1968) 3.

119. R. J. Charles and B. W. Hillig, "Symposium on the Mechanical Strength of Glass and Ways of Improving it", at Florence, Italy. Union Scientifique Cantinentale du Verre, Charleroi, Belgium (1962) 511.

120. B. W. Hillig and R. J. Charles, "High Strength Materials", ed. V. F. Zackay, John Wiley, New York (1965) 682-705.

121. R. H. Doremus, J. Appl. Phys. 47 (1976) 540.

122. A. G. Evans and H. Johnson, J. Mat. Sci. 10 (1975) 214-222.

123. S. M. Wiederhorn, J. Am. Ceram. Soc. 50 (1967) 407.

124. G. W. Weidmann and D. G. Holloway, Physics and Chemistry of Glasses, 15 No. 5, (1974) 116.

125. A. G. Evans, J. Mat. Sci. 7 (1972) 1137-1146.

126. A. G. Evans and M. Linzer, J. Am. Ceram. Soc. 53 (1973) 543.

127. S. M. Wiederhorn, Int. J. Fract. Mech. 4 (1968) 171.

128. J. L. Henshall, D. Rowcliffe and J. W. Edington, Proc. of the 4th Int. Conf. on Fracture. ed. D. M. R. Taplin 3 (1977) 875.

129. A. G. Evans, L. R. Russell, D. W. Richerson, Met. Trans. 6A (1975) 707-715.

130. H. Meredith and P. L. Pratt, "Special Ceramics", ed. P. Popper, Brit. Ceram. Res. Ass. 6 (1975) 107.

131. R. N. Stevens and R. Dutton, Mat. Sci. Eng. 8 (1971) 220.

132. D. P. H. Hasselman, "Ultrafine-Grain Ceramics", eds. J. J. Burke, N. L. Reed, V. Weiss, Syracuse Univ. Press, New York (1970) 297.

133. R. Thomson, C. Hsiech and V. Rana, J. Appl. Phys. 42 (1971) 3154.

134. S. M. Wiederhorn, B. J. Hockey and D. E. Roberts, Phil. Mag. 28 (1973) 783.

135. S. M. Wiederhorn, H. Johnson, A. M. Diness and A. H. Heuer, J. Am. Ceram. Soc. 57 (1974) 336.

136. A. G. Evans, "Fracture Mechanics of Ceramics", eds. R. C. Bradt, D. P. H. Hasselman and F. F. Lange, 1 (1974) 17.

137. S. Mostovoy, P. B. Crosley and E. J. Ripling, J. Mats. 2 (1967) 661.

138. J. A. Kies and A. B. J. Clark, Proceedings of the Second International Conference on Fracture, Brighton, 1969, paper 42.

139. D. P. Williams and A. G. Evans, J. Test. Eval. 1 (1973) 264.

140. S. W. Frieman, D. R. Mulville and P. W. Mark, Report of NRL Progress, (1972) 36.

141. E. A. Steigorwald and G. L. Hanna, Proceed. Amer. Soc. for Testing and Materials, 62 (1962) 885-913.

142. W. F. Brown and J. E. Strawley, Plane Strain Crack Toughness, Testing of High Strength Metallic Materials, STP 410, American Society for Testing and Materials, 1966.

143. M. L. Mendelson, J. Am. Ceram. Soc. 52 (1960) 443-446.

144. J. M. Cowley, Acta. Cryst. 12 (1959) 367.

145. P. B. Hirsch, A. Howie, R. B. Nicholson, D. W. Pashley, M. J. Whelan, "Electron Microscopy of Thin Crystals", Butterworth, London (1965) 366.

146. D. K. Bowen and C. R.Hall, "Microscopy of Materials", The MacMillen Press Ltd., London, (1975) 157.

147. D. R. Clarke, J. Appl. Phys. 49 (1978).

148. D. R. Clarke and G. Thomas, J. Am. Ceram. Soc. 60 (1977) 491-495.

149. L. K. V. Lou, J. E, Mitchell and A. H. Heuer, J. Am. Ceram. Soc. 61, (1978) 392-396.

150. L. A. Harris, J. Appl. Phys. 39 [3] (1968) 1419-1427.

151. J. C. Riviere, Contemp. Phys. 14 (1973) 513-539.

152. C. C. Chang, Surface Sci. 25 (1971) 53.

153. B. D. Powell and P. Drew, J. Mat. Sci. 9 (1974) 1867-1870.

154. W. C. Johnson and D. F. Stein, R. W. Rice, J. Am. Ceram. Soc. 57 (1974) 342-344.

155. N. Laegreid and G. K. Wehner, J. Appl. Phys. 32 (1961) 365.

156. D. F. Stein, W. C. Johnson and L. White in "Grain Boundary Structure and Properties", eds. G. A. Chadwick, D. A. Smith, (Academic Press, London 1976.

157. H. L. Marcus, J. M. Harris and F.J. Szalkowski, "Fracture Mechanics of Ceramics", eds. R. C. Bradt, D. P. H. Hasselman and F. F. Lange, 1 (1974) 387-398.

158. L. E. Davis, N. C. MacDonald, P. W. Planberg, G. E. Riach and R. E. Weber in Handbook of Auger Electrons Spectroscopy, Pub. Physical Electronics Industires, Inc. Second Edition (1976).

159. J. A. Venables, A. P. Janssen, C. J. Harland and B. A. Joyce, Phil. Mag. 34 [3] (1976) 495-500.

160. R. D. Schile and R. L. Sierakowski, Int. J. Non-Linear Mech. 2 (1966) 61-68.

161. G. W. Hollenberg, G. R. Terwilliger and R. S. Gordon. J. Am. Ceram. Soc. 54 (1971) 196-200.

162. G. G. Trantina, J. Am. Ceram. Soc. 60 (1977) 338-341.

163. N. J. Tighe, J. Mat. Sci. 11 (1978) 1455-1463.

164. S. Spinner and W. Tefft, Am. Society for Testing Material, 61 (1961) 1221.

165. S. Timoshenko, "Strength of Materials", (Von Nostrand Reinhold, New York) pt.II (1958) 57.

166. N. Claussen, R. Pabst and C. P. Lahmann, Brit. Ceram. Soc. 25 (1975) 139-149.

167. J. L. Henshall, D. J. Rowcliffe, J. Mat. Sci. 9 (1974) 1559-1561.

168. L. A. Simpson, J. Am. Ceram. Soc. 57, (1974) 151.

169. H. P. Smith and D. E. Piper, "Stress Corrosion Cracking in High Strength Steels and in Titanium and Aluminium Alloys", eds. B. F. Brown (Naval Research Laboratory, Washington) (1972) 17.

170. S. Timoshenko and J. N. Goodier, Theory of Elasticity, McGraw-Hill, New York, 2nd ed. (1951) .277.

171. J. L. Henshall, Ph.D. thesis, University of Cambridge, 1975.

172. N. J. Osborne, Proc. Brit. Ceram. Soc. 25 (1975) 263.

173. F. F. Lange, B. I. Davis and D. R. Clarke, Rockwell International Science Centre, Thousand Oaks, California, Private communication.

174. M. S. Seltzer, High Temperature Creep of Ceramics, Final Report, AFML-TR-76-97 (1976).

175. P. K. Talty, R. A. Dirks, J. Mat. Sci. 13 (1978) 580-586.

176. G. L. Squires in 'Practical Physics', McGraw-Hill; London (1968).

177. M. H. Lewis and P. Barnard, J. Mat. Sci. in press.

178. M. H. Lewis, A. R. Bhatti, R. J. Lumby and B. North, J. Mat. Sci. in press.

179. A. J. Perry, J. Mat. Sci., 9 (1974) 1016-1019.

180. J. N. Greenwood, D. R. Miller and J. W. Suiter, Acta. Metall. 2 (1954) 250-258.

181. R. W. Balluffi and L. L. Seigle, Acta. Metall. 3 (1955) 170-177.

182. E. S. Machlin, Trans. Met. Soc. A.I.M.E. 206 (1956) 106.

183. C. W. Chen and E. S. Machlin, Acta. Metal. 4 (1956) 655.

184. J. E. Harris, Trans. Met. Soc. A.I.M.E. 233 (1965) 1509.

185. R. Raj and M. F. Ashby, Acta. Metall. 23 (1975) 653-666.

186. A. H. Cottrell, 'Intercrystalline Creep Fracture', Symposium on Structural Processes in Creep, Iron and Steel Inst. and Inst. of Metals, London 1961.

187. R. Raj, Acta. Metall. 26 (1978) 995-1006.

188. R. Resnick and L. Seigle; Trans. Met. Soc. A.I.M.E. 209 (1957) 87.

189. D. Hull and D. E. Rimmer, Phil. Mag. 4 (1959) 673.

190. M. V. Speight and J. E. Harris; J. Met. Sci. 1 (1967) 83.

191. J. Weertman, Scripta. Met. 7 (1973) 1129.

192. V. D. Scott, F. G. Stott and A. D. Wilcock, J. Inst. Metals, 101 (1973) 315.

193. B. F. Dayson and D. McLean, J. Metal. Sci. 6 (1972) 220.

194. F. F. Lange, 'Deformation of Ceramic Materials', Eds. R. C. Bradt and R. E. Tressler, Plenum Press, (1975) 361-381.

195. R. Raj and C. H. Dang, Phil. Mag. 32 (1975) 909-921.

196. R. Raj, Report No: 4092, Materials Sci. Centre, Cornell University, New York (1979) 104-129.

197. R. Dutton, "Fracture Mechanics of Ceramics", Eds. R. C. Bradt, D. P. H. Hasselman and F. F. Lange, 2 (1974) 647-657.

198. T. T. Chuang, U. S. Atomic Energy Commission, Contract No. AT (11-1) -3084, Technical Report No. 32, Nov. 1974.

199. A. H. Cottrell in 'An Introduction to Metallurgy' (1967) Pub. Edward Arnold Ltd.,

200. E. R. Fuller, Jr., and R. Thomson, Fracture Mechanics of Ceramics, Eds. R. C. Bradt, D. P. H. Hasselman and F. F. Lange, Plenum Press, New York, 4 (1978) 508.